

**Dense hollow fiber perovskite membranes for
oxygen separation and partial oxidation of
light hydrocarbons**

von der Naturwissenschaftlichen Fakultät der Gottfried Wilhelm Leibniz
Universität Hannover zur Erlangung des Grades eines
Doktor der Naturwissenschaften

- Dr. rer. nat. -

genehmigte Dissertation

von

Cristina Tablet

(Master chimie)

geboren am 14. Juni 1976 in Fetesti, Rumänien

Hannover, 2006

Dissertation im Fach Physikalische Chemie

eingereicht von Cristina Tablet, geb. am 14. Juni 1976 in Fetesti

Referent: Univ-Prof. Dr. Jürgen Caro

Institut für Physikalische Chemie und Elektrochemie, Universität Hannover

Korreferent: Univ-Prof. Dr. Reinhard Schomäcker

Institut für Chemie, Technische Universität Berlin

Tag der Promotion: 12.07.2006

Erklärung an Eides statt

Hiermit erkläre ich, dass ich die vorliegende Arbeit selbstständig verfasst und nur unter Verwendung der angegebenen Quellen und Hilfsmittel angefertigt habe. Die Dissertation ist nicht schon als Diplomarbeit oder ähnliche Prüfungsarbeit verwendet worden.

Hannover, den 30.05.2006

Cristina Tablet

Abstract

Perovskites are well-studied materials for mixed ionic and electronic conducting membranes (MIECM) with selective oxygen transport. Usually, the perovskite powder is pressed into a disc geometry. Because of the disadvantages of the disc geometry for industrial applications, hollow fibers of the perovskite $\text{BaCo}_x\text{Fe}_y\text{Zr}_2\text{O}_{3-\delta}$ (BCFZ) were prepared by a spinning process and the oxygen separation and the partial oxidation properties of these hollow fibers were evaluated.

In a high-temperature permeator the separation of oxygen and the production of oxygen-enriched air were studied. The desired (i) oxygen concentration in the oxygen-enriched air and (ii) production rate of oxygen-enriched air for different industry processes can be adjusted by controlling the operational temperatures, the oxygen partial pressure difference between feed and permeate side, and the flow rates of the air used as feed and sweep gas. The highest oxygen flux so far reported for perovskite membranes was found.

The BCFZ hollow fibers were used as well in a membrane reactor in the catalytic partial oxidation of methane (POM) to syngas ($\text{CO} + \text{H}_2$). The best location of the Ni-based steam reforming (SR) catalyst was found to be behind the fiber in the direction of the reactor outlet without direct contact between fiber and catalyst. Mechanistic studies showed that the so called partial oxidation of methane to syngas is a 2-step reaction of first total methane oxidation followed by reforming. The oxygen permeation flux of the hollow fiber membrane under POM reaction conditions was even higher compared to the case using an inert sweep gas.

Comparing the oxidative dehydrogenation of ethane on the BCFZ disc and hollow fiber membrane reactors, the ethylene selectivity on the disc membrane reactor was found to be higher. Disc membrane reactor performs more selectively compared to the hollow fiber due to a shorter residence time in the former reactor. In the case of the hollow fiber membrane the deeper oxidation of ethylene to CO and CO_2 could not be avoided.

Keywords: hollow fiber membranes, oxygen permeation, partial oxidation of methane.

Zusammenfassung

Perowskite sind gut untersuchte Gemischtleiter (*mixed ionic and electronic conducting membranes*, MIECM) mit selektivem Sauerstofftransport. Üblicherweise werden die Perowskitpulver zu einer Scheibengeometrie verformt. Da diese aber anwendungstechnische Nachteile mit sich bringt, wurden durch Spinnen hergestellte Hohlfasern des Perowskiten $\text{BaCo}_x\text{Fe}_y\text{Zr}_z\text{O}_{3-\delta}$ (BCFZ) für die Sauerstoffabtrennung und Partialoxidation evaluiert.

In einem Hochtemperaturpermeator wurden die Abtrennung von Sauerstoff und die Erzeugung sauerstoffangereicherter Luft untersucht. Die gewünschte Sauerstoffkonzentration in der sauerstoffangereicherten Luft und die erwünschte Menge an sauerstoffangereicherter Luft können durch Einstellen der Permeationsparameter Temperatur, Sauerstoffpartialdruckdifferenz sowie Gasgeschwindigkeiten erhalten werden. Es wurden die höchsten bislang für Perowskite gefundenen Sauerstoff-Flüsse gemessen.

Die BCFZ-Hohlfasern wurden auch als Membranreaktor in der katalytischen Partialoxidation von Methan (*partial oxidation of methane*, POM) zu Synthesegas (CO , H_2) eingesetzt. Als die beste Katalysatorposition erwies sich eine Anordnung des Ni-basierten *steam reforming* (SR) Katalysators nach der BCFZ-Hohlfaser in Richtung Reaktorausgang ohne direkten Kontakt der Faser mit dem Katalysator. Mechanistische Untersuchungen zeigten, dass die sogen. Partialoxidation des Methans zu Synthesegas eine 2-stufige Reaktion aus Totaloxidation und folgendem Reforming ist. Durch Vergrößerung der Sauerstoffpartialdruckunterschiede in der POM-Reaktion verglichen mit dem Einsatz eines Spülgases, steigen die ohnehin schon hohen Sauerstoff-Flüsse der BCFZ-Faser im POM-Reaktorbetrieb weiter an.

In der oxidativen Dehydrierung des Ethans zu Ethylen wurde gefunden, dass die Ethylenselektivität im Membranreaktor in Scheibengeometrie viel höher als im Hohlfaserreaktor ist, da die Scheibengeometrie nur einen kurzen Kontakt der Eduktmoleküle mit der Membranoberfläche erlaubt. Wiederholte Kontakte erfolgen hingegen in der Hohlfaser, so dass dort die tiefe Oxidation zu CO/CO_2 stattfindet.

Schlagwörter: Hohlfasermembranen, Sauerstoffpermeation, Partialoxidation von Methan.

Acknowledgement

Firstly, I would like to express my deep gratitude to Prof. Dr. Jürgen Caro for giving me an opportunity to work in such an interesting and promising hollow fiber membrane reactor field. I would like to thank him especially for his support and attention throughout my work and his useful recommendations.

I would also like to extend my gratitude to Prof. Dr. Reinhard Schomäcker for his supervision and for very stimulating discussions related to hollow fiber perovskite membrane reactors. Furthermore, I thank Dr. Haihui Wang for his valuable comments and assistance throughout my work and Dr. Gerd Grubert for his worthwhile comments at the beginning of my Ph.D study.

I also take the opportunity to thank Dr. Thomas Schiestel and Dipl. Chem Mirjam Kilgus for providing the hollow fibre perovskite membranes and Dipl. Chem. Christof Hamel for the developed model for the production of the O₂-enriched air. I thank Dr. E. Kondratenko for the transient experiments in the temporal analysis of products reactor and Dr. A. Feldhoff for his valuable assistance in the scanning electron microscopy and for providing TEM micrographs. I thank M. Sc. Catherine Aresipathi und Dipl. Chem. Roland Marshall for their help in my work.

I would like to thank all the staff of the mechanical workshop, Mr. Bieder, Mr. Egly and Mr. Becker in particular who helped me in constructing the permeation apparatus, as well as to Mr. Ribbe and Mr. Schmunkamp, from the electrical workshop, for his help in dealing with technical problems. My special thanks to all the colleagues of the Institute of Physical Chemistry and Electrochemistry for their encouragement and support, all through my work.

The membranes and catalysts which I have used in this thesis were developed within the frame of the German Competence Network Catalysis (ConNeCat) in the “Lighthouse” - Project “CaMeRA – Catalytic Membrane Reactor”. I am very grateful towards the industry partners Uhde-Thyssen-Krupp, Bayer Technology Services and Borsig for the permission to publish these results.

Contents

Contents.....	1
1 Mixed oxygen ion and electron conducting membranes (MIECM)	5
1.1 A special mineral: the perovskite	6
1.2 Theory of oxygen transport	7
1.3 Applications of MIECM in oxygen permeable membrane separators and membrane reactors.....	13
1.3.1 Production of pure O ₂ and O ₂ -enriched air	13
1.3.2 Partial oxidation of methane (POM) to synthesis gas	16
1.3.3 Oxidative coupling of methane (OCM).....	19
1.3.4 Oxidative dehydrogenation of light alkanes to olefins.....	21
1.3 Aim of the thesis.....	23
1.4 Bibliography	24
2 Experimental.....	29
2.1 Membranes preparation	29
2.1.1 Preparation of the disc membranes	29
2.1.2 Preparation of the hollow fiber membranes	31
2.2 Structure and microstructure of the dense membranes.....	32
2.2.1 X-ray diffraction.....	32
2.2.2 Electron microscopy	32
2.3 Oxygen permeation through perovskite membrane	33
2.3.1 The hollow fiber membrane reactor	34
2.3.2 The disc membrane reactor	36
2.4 Production of O ₂ -enriched air.....	37

2.5 POM in a hollow fiber membrane reactor	39
2.6 Selective oxidations of C ₂ H ₆ and CH ₄	40
2.6.1 Transient experiments in the temporal analysis of products (TAP) reactor	40
2.6.2 Oxidation in membrane reactors	42
2.7 Bibliography	43
3 High oxygen permeation through MIEC hollow fiber perovskite membranes	45
3.1 Membrane morphology	45
3.2 Micro- and ultrastructure of grain boundaries in perovskite ceramics by transmission electron microscopy	48
3.3 Selection of an optimum material for the hollow fiber membranes.....	50
3.4 Oxygen permeation flux through BaCo _x Fe _y Zr _z O _{3-δ} (BCFZ) disc and hollow fiber membranes	56
3.5 Oxygen permeation flux through hollow fiber membranes coated with Au paste.....	62
3.6 Conclusions	69
3.7 Bibliography	70
4 Experimental and modeling study of dense perovskite hollow fiber membranes for the production of O₂-enriched air.....	71
4.1 Model development for the production of O ₂ -enriched air	71
4.2 Estimation of mass transfer parameters.....	74
4.3 O ₂ -enriched air production results.....	76
4.4 Stability.....	82
4.5 Conclusions	86

4.6 Notation	86
4.7 Bibliography	88
5 POM in a perovskite hollow fiber membrane reactor	90
5.1 POM reaction in a hollow fiber membrane reactor without catalyst.....	92
5.2 POM reaction in a modified hollow fiber membrane reactor with reforming catalyst layer	93
5.3 POM reaction in a hollow fiber membrane reactor with reforming catalyst.....	96
5.4 Possible pathways of reactions for the POM to syngas in a hollow fiber membrane reactor with reforming catalyst	98
5.5 Stability of the hollow fiber membrane during the POM reaction	100
5.6 Conclusions	107
5.7 Bibliography	108
6 Selective oxidations C₂H₆ over a MIECM perovskite — a TAP and membrane reactors study	110
6.1 Test of the catalytic activity of BCFZ in the ODE	111
6.2 C ₂ H ₆ and CH ₄ oxidation over oxidized BCFZ catalyst under transient vacuum conditions in the TAP reactor	112
6.3 Ethane and methane oxidative transformations in the BCFZ membrane reactor	116
6.4 Mechanistic aspects of hydrocarbon conversion over BCFZ perovskite	122
6.6 Conclusions	124
6.7 Bibliography	126
7 Conclusions and outlook	127

Contents

List of publications and conferences..... 130

Curriculum vitae 137

1 Mixed oxygen ion and electron conducting membranes (MIECM)

Mixed ion and electron conducting membranes (MIECM) have attracted much interest in the last decades due to their applications in pure oxygen separation [1, 2] and in the field of chemical processing, including partial oxidation of natural gas to syngas [3–6], oxidative coupling of methane to value-added products such as ethane/ethane [7-11], selective oxidation of hydrocarbons [12-14] waste reduction and recovery [15]. Among the mixed-conducting ceramic membranes, perovskite-type (ABO_3) ceramic membranes exhibit the highest oxygen permeability due to their high ionic and electronic conductivity. Teraoka et al. [16, 17] were the first to report high oxygen permeation flux through several $La_{1-x}Sr_xCo_{1-y}Fe_yO_{3-\delta}$ perovskite membranes. The aim of the material synthesis is to substitute the lattice positions A and/or B of the perovskite ABO_3 structure by cations of similar size but lower charge to create an oxygen transporting material with both ionic and electronic conductivity and sufficient chemical and mechanical stability.

For practical applications, a dense oxygen separation membrane should possess the following properties: (1) the materials must be stable for long-term operation under strongly reducing atmosphere, such as the mixture of carbon monoxide and hydrogen, at elevated temperatures (> 700 °C); (2) the materials must have considerable high oxygen permeability under the operation conditions; (3) the materials must have enough mechanical strength for constructing the membrane reactor; (4) the oxygen permeability of the membrane materials should avoid a decline with time; (5) the materials should be cheap enough for large-scale industrial applications.

1.1 A special mineral: the perovskite

The parent mineral was first described from samples found in the Ural Mountains in 1839 by the geologist Gustav Rose, who named it after the famous Russian mineralogist Count Lev Aleksevich von Perovski. It is nowadays regarded as the most abundant solid phase (70-80 %) of the lower earth mantle (670 to 2900 km depth).

The general structure of the perovskite mineral is ABX_3 where A and B are cations and X oxygen anions. One way to visualize the structure is to place the smaller B cation in an oxygen octahedral environment on the corner of a cube which center would be occupied by the larger A cation, as seen on Fig. 1.1. In such a cubic structure, the coordination numbers of the A and B cations are 12 and 6, respectively. The A cation is generally an alkali earth metal or a transition metal. The B cation is a transition metal or a rare earth metal but can also be found in the family (Al, Ga, Pb, Bi, Ti, etc).

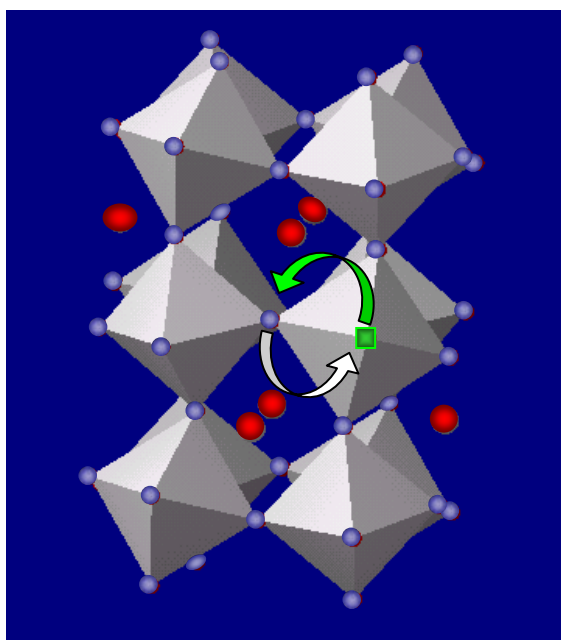


Figure 1.1 Ideal perovskite structure of CaTiO_3 .

The relative size difference between the two types of cations can lead to the tilting of the BO_6 octahedra, the structure therefore becoming orthorhombic. Goldschmidt introduced a

so-called tolerance factor [18] being in essence a measure of the “cubic-ness” of the perovskite structure. The definition of this factor is:

$$t = \frac{r_A + r_B}{\sqrt{2}(r_B + r_O)} \quad (1.1)$$

where r_A , r_B and r_O are the ionic radii of the A-site cation, the B-site cation and the oxygen anion, respectively. When t equals unity, the structure is cubic. Lower values of t correspond to lower symmetry.

Perovskite materials are classified as ceramics and can be doped, i.e. a fraction of the A-site and/or the B-site cations can be replaced by another metal. It is therefore possible to tune the properties of these ceramics for a very wide range of applications.

Materials with the perovskite structure can also be mixed ionic and electronic conductors (MIEC). Their use as membrane for oxygen separation will be the core of this thesis.

1.2 Theory of oxygen transport

Fig. 1.2 illustrates the oxygen permeation through a dense oxygen permeable membrane driven by an oxygen partial pressure gradient across it. The oxygen permeation involves three steps. At first, oxygen molecules adsorb and become reduced to oxygen ions at the membrane surface exposed to the high oxygen partial pressure, $P_{O_2}^i$. Driven by the chemical potential gradient, oxygen ions and electrons counter diffuse through the bulk of the membrane. Finally, oxygen molecules were formed by recombining oxygen ions at the membrane surface exposed to the low oxygen partial pressure, $P_{O_2}^n$ and release to gas phase. Local charge neutrality is maintained by the joint diffusion of oxygen vacancies and electrons or electron holes. The net flux is determined by the species with the smallest conductivity.

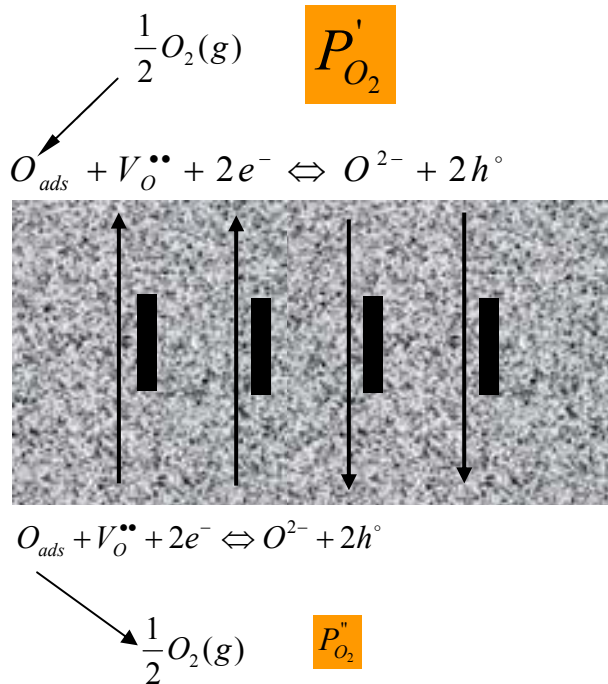


Figure 1.2 Fluxes in mixed conducting membrane under a partial pressure gradient. P'_{O_2} is the higher oxygen partial pressure, P''_{O_2} is the lower oxygen partial pressure.

The oxygen permeation flux through the perovskite membranes is essentially controlled by two factors, by (i) the rate of the oxygen ion (O^{2-}) / oxygen vacancy ($V_o^{\bullet\bullet}$) diffusion and/or the simultaneous counter flux of the charge balancing electrons (e^-) / electron holes (h°) within the bulk membrane and by (ii) the interfacial oxygen exchange on either side of the membrane, as shown in Fig. 1.3. Considering oxygen exchange between the gas phase and the oxide surface, one may distinguish many steps, like adsorption, dissociation, surface diffusion, charge transfer and incorporation in the surface layer, and reversed steps, each of these steps may impede interfacial transfer of oxygen. If the oxygen permeation is limited by the surface exchange, the oxygen permeation flux can be given:

$$j_{O_2} = k_0 c_0 \times (P'_{O_2}{}^{1/2} - P''_{O_2}{}^{1/2}) \quad (1.2)$$

or

$$j_{O_2} = k_0 c_0 \times \left(P_{O_2, s}''^{1/2} - P_{O_2, s}'^{1/2} \right) \quad (1.3)$$

where k_0 is the surface exchange coefficient, c_0 is the density of oxygen ions on the surface.

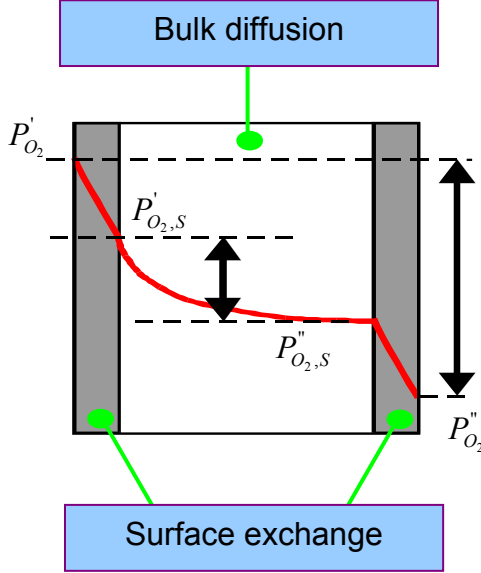


Figure 1.3 Oxygen transport through both interfaces and bulk. $P'_{O_2, s}$ and $P''_{O_2, s}$ are the virtual oxygen pressure on the interfaces of feed side and permeate side.

For a thick membrane the rate of the overall oxygen permeation is usually determined by the lattice diffusion of oxygen or the transport of electronic charge carriers through the bulk oxide. The gradient $\nabla\mu_{O_2}$ of the chemical potential of the oxygen on the two sides of the membrane is regarded as the driving force for the oxygen ion transport. Assuming ion diffusion in the bulk of the solid electrolyte as rate limiting, the oxygen potential gradient depends at a given temperature T and a membrane thickness d only on the oxygen partial pressures on the feed (air) and permeate side of the membrane, $P'_{O_2, s}$ and $P''_{O_2, s}$, respectively [19]

$$\nabla\mu_{O_2} = \frac{\mu_{O_2}'' - \mu_{O_2}'}{d} = \frac{RT}{d} \ln\left(\frac{P''_{O_2, s}}{P'_{O_2, s}}\right) \quad (1.4)$$

When the bulk diffusion is the limiting step of oxygen transport, it means that the surface reaction is so fast that a fast equilibration of the oxide surface with the imposed gas atmosphere would imply that $P_{O_2,S}' = P_{O_2}'$ and $P_{O_2,S}'' = P_{O_2}''$. Eq. (1.4) can be changed to:

$$\nabla \mu_{O_2} = \frac{\mu_{O_2}'' - \mu_{O_2}'}{d} = \frac{RT}{d} \ln \left(\frac{P_{O_2}''}{P_{O_2}'} \right) \quad (1.5)$$

For charge neutrality reasons, oxygen ion transport in one direction is accompanied by electron transport in the opposite direction. Considering the ionic and electronic conductivities σ_i and σ_e we obtain for the oxygen flux j_{O_2} through the membrane with F as Faraday constant:

$$j_{O_2} = -\frac{1}{4^2 F^2} \frac{\sigma_i \cdot \sigma_e}{\sigma_i + \sigma_e} \cdot \nabla \mu_{O_2} \quad (1.6)$$

If the oxygen ion transport occurs via oxygen vacancies (V_o^{**}) and the electron transport via electron holes (h^*), we have the case of the counter diffusion of V_o^{**} and $2h^*$.

Integration of Eq. (1.6) across the membrane thickness d using the relationship

$$\nabla \mu_{O_2} = \frac{\partial RT \ln P_{O_2}}{\partial x} \text{ yields the Wagner equation in the usual form which has general$$

validity for mixed conductors [20]

$$j_{O_2} = -\frac{RT}{4^2 F^2 d} \int_{\ln p_{O_2}^F}^{\ln p_{O_2}^P} \frac{\sigma_i \cdot \sigma_e}{\sigma_i + \sigma_e} \cdot d \ln P_{O_2} \quad (1.7)$$

In order to understand the roles of the surface exchange and bulk diffusion during the oxygen transport through the perovskite membrane, a surface exchange fluxes model was introduced. The exchange flux i_i at the perovskite membrane – gas interfaces at the inlet and outlet sides is given by [21, 22]:

$$i_i = k_{i,0} C_i (e^{n\mu_g / RT} - e^{2n\mu / RT}) \quad (1.8)$$

where $k_{i,0}$ is the surface exchange coefficient, C_i is the density of oxygen ions, n is the reaction order at the interfaces, μ is the chemical potential of the oxygen ions at the two interfaces, and μ_g is the chemical potential of the gas

$$\mu_g = RT \ln(P / P_0) \quad (1.9)$$

where P is the gas pressure and the subscript 0 indicates the standard pressure of 1.0 atm.

At the interfaces, the following reaction occurs:



Thus the reaction order, n , at the interfaces is $n = 1/2$. The exchange oxygen fluxes i_1 and i_2 at the perovskite membrane – gas interfaces at the inlet and outlet sides are given by:

$$i_1 = k_{i,0} C_i (e^{\mu_{1g}/2RT} - e^{\mu_1/RT}) \quad (1.11)$$

$$i_2 = k_{i,0} C_i (e^{\mu_2/RT} - e^{\mu_{2g}/2RT}) \quad (1.12)$$

On the other hand, the flux density is determined by the charge, conductivity and the gradient of the electrochemical potential. Therefore, the oxygen ionic flux i_i can be also described by [23]:

$$i_i = -\frac{\sigma_i}{2F} \frac{d\mu}{d\phi} \quad (1.13)$$

where ϕ is the diameter of the membrane tube, σ_i is the oxygen ion conductivity.

The oxygen ion conductivity is also determined by the oxygen ion diffusion coefficient D_i and the oxygen ion concentration C_i in the perovskites [23]

$$\sigma_i = \frac{D_i}{RT} 4F^2 C_i \quad (1.14)$$

By combining Eqs. (1.13) and (1.14) it gives the oxygen permeation flux j_{O_2} ,

$$j_{O_2} = \frac{i_i}{2F} = -\frac{\sigma_i}{4F^2} \frac{d\mu}{d\phi} = -\frac{D_i C_i}{RT} \frac{d\mu}{d\phi} \quad (1.15)$$

The normalized oxygen permeation flux j_{O_2} can be expressed as:

$$j_{O_2} = \frac{F}{\pi\phi L} \quad (1.16)$$

where L is the length of the membrane tube, $\pi\phi L$ is the membrane surface, F is the total oxygen flux through the membrane.

By combining Eqs. (1.15) and (1.16) it gives:

$$-\frac{D_i C_i}{RT} \frac{d\mu}{d\phi} = F / \pi \phi L \quad (1.17)$$

Continuity of ion flux requires that the surface exchange fluxes and the oxygen permeation flux j_{O_2} at the two interfaces match:

$$F / \pi \phi_1 L = k_{i,0} C_i (e^{\mu_{1g} / 2RT} - e^{\mu_1 / RT}) \quad (1.18)$$

$$F / \pi \phi_2 L = k_{i,0} C_i (e^{\mu_2 / RT} - e^{\mu_{2g} / 2RT}) \quad (1.19)$$

Integrating of Eq. (1.17) yields:

$$\mu_2 - \mu_1 = \frac{RTF}{\pi c_i D_i L} \ln(\phi_2 / \phi_1) \quad (1.20)$$

where ϕ_1 and ϕ_2 are the inner and outer diameters of the membrane tube

The following relation can be obtained by eliminating μ_1 and μ_2 in Eqs. (1.18) – (1.20)

$$\frac{F}{\pi c_i D_i L} \ln(\phi_2 / \phi_1) = \ln \left(\frac{\sqrt{P'_{O_2} / P_0} - F / \pi \phi_2 L C_i k_{i,0}}{\sqrt{P''_{O_2} / P_0} + F / \pi \phi_1 L C_i k_{i,0}} \right) \quad (1.21)$$

If the oxygen transport is limited by the surface exchange, $\mu_1 \rightarrow \mu_2$, so Eq. (1.21) reduces to:

$$F = \frac{\pi \phi_1 \phi_2 L c_i k_{i,0}}{\phi_1 + \phi_2} \left(\sqrt{P'_{O_2} / P_0} - \sqrt{P''_{O_2} / P_0} \right) \quad (1.22)$$

On the other hand, if the oxygen transport is limited by the bulk diffusion $\mu_1 \rightarrow \mu_{g,1} / 2$ and $\mu_2 \rightarrow \mu_{g,2} / 2$, so Eq. (1.21) changes to:

$$F = \frac{\pi L c_i D_i}{2 \ln(\phi_2 / \phi_1)} \ln(P'_{O_2} / P''_{O_2}) \quad (1.23)$$

The total oxygen flux can be expressed by:

$$F = J_{O_2} \times S \quad (1.24)$$

where J_{O_2} is the oxygen permeation flux measured in the experiment and S is the effective area of the membrane tube. If the oxygen transport is limited by the surface exchange at the interfaces, Eq. (1.22) gives:

$$J_{O_2} = \frac{\pi\phi_1\phi_2 LC_i k_{io}}{S(\phi_1 + \phi_2)} \left(\sqrt{P'_{O_2} / P_0} - \sqrt{P''_{O_2} / P_0} \right) \quad (1.25)$$

Eq. (1.25) predicts that the oxygen permeation flux (J_{O_2} , mol/cm².s) should be proportional to the pressure term $\left(\sqrt{P'_{O_2} / P_0} - \sqrt{P''_{O_2} / P_0} \right)$ if only the surface exchange is the limiting step of the oxygen transport.

On the other hand, if the oxygen transport is only limited by the bulk diffusion through the membrane, the oxygen permeation flux is given by the following formula:

$$J_{O_2} = \frac{\pi LC_i D_i}{2S \ln(\phi_2 / \phi_1)} \ln \left(\frac{P'_{O_2}}{P''_{O_2}} \right) \quad (1.26)$$

Now the oxygen permeation flux, J_{O_2} , is proportional to $\ln \left(\frac{P'_{O_2}}{P''_{O_2}} \right)$ if the limiting step is the bulk diffusion.

1.3 Applications of MIECM in oxygen permeable membrane separators and membrane reactors

1.3.1 Production of pure O₂ and O₂-enriched air

Mixed-conducting oxides with high electron and oxygen ion conductivities are applied as ceramic membranes to separate oxygen from other gases by selective permeation [22, 24, 25]. At elevated temperature, this membrane can selectively permeate oxygen rather than other gases such as nitrogen from oxygen-containing gas. The separation of oxygen through the MIECM is schematically shown in Fig. 1.2.

There is a large potential application of O₂-enriched air in order to perform enhanced combustion. Oxygen enrichment of up to 30 % has been demonstrated to provide benefits in combustion efficiency and pollution reduction [30]. O₂-enriched air with 30 – 50 % O₂ is also used in a number of industrial processes, for example in ammonia synthesis, the Claus process and the Fluidized Catalytic Cracking (FCC) catalyst regeneration [26, 27].

Another application field of O₂-enriched air is the most efficient utilization of methane in high-temperature furnaces or cement kilns [27].

There are different existing technologies for the production of O₂-enriched air. Mainly mixing air with pure O₂ is applied. Such system usually requires pure oxygen supply equipment, a control skid and a sparger which is used to mix the pure oxygen and air well. The current commercial pure oxygen supply equipment is based on cryogenic fractionation technology or pressure swing adsorption (PSA). However, these techniques require high capital and operational costs. Membrane separations have drawn great attention in air separation. Polymeric membranes that have high selectivity to oxygen and high flux are intensively studied for oxygen enrichment. However, since normal polymeric membranes generally have a low separation factor at a considerable permeability, a single-stage polymeric membrane is limited to produce oxygen purity up to 40 %. Although high oxygen purity and permeability can be achieved by increasing the feed flow rate, reducing the membrane thickness or by increasing the pressure difference, all of these actions increase the separation cost [28]. Furthermore, a high pressure difference of about 9 bar (10 bar at feed side and 1 bar on the permeate side) is needed for polymeric membranes to get reasonable oxygen fluxes, leading to high costs for the air compression. Another problem is that polymeric membranes can not be used for the recovery of heat from exhaust gas, which prevents their use in high temperature reactions or processes applications. Polymeric membranes also transport noble or inert gases like Ar or CO₂, which can be disadvantageous depending on the processes design.

Membrane development represents a frontier research area in chemical engineering, materials science and materials chemistry. The breakthrough in the wide application of organic polymer membranes in dialysis, natural gas treatment and treatment of refinery gas streams became possible through the availability of hollow fiber membranes. Consequently, increasing activities can be observed in the preparation of oxygen ion conducting membranes in a hollow fiber geometry. Examples are the pioneering papers from the groups of Li [29-33] and Galavas [34, 35] as well as the papers by Schiestel et al [36], Trunec [37], Luyten et al. [38] showing that thin walled ceramic fibers can be prepared by phase inversion spinning followed by sintering. The development of

perovskite hollow fiber membranes is expected to trigger a similar development like it was observed in the field of hollow fiber organic polymer membranes.

The principle of O₂-enriched air by using a MIEC perovskite membrane is shown in Fig. 1.4. At elevated temperatures, under a slight difference in air pressure (1 – 2 bar) O₂ can be transported through a MIEC perovskite membrane in the form of oxygen ions from the side of high air pressure to the side of low air pressure. Simultaneously, electrons are transported in the opposite direction to maintain electric neutrality. The permeated O₂ increases the O₂ concentration to typically 30 – 50 vol % in the sweep air that forms the O₂-enriched air on the low-pressure side. Therefore, the perovskite membrane combines the in situ O₂ supply with permeated O₂ and air in one unit thus simplifying the process of O₂ enrichment and reducing the operational and capital costs.

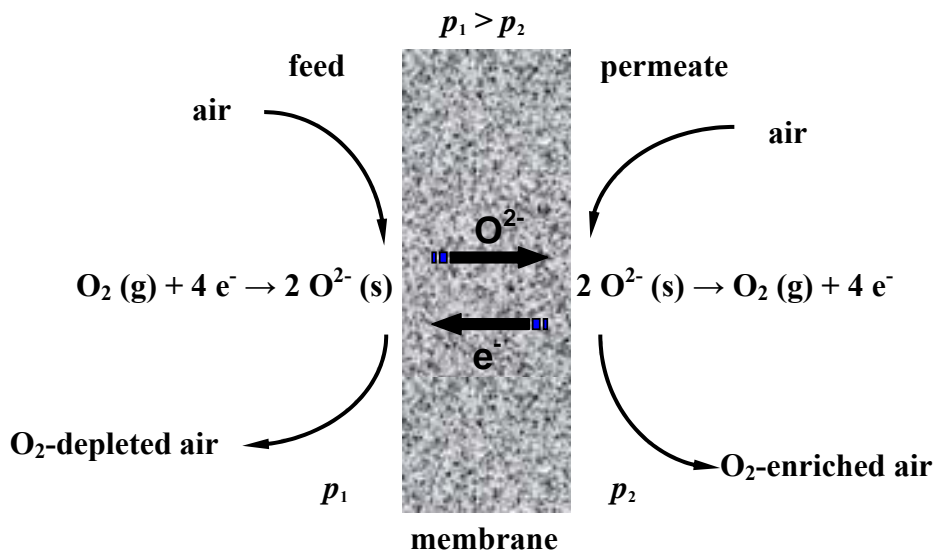


Figure 1.4 Scheme of the O₂-enrichment using perovskite mixed conducting membranes [39].

The obvious advantage of perovskite membranes is their 100 % selectivity for O₂. Moreover, compared with organic polymer hollow fiber membranes, the perovskite hollow fiber membrane requires a lower pressure difference (1 - 2 bar) across the membrane and can work at elevated temperatures thus allowing high temperature heat exchange. O₂-enriched air is used mostly in high-temperature oxidation processes such as in the generation of synthesis gas for ammonia production in which O₂-enriched air is

used to run a secondary reformer typically operated at 1000 °C to 1100 °C. Therefore, in this process the temperature required to operate the perovskite hollow fiber is already available and can be used by heat exchange. Furthermore, the heat used for the O₂ enrichment is not consumed, for example, in an endothermic reaction and can be regained by heat exchange with the product streams that leave the O₂-permeation-membrane module. A similar setup may also apply to other applications for O₂ enrichment with perovskite membranes, for example, the temperature increase of firing systems in power plants or industrial furnaces. It is noteworthy that there is no correlation between permeability and selectivity for perovskite membranes, as it is the case for polymer membranes. Increasing the pressure difference leads to an increase of oxygen permeation flux while the selectivity remains stable (100 %).

1.3.2 Partial oxidation of methane (POM) to synthesis gas

An attractive route for the utilization of the large reserves of natural gas is their conversion to syngas (CO + H₂), from which a wide variety of valuable hydrocarbons and oxygenates can be synthesized. Up to now, steam reforming (SR): $\text{CH}_4 + \text{H}_2\text{O} \rightarrow \text{CO} + 3 \text{H}_2$, $\Delta_{\text{R}}H^\circ = + 206 \text{ kJ/mol}$ at pressures between 15 - 30 bar and temperatures between 850 - 900 °C is the dominant process for producing syngas. The endothermic nature of the SR reaction, however, makes the process energy intensive. Moreover, the reaction produces syngas with a high H₂/CO ratio of 3.0, unsuitable for methanol or Fischer – Tropsch (F – T) synthesis. The slightly exothermic POM to syngas: $\text{CH}_4 + \frac{1}{2} \text{O}_2 \rightarrow \text{CO} + 2 \text{H}_2$, $\Delta_{\text{R}}H^\circ = - 36 \text{ kJ/mol}$ has captured much attention. In comparison with SR, the catalytic POM is estimated to offer costs reductions of about 30 % [40]. A further advantage is its H₂/CO ratio of about 2, which makes POM ideal for the production of syngas for the methanol or F - T synthesis. Although the POM with air as the oxygen source is a potential alternative to the SR process, the downstream requirements usually cannot tolerate the presence of nitrogen. Therefore, pure oxygen is required, and a significant part of the costs associated with conventional POM to syngas are those of the oxygen separation plant.

An alternative route that seems very promising is to use the MIEC membranes for the oxygen separation, and to combine the catalytic partial oxidation reaction and oxygen separation into a catalytic membrane reactor, as shown in Fig. 1.5. The principle of this MIECM reactor for the POM reaction is shown in Fig. 1.5. On the reaction side, methane is oxidized by surface O^{2-} and the surface oxygen is depleted; bulk O^{2-} diffuse from oxygen rich side to fill in the oxygen vacancies. On the oxygen rich side, gaseous O_2 is first reduced to O^{2-} , which diffuses towards the reaction side. The driving force is the oxygen partial pressure gradient across the membrane. The dense ceramic membrane inhibits the direct contact between the reactant and oxygen, and introduces oxygen not in the gaseous but in atomic form to the reaction chamber. This allows the complete control over the contact mode of reactants with each other, and with the catalytically active surface.

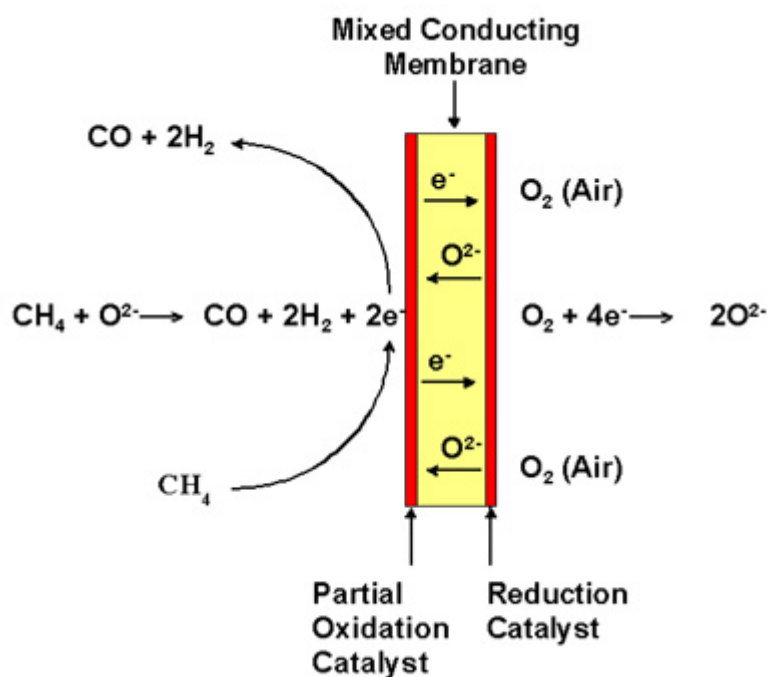


Figure 1.5 Schematic diagram of the MIECM reactor for partial oxidation of methane to syngas.

Balachandran et al [24, 41, 42] investigated POM to syngas in a $\text{La}_{0.2}\text{Sr}_{0.8}\text{Co}_{0.2}\text{Fe}_{0.8}\text{O}_{3-\delta}$ and $\text{SrCo}_{0.8}\text{Fe}_{0.2}\text{O}_{3-\delta}$ tubular membranes. They found that the membranes had broken into several pieces in a few minutes after the methane was introduced to the core side of the membrane at 850 °C. They attributed this to the stress induced by the expansion of the inside surface of the membrane tube exposed to methane, because there is higher oxygen vacancy concentration in the reducing atmosphere.

High oxygen fluxes in syngas membrane experiments with membranes of nominal composition $\text{SrFe}_{0.5}\text{Co}_{0.5}\text{O}_x$ have been reported. The material with this composition has been found to be a multi-phase system consisting of the phases $\text{Sr}_4(\text{Fe}_{1-x}\text{Co}_x)_6\text{O}_{13+\delta}$, $\text{SrFe}_{1-x}\text{Co}_x\text{O}_{3+\delta}$ and CoO [43]. Neither of these phases is stable under reducing conditions. In several papers it is demonstrated that $\text{SrFeCo}_{0.5}\text{O}_x$ shows extremely high oxygen conductivity but instability [44].

The perovskite $\text{SrCo}_{0.8}\text{Fe}_{0.2}\text{O}_{3-\delta}$ [45] exhibits a relatively high oxygen permeation rate under air/He conditions. Two types of cracks were found when the membrane made of $\text{SrCo}_{0.8}\text{Fe}_{0.2}\text{O}_{3-\delta}$ was exposed to the syngas. The first type occurred shortly after the reaction started (about 1 h) and the membrane tube in the hot reaction zone often broke into many small pieces. The second type often occurred days after the reaction, and a large crack formed parallel to the axis of the tube. They also found the first fracture was the consequence of oxygen gradient in the membrane from the reaction side to the air side, which caused a little mismatch inside the membrane, leading to the fracture. The second type of fracture was the result of a chemical decomposition.

Tsai et al [3] reported that $\text{La}_{0.2}\text{Ba}_{0.8}\text{Co}_{0.2}\text{Fe}_{0.8}\text{O}_{3-\delta}$ shows higher oxygen permeation flux and would be much more stable than $\text{La}_{0.2}\text{Sr}_{0.8}\text{Co}_{0.2}\text{Fe}_{0.8}\text{O}_{3-\delta}$. The authors successfully used membranes of the latter composition in syngas generation experiments for 850 h at 850 °C, albeit that XRD, EDXS and SEM analysis after the experiments revealed morphological and compositional changes of the membrane surfaces. Also it is noteworthy that a five fold increase in the oxygen permeation flux. The maximum value of 4.3 mL/cm².min was observed when the 5 % Ni/Al₂O₃ catalyst was packed on the membrane surface at the reaction side. This observation demonstrates that the catalyst is critical to deplete oxygen at the immediate membrane surface in order to accomplish a high oxygen

potential gradient for oxygen transport.

H. Dong et al. [46] successfully operated a reactor for conversion of methane to syngas in the membrane reactor made of $\text{Ba}_{0.5}\text{Sr}_{0.5}\text{Co}_{0.8}\text{Fe}_{0.2}\text{O}_{3-\delta}$ for more than 500 h. A stable oxygen flux of $11.5 \text{ mL/cm}^2\cdot\text{min}$ was observed. Though TPR experiments demonstrated that the material is not stable under the syngas atmosphere, facile kinetics of phase changes in this material prevented the membrane forming fracturing.

The membrane reactor based on $\text{BaCo}_x\text{Fe}_y\text{Zr}_z\text{O}_{3-\delta}$ [5] was used for partial oxidation of methane to syngas successfully. Not only was a short induction period of 2 h obtained, but also a high catalytic performance of 96 - 98 % CH_4 conversion, 98 - 99 % CO selectivity and an oxygen permeation flux of $5.4 - 5.8 \text{ mL/min}\cdot\text{cm}^2$ were achieved at $850 \text{ }^\circ\text{C}$. Above all, the membrane reactor can be steadily operated for more than 2200 h. After the reaction, XRD, XPS and EDS showed that no interaction between the membrane material and catalyst took place.

1.3.3 Oxidative coupling of methane (OCM)

Oxidative coupling of methane is a promising process for direct conversion of natural gas into more useful products such as C_2 hydrocarbons (ethylene and ethane). Using different catalysts [47, 48] in a temperature region $700 - 900 \text{ }^\circ\text{C}$ mainly three reactor concepts have been evaluated: co-feeding of CH_4 and O_2 , periodic reactor operation and reactor with MIEC membrane. The major challenge for the commercialization of OCM process is that C_2 yield is still not high enough. High C_2 yield can be realized by either increasing methane conversion, C_2 selectivity or both of them. However, higher methane conversion often leads to lower C_2 selectivity. In the classical co-feed mode the C_2 yields are less than 20 - 30 % because of undesired gas-phase combustion reaction.

The C_2 selectivity of OCM in membrane reactor is found significantly higher than that obtained in conventional co-feed reactors [49-51]. However, the reported yields are still low, generally below 20 %. OCM reaction was investigated in a tubular dense membrane reactor with $\text{Bi}_{1.5}\text{Y}_{0.3}\text{Sm}_{0.2}\text{O}_{3-\delta}$ MIEC membrane [52] and a high C_2 yield of 35 % at a C_2 selectivity of 54 % was achieved. Other examples for MIEC membranes used in the OCM

reaction are $\text{LaSrCoFeO}_{3-\delta}$ [53], $\text{LaBaCoFeO}_{3-\delta}$ [54], $\text{BaSrCoFeO}_{3-\delta}$ [55] of different chemical compositions. The C_2 selectivity is around 70 - 90 % when CH_4 conversion is lower than 10 %.

The mechanism proposed for the OCM reaction using MIEC perovskites as oxygen transporting is shown in Fig. 1.6. First the reaction of methane with lattice oxygen and electron holes gives the CH_3 radicals, water and an oxygen vacancy: $2\text{CH}_4 + \text{O}_\text{O}^\times + 2h^\circ \rightarrow 2\text{CH}_3 \cdot_{(ads)} + \text{H}_2\text{O} + \text{V}_\text{O}^{\bullet\bullet}$. The two $\text{CH}_3 \cdot$ radicals form ethane which can react again with lattice oxygen and electron holes giving ethylene, water and oxygen vacancy: $\text{C}_2\text{H}_6 + \text{O}_\text{O}^\times + 2h^\circ \rightarrow \text{C}_2\text{H}_4 + \text{H}_2\text{O} + \text{V}_\text{O}^{\bullet\bullet}$. Deeper oxidation of the C_1 and C_2 to CO_x can be achieved when the lattice oxygen is not completely consumed: $2\text{O}_\text{O}^\times + 4h^\circ \rightarrow \text{O}_{s(gas)} + 2\text{V}_\text{O}^{\bullet\bullet}$. Therefore the methane conversion is increased but the C_2 selectivity decreases when the oxygen transport through the membrane is too high.

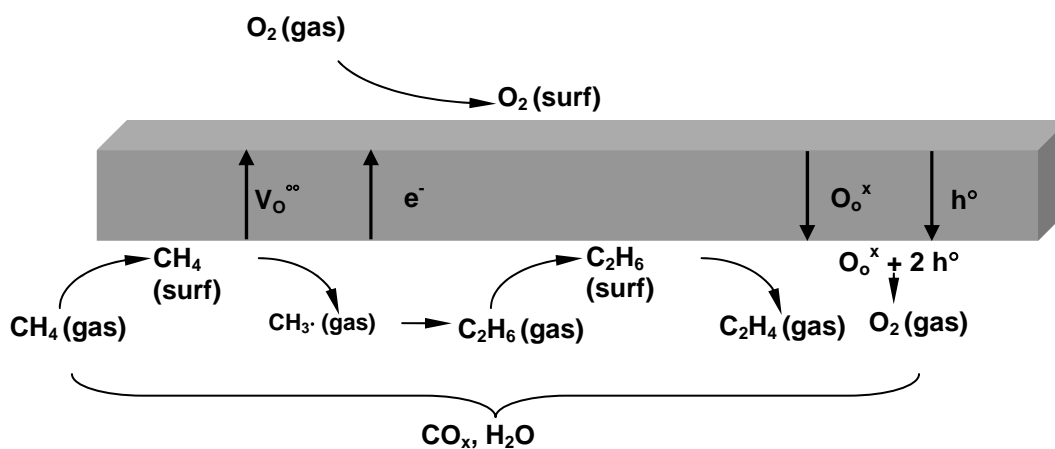


Figure 1.7 Possible mechanism of the OCM in a perovskite membrane reactor [56].

In conclusion the MIEC membrane reactor could improve the C_2 selectivity of OCM reaction. However, there is a long way to go for the MIEC membrane used in the commercial OCM process. The challenge is to develop the membrane material, which possesses both excellent OCM catalytic performance and sufficient oxygen permeation at the reaction temperature.

1.3.4 Oxidative dehydrogenation of light alkanes to olefins

Ethylene and propylene are currently produced by the thermal cracking of ethane, ethane-propane mixture, or naphtha [57], which is a highly endothermic and energy consumption intensive process with extensive coke formation. To overcome these problems, oxidation activation of alkanes such as the oxidative dehydrogenation of ethane to ethylene (ODE) is considered as an attractive alternative to the current thermal steam cracking process [58, 59]. In addition to the fall away of any thermodynamic limitation of the conversion, lower operating temperatures and less coke formation are expected. Unfortunately, the yields attained so far in conventional co-feed reactors still remain too low for industrial application because ethane reaction with oxygen results in the thermodynamically favored formation of carbon oxides. In order to increase the selectivity for ethylene at a given conversion, a controlling of the contact mode of reactants is necessary.

Dense mixed oxygen ion and electron conducting membranes offer a beneficial contact medium for the oxidative dehydrogenation. The advantage of the dense ceramic membrane reactor is that oxygen (air) is not co-fed with ethane, which avoids the formation of carbon oxides due to direct reactions between ethane and oxygen, thus higher ethylene selectivities can be expected. H. Wang et al. reported the ODE using planar and tubular oxygen permeable mixed ion and electron conducting membranes made of $\text{Ba}_{0.5}\text{Sr}_{0.5}\text{Co}_{0.8}\text{Fe}_{0.2}\text{O}_{3-\delta}$ (BSCF) [12, 13]. The ethylene selectivity of 80 % for an ethane conversion of 84 % was achieved at 800 °C. Rebeilleau et al. [60, 61] also investigated the ODE in the BSCF catalytic membrane reactor. At 807 °C, an ethylene yield of 66 % was obtained in the membrane reactor. After Pd cluster deposition, the ethylene yield reached 76 % at 777 °C. However, Ni cluster deposition led to a decrease of ethane conversion compared to the bare membrane without changing ethylene selectivity. Akin and Lin found that per pass ethylene yield of 56 % with an ethylene selectivity of 80 % was achieved in a dense tubular ceramic membrane reactor made of $\text{Bi}_{1.5}\text{Y}_{0.3}\text{SmO}_3$ (BYS) at 875 °C [14].

Compared with the ODE in MIEC membrane reactors, there are only a few papers on the oxidative dehydrogenation of propane (ODP). Using a $\text{Ba}_{0.5}\text{Sr}_{0.5}\text{Co}_{0.8}\text{Fe}_{0.2}\text{O}_{3-\delta}$ perovskite

and a diluted feed (90 % inert, 10 % propane), propylene selectivities of 44.2 % were found which was much higher than the selectivities in corresponding co-feed reactor experiments at similar propane conversions (23 - 27 %) [62]. At low propane conversions (5 %), the propylene selectivity was found to be 52 %. These results show that in contrast to the ODE, the ODP on MIEC membrane supported dehydrogenation of propane are below those in the co-feed reactor.

The catalyst may be either the membrane surfaces itself or another material deposited on the top of the membrane. The promising feature of perovskite membranes is that the oxygen permeation flux may alter the relative presence of different oxygen species on the membrane surface [63], thereby providing especially lattice oxygen species that may be more selective for partial oxidation reactions than gas phase oxygen. The principle of a dense oxygen-permeable membrane for the selective oxidation of hydrocarbons is shown in Fig. 1.7. Under an oxygen partial pressure gradient across the membrane, oxygen is driven from the air side to the reaction side (hydrocarbon) as lattice oxygen (O^{2-}). Local charge neutrality is maintained by the counter-current diffusion of oxygen ions (or oxygen vacancies) and electrons (or electron holes). Since lattice oxygen converted from O_2 by the oxygen permeation membrane is continuously supplied to the reaction side, the selectivity of the oxidation reaction can be controlled by fine tuning of the oxygen and hydrocarbon fluxes to a high level.

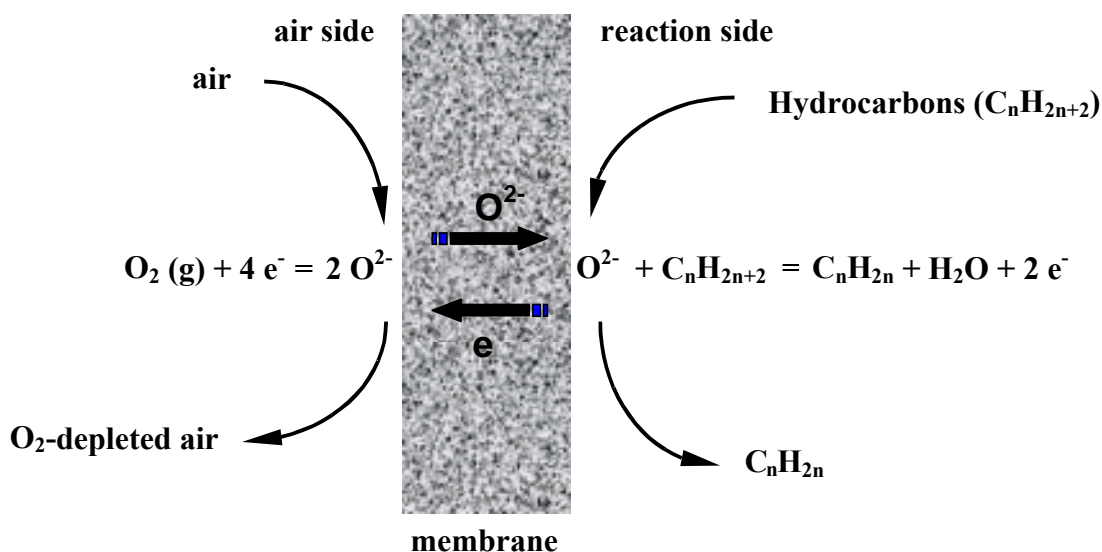


Figure 1.7 Mechanistic scheme of selective oxidation of hydrocarbons in a dense oxygen permeable membrane reactor.

1.3 Aim of the thesis

In order to develop the ceramic membrane system for industrial applications, it is essential to improve both the oxygen permeation flux and the membrane configuration such as flat sheet [64], tubular [2] or hollow fiber [30, 35, 36]. So far, mainly disk-shaped membranes with a limited membrane area ($< 5 \text{ cm}^2$) were employed because they can be easily fabricated by a conventional pressing method. Although a multiple planar stack can be adopted to enlarge the membrane area to an industry plan scale, many problems such as high temperature sealing, the connection and the pressure resistance have to be faced [64]. Tubular membranes were developed to reduce the engineering difficulties, especially the problems associated with the high temperature sealing [4], but their small surface area to volume ratio and their relative thick wall leading to a low oxygen permeation flux, make them unfavorable in practice.

Hollow fiber membranes with an asymmetric cross section can solve the problems mentioned above. Such hollow fiber membranes possess much larger membrane area per unit volume for oxygen permeation (per m^3 permeator of the order of $5,000 \text{ m}^2$) [30, 35,

36]. Furthermore, the resistance of the membrane to oxygen permeation is very much reduced due to the thinner wall and the asymmetric structure which increases the membrane surface area for oxygen surface exchange. Therefore, it is expected that asymmetric hollow fiber membranes can give higher permeation fluxes than other membrane geometries. By adopting a long hollow fiber and keeping the two sealing ends away from the high temperature zone, the problem of high temperature sealing no longer exists.

The purpose of this thesis is to develop the perovskite hollow fibre membrane reactor for production of O₂-enriched air, POM to syngas and ODE reaction. Therefore the hollow fibre membrane based on BaCo_xFe_yZr_zO_{3-δ} (BCFZ) material will be used to construct a reactor for selective oxidation of CH₄ and C₂H₆. Chapter 2 describes the experimental method for the preparation and characterization of the disc and hollow fiber perovskite membranes and construction of the hollow fiber membrane reactor for partial oxidation of methane to syngas and oxidative dehydrogenation of ethane to ethylene. Chapter 3 presents a study of the oxygen permeation flux through BCFZ hollow fiber membrane and a comparison of the oxygen permeation flux of the hollow fiber membrane to the oxygen permeation flux of the disc membrane prepared from the same material. In chapter 4, further investigation on the same material for production of O₂-enriched air is achieved. In chapter 5, a hollow fiber membrane reactor for partial oxidation of methane to syngas using Ni-based steam reforming (SR) catalyst is developed. Chapter 6 presents the selective oxidation of C₂H₆ and CH₄ over a mixed ionic and electronic conducting perovskite membrane.

1.4 Bibliography

- [1] M. Liu, A. V. Joshi, Y. Shen, K. Krist, U. S. Patent 5,273,628 (1993).
- [2] H. H. Wang, Y. Cong, W. S. Yang, J. Membr. Sci. 210 (2002) 259.
- [3] C. Y. Tsai, A. G. Dixon, W. R. Moser, Y. H. Ma, AIChE J. 43 (1997) 2741.
- [4] U. Balachandran, J. T. Dusek, P. S. Maiya, B. Ma, R. L. Mieville, M. S. Kleefish, C. A. Udovich, Catal. Today 36 (1997) 117.

- [5] J. H. Tong, W. S. Yang, R. Cai, B. C. Zhu, L. W. Lin, *Catal. Lett.* 78 (2002) 129.
- [6] T. Ishihara, Y. Tsuruta, T. Todaka, H. Nishiguchi, Y. Takita, *Solid State Ionics* 152 (2002) 709.
- [7] S. Xu, W. J. Thomson, *AIChE J.* 43 (1997) 2731.
- [8] J. E. Elshof, H. J. M. Bouwmeester, H. Verweij, *Appl. Catal. Gen. A* 130 (1995) 195.
- [9] Y. Zeng, Y. S. Lin, *J. Catal.* 193 (2000) 58.
- [10] Y. P. Lu, A. G. Dixon, W. R. Roser, Y. H. Ma, U. Balachandran, *J. Membr. Sci.* 170 (2000) 27.
- [11] F. T. Akin, Y. S. Lin, *AIChE. J.* 48 (10) (2002) 2298.
- [12] H. H. Wang, Y. Cong, W. S. Yang, *Chem. Commun.* 14 (2002) 1468.
- [13] H. H. Wang, Y. Cong, W. S. Yang, *Catal. Lett.* 84 (2002) 101.
- [14] F. T. Akin, Y. S. Lin, *J. Membr. Sci.* 209 (2002) 457.
- [15] N. Miura, Y. Okamoto, J. Mamaki, K. Morinaga, N. Yamazoe, *Solid State Ionics* 79 (1995) 195.
- [16] Y. Teraoka, H. M. Zhang, S. Furukawa, N. Yamazoe, *Chem. Lett.* (1985) 1743.
- [17] Y. Teraoka, T. Nobunaga, N. Yamazoe, *Chem. Lett.* (1988) 503.
- [18] V. M. Goldschmidt, *Skrifer Norske Videnskaps-Akad. Oslo, I. Mat.-Nat. Kl.* 8, 1926.
- [19] C. G. Guizard, A. C. Julbe, in: *Recent Advances in Gas Separation by Microporous Ceramic Membranes, part VI*, (ed. by N. K. Kanellopoulos), Elsevier (2000), 435.
- [20] H. J. M. Bouwmeester, A. J. Burggraaf, in: *Fundamentals of Inorganic Membrane Science and Technology* (eds. A. J. Burggraaf and L. Cot), Elsevier, (1996), 435.
- [21] S. Kim, Y. L. Yang, R. Christoffersen, A. J. Jacobson, *Solid State Ionics* 109 (1998) 187.
- [22] S. Kim, Y. L. Yang, A. J. Jacobson, B. Abeles, *Solid State Ionics* 106 (1998) 189.
- [23] A. Thursfield, I. S. Metcalfe, *J. Mater. Chem.* 14 (2004) 2475.
- [24] U. Balachandran, J. T. Dusek, R. L. Mieville, R. B. Poepfel, M. S. Kleefisch, S. Pei, T. P. Kobylinski, C. A. Udovich, A. C. Bose, *Appl. Catal. Gen. A* 133 (1995)

- 19.
- [25] S. Diethelm, J.V. Herle, *J. Eur. Ceram. Soc.* 24 (2004) 1319.
- [26] D. P. Bhasin, M. S. Liebeison, G. J. Chapman, *Hydrocarbon Process* 62 (1983) 85.
- [27] Baker R. *Membrane Technology in the Chemical Industry: Further directions.* in: Nunes S P, Peinemann KV. *Membrane Technology in the Chemical Industry*, Wiley-VCH, 2001.
- [28] R. Spillman, *Membr. Sci. Tech. Series*, 2 Elsevier, 1996.
- [29] X. Y. Tan, Y. T. Liu, K. Li, *AIChE J.*, 51 (2005) 1991.
- [30] X. Y. Tan, Y. T. Liu, K. Li, *Ind. Eng. Chem. Res.* 44 (2005) 61.
- [31] X. Y. Tan, S. M. Liu, K. Li, *J. Membr. Sci.* 88 (2001) 87.
- [32] S. M. Liu, X. Y. Tan, K. Li, R. Hughes, *J. Membr. Sci.* 193 (2001) 249.
- [33] S. M. Liu, K. Li, R. Hughes, *Mater. Res. Bull.* 39 (2004) 119.
- [34] S. M. Liu, G. R. Gavalas, *J. Membr. Sci.* 246 (2005) 103.
- [35] S. M. Liu, G. R. Gavalas, *Ind. Eng. Chem. Res.* 44 (2005) 7633.
- [36] T. Schiestel, M. Kilgus, S. Peter, K. J. Caspary, H. Wang, J. Caro, *J. Membr. Sci.* 258 (2005) 1.
- [37] M. Trunec, *J. Eur. Ceram. Soc.* 24 (2004) 645.
- [38] J. Luyten, A. Buekenhoudt, W. Adriansens, J. Coymans, H. Weyten, F. Servaes, R. Leysen, *Solid. State Ionics* 135 (2000) 637.
- [39] C. Hamel, A. S. Morgestern, T. Schiestel, S. Werth, C. Tablet, J. Caro, H. Wang, *AIChE J.*, in revised version.
- [40] A. Koh, L. Chen, B. Johnson, T. Khimyak, W. Leong, J. Lin, *Int. J. Hydrogen Engery*, in press.
- [41] U. Balachandran, J. T. Dusek, S. M. Sweeney, R. B. Poeppel, R. L. Mieville, P. S. Maiya, M. S. Kleefisch, S. Pei, T. P. Kobylinski, C. A. Udovich, A. C. Bose, *Am. Ceram. Soc. Bull.* 74 (1995) 71.
- [42] U. Balachandran, J. T. Dusek, P. S. Maiya, B. Ma, R. L. Mieville, M. S. Kleefisch, C. A. Udovich, *Catal.Today* 36 (1997) 265.
- [43] H. Fjellag, B. C. Hauback, R. Bredesen, *J. Mat. Chem.* 7 (1997) 2415.
- [44] P. V. Hendriksen, *Lecture on 4th Intern. Conf. Catalysis in Membrane Reactors*,

- Zaragoza, Spain, July 3-5, 2000 and B. Ma, U. Balachandran, *Mat. Res. Bull.* 33 (1998) 223.
- [45] S. Pei, M. S. Kleefisch, T. P. Kobylinski, J. Faber, C. A. Udovich, V. Zhang-Mc Coy, B. Babrowski, U. Balachandran, *Catal. Lett.* 30 (1995) 201.
- [46] V. D. Sokolovskii, E. A. Mamedov, *Catal. Today* 14 (1992) 415.
- [47] M. Baerns, G. Grubert, E. V. Kondratenko, D. Linke, U. Rodemerk, *Oil Gas Europ. Magaz.* 1 (2003) 36.
- [48] B. Ebrahim, H. Abbas, H. Aziz, WO2005005042, 2004, to HRD Corp., Nat. Petrochemical Company PETR.
- [49] Y. P. Lu, A. G. Dixon, W. R. Moser, Y. H. Ma, U. Balachandran, *Catal. Today* 56 (2000) 297.
- [50] Y. Zeng, Y. S. Lin, *Ind. eng. Chem. Rev.* 36 (1997) 277.
- [51] S. Xu, W. Thomson, *AIChE J.* 43 (1997) 2731.
- [52] F. T. Akin, Y. S. Lin, *Catal. Lett.* 78 (2002) 239.
- [53] Y. Zeng, Y. S. Lin, S. L. Swartz, *J. Membr. Sci.* 150 (1998) 87.
- [54] J. E. ten Elshof, B. A. Vanhassel, H. J. M. Bouwmeester, *Catal. Today*, 25 (1995) 397.
- [55] Z. Shao, H. Dong, G. Xiong, Y. Cong, W. Yang, *J. Membr. Sci.* 183 (2001) 181.
- [56] R. Dittmeyer, J. Caro, *Handbook of Heterogeneous Catalysis*, Eds. G. Ertl, H. Knözinger and J. Weitkamp, 2006.
- [57] L. Kniel, O. Winter, K. Stork, in 'Ethylene: Keystone to the Petrochemical Industry Dekker, New York, 1980.
- [58] T. Blasco, J. M. Lopez Nieto, *Appl. Catal. A* 157 (1997) 117.
- [59] M. Banares, *Catal. Today* 51 (1999) 319.
- [60] M. Rebeilleau, A.C. van Veen, D. Farrusseng, J. Rousset, C. Mirodatos, Z. Shao, G. Xiong, *Stud. Surf. Sci. Cat.* 147 (2004) 655.
- [61] M. Rebeilleau, S. Rosini, A.C. van Veen, D. Farrusseng, C. Mirodatos, *Catal. Today* 104 (2005) 131.
- [62] H. Wang, Y. Cong, X. Zhu, W. Yang, *React. Kinet. Catal. Lett.* 79 (2003) 351.
- [63] P. J. Gellings and H. J. M. Bouwmeester, *Catal. Today* 12 (1992) 1.

- [64] L. Qiu, T. H. Lee, L. M. Liu, Y. L. Yang, A. J. Jacobson, *Solid State Ionics* 76 (1995) 321.
- [65] P. N. Dyer, R. E. Richards, S. L. Russek, D. M. Taylor, *Solid State Ionics* 134 (2000) 21.

2 Experimental

2.1 Membranes preparation

Usually, the procedure for preparing perovskite-type membranes consists of three steps: powder synthesis, shaping and sintering. Powder synthesis, as the first step, plays an important role in determining the particle size of the powder, and consequently has an influence on the microstructure of the membrane. There are many routes to synthesize powders, such as conventional solid-state reaction method (designed as SS method) and a wet chemical process that includes thermal decomposition of cyanide, metal-EDTA, chemical co-precipitation and the sol-gel process [1]. The sintering parameters (atmosphere, heating/cooling rate, highest sintering temperature and dwelling time) can obviously affect the membrane microstructure [2, 3]. The shaping process is also a very important factor.

2.1.1 Preparation of the disc membranes

The synthesis of the $\text{BaCo}_x\text{Fe}_y\text{Zr}_z\text{O}_{3-\delta}$ * (BCFZ) perovskite powder was carried out by an adapted variant of the so-called citrates method [4, 5] employing EDTA and citric acid in parallel as complex formation agents [6, 7]. Briefly, the required amounts of cation precursors were introduced as $\text{Ba}(\text{NO}_3)_2$, $\text{Co}(\text{NO}_3)_3$, $\text{Fe}(\text{NO}_3)_3$ and $\text{Zr}(\text{NO}_3)_2$ (purity > 99.5 %). The calculated amounts of the starting materials were dissolved in EDTA- $\text{NH}_3\cdot\text{H}_2\text{O}$ solution followed by addition of citric acid. The solution was kept under heating and stirring until a gel was formed. The gel was dried at 150 °C for 10 h and then calcined at 950 °C for 5 h to obtain powder with the final composition. The resulting powder was pressed into a disc under 11 MPa for 5 minutes. Green disc was then sintered at 1300 °C for 10 h air with a heating and cooling rate of 2 °C/min (Fig. 2.1). The $\text{SrCo}_{0.8}\text{Fe}_{0.2}\text{O}_{3-\delta}$ (SCF) and $\text{Ba}_{0.5}\text{Sr}_{0.5}\text{Co}_{0.8}\text{Fe}_{0.2}\text{O}_{3-\delta}$ (BSCF) oxides were synthesized using the same method.

* Because of several pending WO Patents, the exact composition of the BCFZ fiber can not be given.

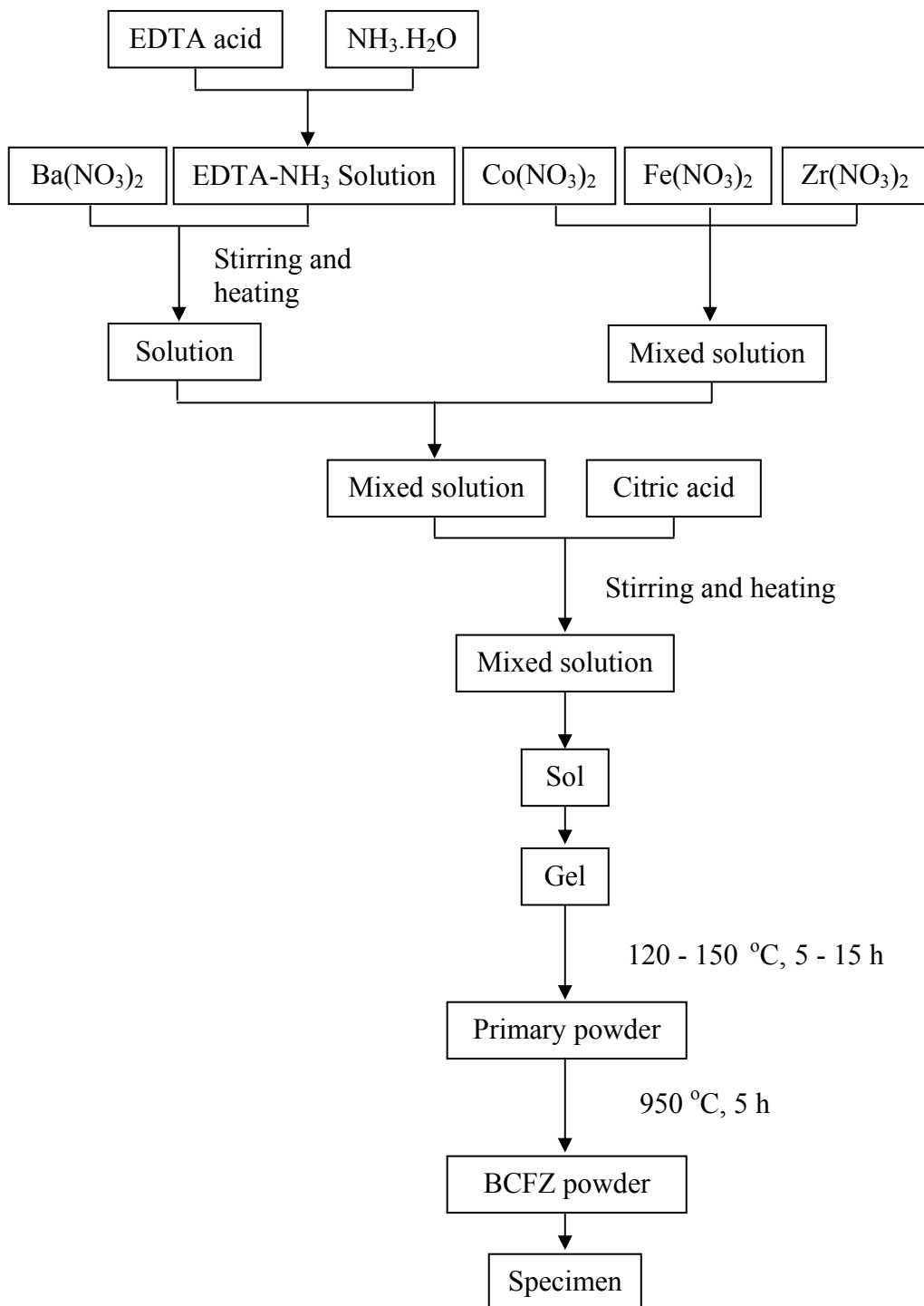


Figure 2.1 Scheme of the preparation of the BCFZ perovskite disc membrane.

2.1.2 Preparation of the hollow fiber membranes

Dense hollow fiber perovskite membranes were manufactured at Fraunhofer Institute for Interfacial Engineering and Biotechnology (IGB), Stuttgart by a phase inversion process. The BCFZ hollow fiber membrane was fabricated by a phase inversion spinning followed by sintering (Fig. 2.2). A homogeneous slurry of a polymer solution and the BCFZ powder was obtained by ball milling up to 24 hours with a solid content of 50 - 60 mass %. The slurry was spun through a spinneret and the obtained infinite green hollow fiber was cut into 0.5 m long pieces before sintering the fibers in a hanging geometry. During the calcination above 1300 °C the length and diameter of the green fiber reduced from 50 cm in length and 1mm in diameter to ~ 32 cm in length and around ~ 0.80 mm in the outer diameter [8, 9].

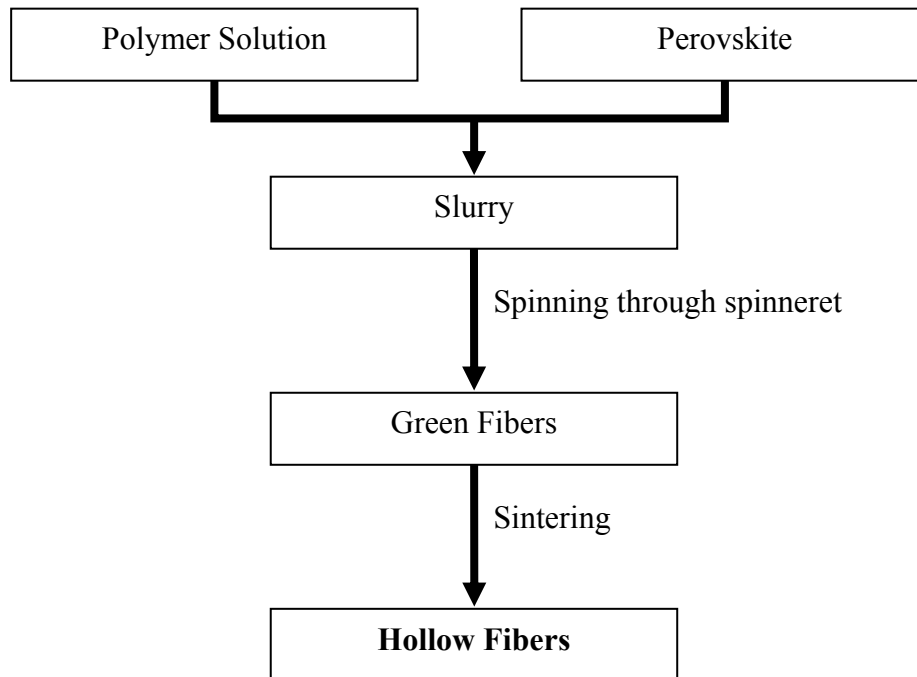


Figure 2.2 Scheme of the preparation of the perovskite hollow fiber membranes.

2.2 Structure and microstructure of the dense membranes

2.2.1 X-ray diffraction

X-ray diffraction is an extremely important technique in the field of material characterization to obtain the constitutional and structural information from crystalline materials. Single-crystal X-ray diffraction requires single crystals of appropriate size (at least 10 - 100 μm in length) and is easier to solve structures of crystals than powder technique. However, the latter one can determine the constituents of a mixture of crystalline solid phases.

The crystal structure and lattice parameters of the perovskite materials were characterized by *in situ* high-temperature X-ray diffraction (PHILIPS-PW1710) using Cu $K\alpha$ radiation. The sample was tested in a high temperature cell (Bühler HDK 2.4 with REP 2000) with a heated Pt sample holder up to 1000 $^{\circ}\text{C}$ under different atmospheres (air, 2 % O_2 in Ar and pure Ar). The heating and cooling rates amounted to 5 $^{\circ}\text{C}/\text{min}$. The total flow rate of gases through the cell was 100 mL/min. At each temperature step, the temperature was hold for 70 min. Data were collected in continuous scan mode in the range of 20 – 90 $^{\circ}$ with interval 0.05 $^{\circ}$. The peaks of Pt were used as internal standard to calculate the lattice parameters of the perovskite-type oxides.

The crystal structures of the BCFZ powder, disc and hollow fiber membrane before and after operation were characterized by X-ray diffraction (XRD, PHILIPS-PW1710) using Cu $K\alpha$ radiation (Voltage = 40 kV, Current Intensity = 40 mA).

2.2.2 Electron microscopy

For characterization of materials, electron beam methods are indispensable analytic tools. In this study, two types of methods have been involved: scanning electron microscopy (SEM) and transmission electron microscopy (TEM). X-ray microanalysis of thin specimens in the Transmission Electron Microscope offers nano-scale information on the chemistry of materials. However, the complexity of TEM designs means that the application of energy

dispersive X-ray spectrometers to the TEM is a serious technical challenge. TEM is a powerful and unique technique to reveal the internal microstructure of materials at the nanometer level.

The TEM micrographs are made by Dr. A. Feldhoff at the Institute of Physical Chemistry and Electrochemistry, University of Hanover. The microstructure of the perovskite membranes was investigated at different length scales. Secondary electron micrographs were taken on a field-emission scanning electron microscope (FE-SEM) of the type Jeol JSM-6700F at low voltages. High-resolution transmission electron microscopy (HRTEM), bright-field (BF) and dark-field (DF) imaging as well as selected area electron diffraction (SAED) was performed at 200 kV in a Jeol JEM-2100F-UHR that yields a point resolution better than 0.19 nm. An Oxford Instruments INCA-200-TEM system with an ultra-thin window was attached to the microscope that allowed for elemental analysis by energy-dispersive X-ray spectroscopy (EDXS). Prior to TEM investigations sintered powder was crushed in a mortar, ultrasonically dispersed in ethanol, and fished up with a 300 mesh copper supported holey carbon foil.

2.3 Oxygen permeation through perovskite membrane

The O₂-permeation of the BCFZ disc and hollow fiber perovskite membrane was tested in a high-temperature gas permeation cell at (i) different temperatures between 650 °C and 950 °C, (ii) different flow rates of air and sweep gas as well as (iii) different O₂-partial pressures. At the shell side air or synthetic air of different ratios of nitrogen and oxygen were used as the feed with a flow rate from 20 mL/min to 150 mL/min. Pure He (99.995 %) and Ne (>99.995 %) as internal standardization gas (constant F = 0.46 mL/min) flowed on the core side of the membrane at a flow rate varying from 10 mL/min to 100 mL/min. The inlet gas flow rates were controlled by mass flow controllers (Bronkhorst).

2.3.1 The hollow fiber membrane reactor

In the oxygen permeation measurements, two sealing techniques for the BCFZ fibers were applied: cold sealing of the fibers by silicon rubber rings outside the oven and fibers coated with an Au paste in the hot zone of the oven as shown in Fig. 2.3. The ends of the hollow fiber were coated with Au paste, after sintering at 950 °C a dense Au film was obtained. Therefore such Au-coated hollow fiber can be sealed at room temperature and the uncoated part can be kept in the middle of the oven ensuring isothermal conditions. The gases were pre-heated to 180 °C before they were fed to the permeator and all gas lines to the gas chromatograph (GC) were heated to 180 °C. The gases at the exit of the permeator were analyzed by a GC (Agilent 6890) equipped with the Carboxen 1000 column (Supelco).

The permeated O₂ concentration was determined by calibration. The total flow rate of the components in the effluent gas has been calculated from the change in the Ne concentrations before and after the permeator. Nitrogen can be also found in the effluents by gas chromatography due to slight imperfections of the sealing. The leakage of oxygen was subtracted when the oxygen permeation flux was calculated. Assuming that leakage of nitrogen and oxygen through pores or cracks is in accordance with Knudsen diffusion, the

fluxes of leaked N₂ and O₂ are related by $J_{N_2}^{Leak} : J_{O_2}^{Leak} = \sqrt{\frac{32}{28}} \times \frac{0.79}{0.21} = 4.02$. The oxygen

permeation flux was then calculated as follows:

$$J_{O_2} (mL / cm^2 \cdot min) = \left(C_{O_2} - \frac{C_{N_2}}{4.02} \right) \times \frac{F}{S} \quad (2.1)$$

where C_{O_2} , C_{N_2} are the oxygen and nitrogen concentrations calculated from GC calibration, F is the total flow rate of the outlet on the core side, which can be calculated from the change of the Ne concentrations before and after passing the permeator. S is the hollow fiber membrane area. The leakage percentage is less than 2 %.

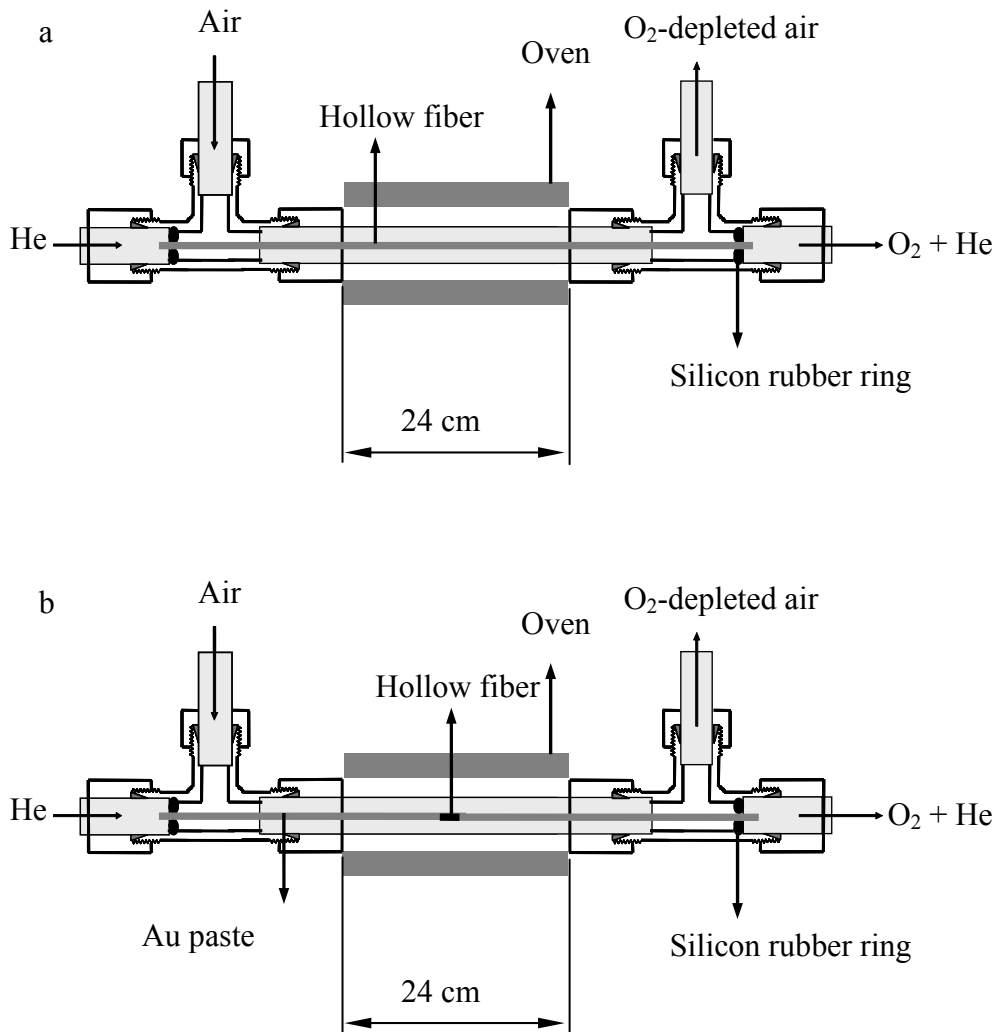


Figure 2.3 Schematic diagram of the high temperature oxygen permeation cell for a dense hollow fiber perovskite membrane: a) sealed by silicon rubber ring outside the oven and b) coated fiber with an Au paste in the hot zone of the oven.

For the determination of the effective membrane area S the following formula was used

$$S = \frac{\pi L(d_o - d_i)}{\ln(d_o / d_i)}$$

with d_o and d_i denoting the outer and inner diameters of the hollow fiber

of the effective length L , respectively. When short cm-long pieces of the hollow fiber were

sealed with the gold pasta, the whole fiber was in the isothermal zone of the oven and the effective length L for permeation is identical with the real length of the fiber. However, when 30 cm long hollow fibers in a 24 cm long oven were studied, only 16 cm were assumed as the effective fiber length L since from measuring the temperature profile of the oven it is known that only the inner 16 cm of the oven have a temperature > 600 °C.

2.3.2 The disc membrane reactor

Oxygen permeation experiments using disc membrane were realized in a vertical high temperature cell (Fig. 2.4). To seal the disc into a quartz tube a ceramic glass powder was used. The temperature was increased to 1040 °C and held for 10 minutes. The permeation experiments were performed within the temperature range of 650 – 950 °C.

During the permeation experiments, the shell side of the membranes was exposed to different air/O₂-N₂ mixtures flow rate, to pressure gradient and the sweep side was exposed to helium gas. Nitrogen was also determined in the effluents by the gas chromatograph because of the slight imperfections of the sealing, and the leakage of oxygen was subtracted in the calculation of the oxygen permeation flux. The relative leakage of O₂ was found to be less than 2 %.

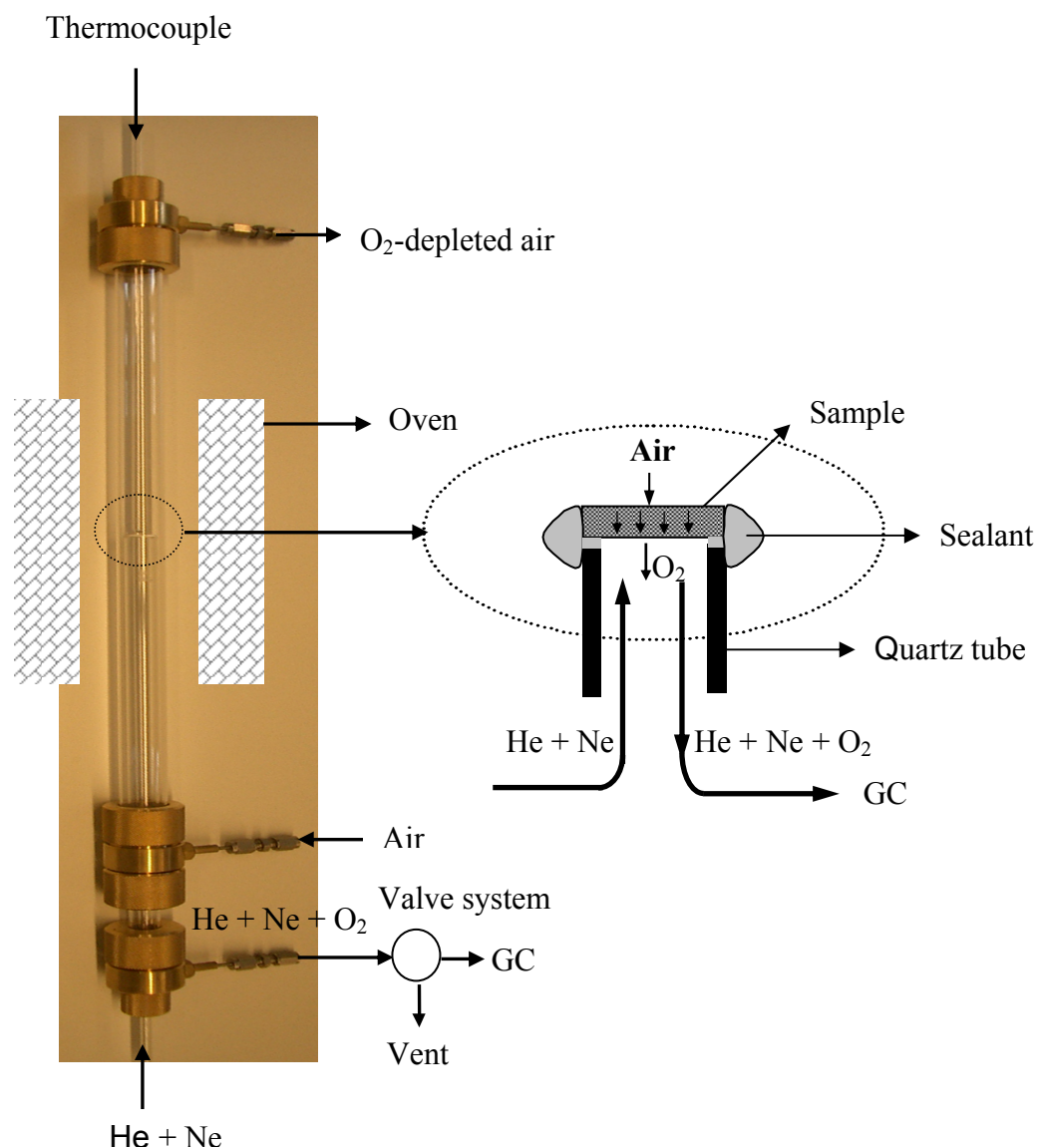


Figure 2.4 Schematic diagram of the disc membrane reactor for oxygen permeation at high temperature.

2.4 Production of O₂-enriched air

An O₂-enrichment was studied in a high temperature permeator, as shown in Fig. 2.5. The two ends of the hollow fiber membrane were sealed by two silicon rubber rings. 100 mL/min preheated air was fed to the shell side and different air pressures were obtained by adjusting the needle valve on the outlet of air. The air pressures on the shell side varied

2 Experimental

between 1.5 bar and 4.0 bar. 10 - 40 mL/min preheated air was fed to the core side and the air pressure was fixed at 1.0 bar. Due to the air pressure difference between the shell side and the core side, the O₂ on the shell side permeates through the hollow fiber membrane to the core side and mixes with air to form O₂-enriched air. The O₂ permeation rate, J_{O_2} can be calculated as

$$J_{O_2} = \frac{F_{air,inlet} \times (C_{O_2,outlet} - C_{O_2,inlet})}{S \times (100 - C_{O_2,outlet})} \quad (2.2)$$

where $F_{air,inlet}$ is the air flow rate at the inlet on the core side; $C_{O_2,inlet}$ is the fed oxygen concentration in air, $C_{O_2,outlet}$ is the O₂ concentration at the outlet of the core side; and S is the effective membrane surface area of the hollow fiber for the O₂ permeation.

The O₂-enriched air production rate, R_{OEA} , is defined as

$$R_{OEA} = \frac{F_{outlet}}{S} \Big|_{C_{O_2,outlet}} \quad \text{with } C_{O_2,outlet} > C_{O_2,inlet} \quad (2.3)$$

where F_{outlet} is the flow rate at the outlet of the core side, which can be measured by soap film meter.

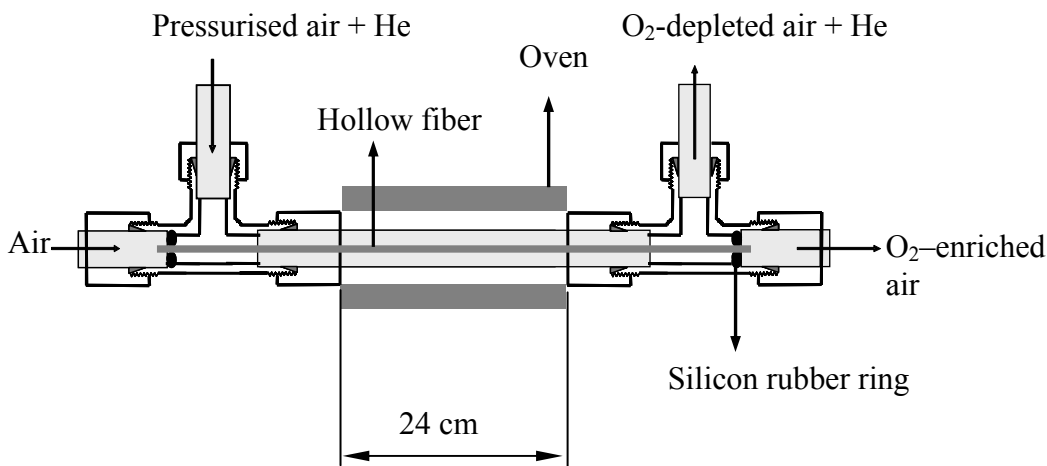


Figure 2.5 Permeator for the O₂-enrichment at high temperatures.

2.5 POM in a hollow fiber membrane reactor

Fig. 2.6 shows a schematic diagram of the membrane reactor used to perform the POM to syngas. Different types of catalyst arrangements were studied. The detailed diagrams of the membrane reactors are shown in Chapter 5. At first the hollow fiber membrane without catalyst was used. Then the modified hollow fiber membrane was used for POM to syngas. For the preparation of the slurry, the powder BCFZ (20 %), Ni-based SR catalyst (60 %) and poli-vinyl alcohol (80 % hydrolyzed) (20 %) were ball-milled for 24 h in ethanol. The hollow fiber membrane sintered at 1300 °C was coated with the slurry for 5 h, every 30 minutes and dried in air. When the the two ends of the hollow fiber were coated by Au paste, after sintering at 950 °C a dense Au film was obtained. Therefore such Au-coated hollow fiber can be sealed at room temperature and the uncoated part can be kept in the middle of the oven ensuring isothermal conditions. In the last configurations, a commercial Ni-based SR catalyst (Süd-Chemie) was packed either only around the hollow fiber membrane or around and behind the hollow fiber membrane. POM was performed at different temperatures between 800 – 950 °C, different air and methane flow rate and different methane concentration. 150 mL/min air was fed to the core side and a mixture of CH₄ and He was fed to the shell side. The gas composition at the outlet of the shell side was determined by GC (Agilent 6890 equipped with two auto valves) with a Carboxen 1000 column (Supelco). The H₂O amount was accounted based on the hydrogen atom balance. CH₄ conversion (X_{CH_4}) and products selectivities (S_i) were defined respectively as the followings:

$$X_{CH_4} = 100 - \frac{F_{CH_4}^{outlet}}{F_{CH_4}^{inlet}} \times 100\% \quad (2.4)$$

$$S_i = \frac{n_i F_i}{F_{CH_4}^{inlet} - F_{CH_4}^{outlet}} \times 100\% \quad (2.5)$$

where n_i is the number of carbon atoms in the molecules of carbon-containing products i , F_i is the flow rate of species i in mL/min.

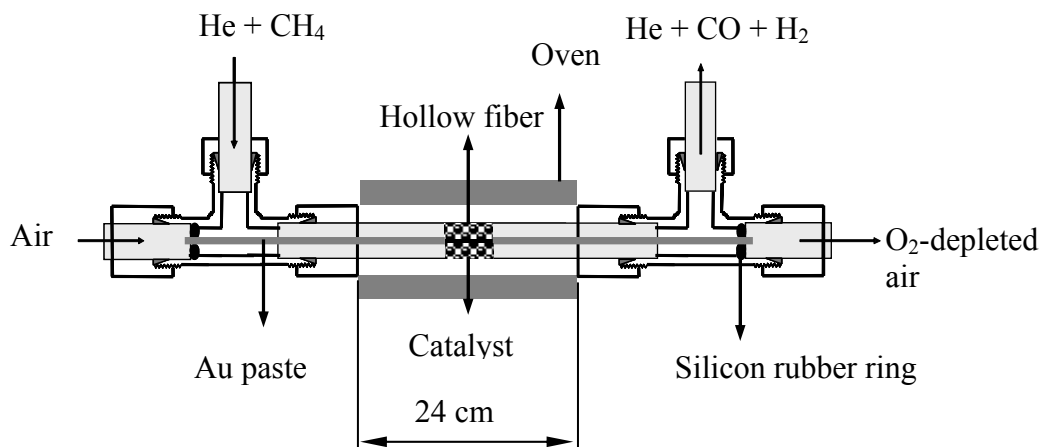


Figure 2.6 Schematic diagram of the hollow fiber membrane reactor for POM reaction.

2.6 Selective oxidations of C₂H₆ and CH₄

2.6.1 Transient experiments in the temporal analysis of products (TAP) reactor

Transient analysis of C₂H₆ and CH₄ interactions with a perovskite BCFZ formula was performed in the TAP-2 reactor of the Institute for Applied Chemistry in Berlin-Adlershof by Dr. E. Kontratenko. The TAP-2 reactor system has been described in detail elsewhere [10-12]. The pressed perovskite powder (ca. 140 mg, $d_p = 250 - 355 \mu\text{m}$) was packed between two layers of quartz of the same particle size in the micro reactor ($\varnothing_{in} \approx 6 \text{ mm}$) made of quartz. Before transient experiments the catalyst was pre-treated at ambient pressure in an O₂ flow (30 mL/min) at 875 °C for 1h. After the oxidative pre-treatment, the pre-treated catalyst was exposed to vacuum (ca. 10^{-5} Pa) and pulse experiments were carried out. Strong desorption of oxygen was observed upon catalyst exposure to vacuum. Multipulse experiments with C₂H₆ and CH₄ were performed at 875 °C and 800 °C, respectively. In these experiments, a mixture of CH₄:Ne = 1:1 or C₂H₆:Ne = 1:1 was repetitively (ca. 900 pulses) pulsed over the pre-oxidized catalyst. Pulse size of Ne was ca.

2 Experimental

$1 \cdot 10^{16}$ molecules. The following atomic mass units (AMUs) were used for mass-spectroscopic identification of different compounds: 60 (CH₃COOH), 45 (CH₃COOH, C₂H₅OH), 44 (CH₃CHO, CO₂), 43 (CH₃COOH), 31 (C₂H₅OH, CH₃OH), 30 (C₂H₆), 29 (C₃H₈, C₂H₅OH, CH₃CHO, C₂H₆), 28 (C₃H₈, C₂H₆, C₂H₄, CO₂, CO), 27 (C₃H₈, C₃H₆, C₂H₆, C₂H₄), 26 (C₂H₆, C₂H₄), 20 (Ne), 18 (H₂O) and 2 (H₂). The individual AMU's were recorded without averaging. Quantification of the results, i.e. calculation of conversion (Eq. 2.6) and selectivity (Eq. 2.7 and Eq. 2.8) values was performed for each pulse using relative sensitivities, which arise from the different ionisation probabilities of individual compounds. The relative sensitivities (S_i^r) were determined as a ratio of the areas under the response signals of each compound related to the area under the response signal of inert gas. The respective areas were corrected accordingly the contribution of fragmentation pattern of different compounds to the measured AMU signal.

$$X_i = \frac{S_{cal,i}^r - S_{exp,i}^r}{S_{cal,i}^r} \quad (2.6)$$

$$S_i = \frac{v_{educt} \times k_{product,i}}{v_{product,i} \times (k_{educt}^0 - k_{educt}^{out})} \quad (2.7)$$

$$k_i = \frac{k_{inert} \times S_{exp,i}^r}{S_{cal,i}^r} \quad (2.8)$$

$S_{exp,i}^r$ is the relative sensitivity observed over the catalytic material under study, $S_{cal,i}^r$ - the relative sensitivity determined separately for the same reactant mixture in the reactor filled with inert material of the same particle size, k_{inert} - molar fraction of inert gas in this mixture, k_{educt}^0 - molar fraction of reactant at the reactor inlet, k_{educt}^{out} - molar fraction of reactant in a pulse at the reactor outlet.

Carbon balance was calculated according to Eq. 2.9.

$$C_{balance} = \frac{\sum_i n_i \times C_i^{outlet}}{\sum_i n_i \times C_i^{inlet}} \times 100\% \quad (2.9)$$

where C_i^{outlet} and C_i^{inlet} are concentrations of gas-phase carbon-containing species at the reactor outlet and inlet, respectively n_i means the number of C atoms in the detected carbon-containing molecules.

2.6.2 Oxidation in membrane reactors

The BCFZ perovskite hollow fiber membrane, which has been successfully used for oxygen separation [8, 9, 13] has been applied for the POM reaction to syngas (CO and H₂) and the ODE reaction to ethylene. Hydrocarbons (methane or ethane) diluted with helium were fed (40 – 80 mL/min) to the sweep side, while air with a flow rate of 150 mL/min were fed to the shell side. The reaction temperature was varied from 700 °C to 925 °C.

For the ODE, ethane diluted with helium was fed to the core side, while air was fed to the shell side, as shown in Fig. 2.7. The products were analyzed by an online GC (Agilent 6890 equipped two auto valves) with Carboxen 1000 column (Supelco) which was used to separate C₂H₆, C₂H₄, CH₄, CO, CO₂, H₂, N₂ and O₂. Concentrations of these species were determined by calibrating against the standard gases of all the product species. The quantity of H₂O was accounted based on hydrogen atom balance. The oxygen permeation flux was calculated from oxygen atoms of all the oxygen-containing products. The conversion of C₂H₆, selectivities of C₂H₄, CH₄, CO₂, CO and the oxygen permeation flux in the ODE were defined as follows:

$$C_2H_6 \text{ conversion} = \frac{\frac{1}{2}F_{CO_2} + \frac{1}{2}F_{CO} + \frac{1}{2}F_{CH_4} + F_{C_2H_4}}{F_{C_2H_6}^{Feed}} \quad (2.10)$$

$$C_2H_4 \text{ selectivity} = \frac{F_{C_2H_4}}{\frac{1}{2}F_{CO_2} + \frac{1}{2}F_{CO} + \frac{1}{2}F_{CH_4} + F_{C_2H_4}} \quad (2.11)$$

$$CH_4 \text{ selectivity} = \frac{\frac{1}{2}F_{CH_4}}{\frac{1}{2}F_{CO_2} + \frac{1}{2}F_{CO} + \frac{1}{2}F_{CH_4} + F_{C_2H_4}} \quad (2.12)$$

$$CO \text{ selectivity} = \frac{\frac{1}{2}F_{CO}}{\frac{1}{2}F_{CO_2} + \frac{1}{2}F_{CO} + \frac{1}{2}F_{CH_4} + F_{C_2H_4}} \quad (2.13)$$

$$CO_2 \text{ selectivity} = \frac{\frac{1}{2}F_{CO_2}}{\frac{1}{2}F_{CO_2} + \frac{1}{2}F_{CO} + \frac{1}{2}F_{CH_4} + F_{C_2H_4}} \quad (2.14)$$

$$F_{O_2} = \frac{F_{CO} + F_{H_2O}}{2} + F_{CO_2} \quad (2.15)$$

$$J_{O_2} = \frac{F_{O_2}}{S} \quad (2.16)$$

where F_i is the flow rate of species i in mL/min, the membrane surface area S is 3.52 cm² in this study.

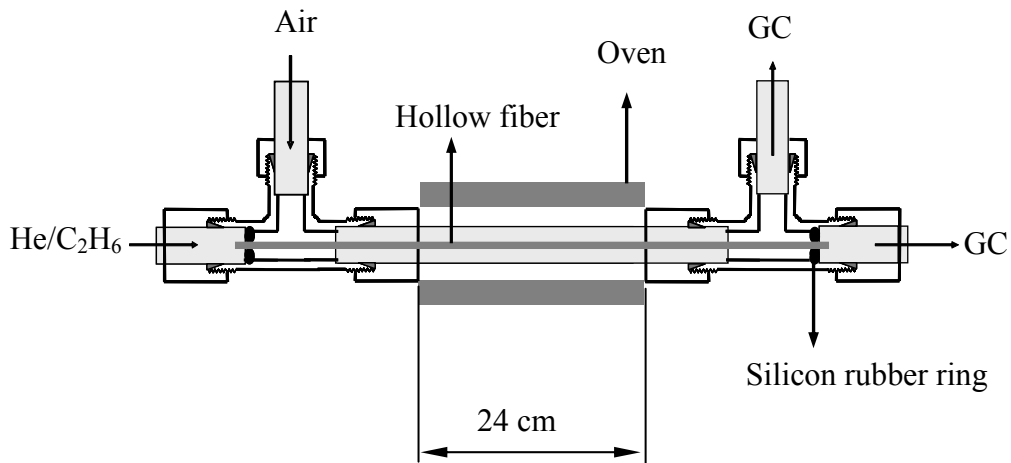


Figure 2.7 Schematic diagram of the hollow fiber membrane reactor for oxygen permeation and the ODE.

2.7 Bibliography

- [1] X. L. Cui, Y. Liu, Chem. Eng. J. 78 (2000) 206.
- [2] M. Mori, N. M. Sammes, G. A. Tompsett, J. Power Sources 96 (2000) 395.
- [3] H. H. Wang, C. Tablet, G. Grubert, A. Feldhoff, J. Caro, ICCMR-6, Lahnstein, 2004.
- [4] M. P. Pechini, US Pat. 3, 330, 697, (1967).
- [5] T. Taguchi, S. Matsura, M. Nagao, T. Choso, K. Tabata, J. Solid State Chem. 129 (1997) 60.

- [6] Z. Shao, H. Dong, G. Xiong, Y. Cong, W. Yang, *J. Membr. Sci.*, 183 (2001) 181.
- [7] Z. Shao, W. Yang, Y. Cong, H. Dong, J. Tong, G. Xiong, *J. Membr. Sci.*, 172 (2000) 177.
- [8] T. Schiestel, M. Kilgus, S. Peter, K. J. Caspary, H. H. Wang, J. Caro, *J. Membr. Sci.* 258 (2005) 1.
- [9] C. Tablet, G. Grubert, H. H. Wang, T. Schiestel, M. Schroeder, B. Langanke, J. Caro, *Catal. Today* 104 (2005) 126.
- [10] J. T. Gleaves, G. S. Yablonsky, P. Phanawadee, Y. Schuurman, *Appl. Catal. Gen. A* 160 (1997) 55.
- [11] E. Kondratenko, M. Cherian, M. Baerns, *Catal. Today* 99 (2005) 59.
- [12] E. Kondratenko, J. P. Ramirez, *Appl. Catal. Gen. A* 267 (2004) 181.
- [13] H. H. Wang, S. Werth, T. Schiestel, J. Caro, *Angew. Chem. Int. Ed.* 44 (2005) 2.

3 High oxygen permeation through MIEC hollow fiber perovskite membranes

In this chapter the manufacture, the microstructure and the oxygen permeability of the $\text{BaCo}_x\text{Fe}_y\text{Zr}_z\text{O}_{3-\delta}$ (BCFZ) hollow fiber membranes have been investigated. The oxygen permeation flux through disc and hollow fiber membranes are compared.

3.1 Membrane morphology

Fig. 3.1 shows SEM micrographs of the BCFZ hollow fiber precursor and the hollow fiber sintered above 1300 °C for 5 h. The outer diameter and the inner diameter of the hollow fiber precursor prepared are 1764 μm and 1145 μm , respectively. The cross section of the green hollow fiber shows an asymmetric columnar structure (Fig. 3.1a and Fig. 3.1e). A porous structure in the middle and denser structures at the outer surfaces were found. This asymmetric structure results from the diffusion and phase separation phenomena occurring during the spinning process. Fig. 3.1c shows the outer surface of the hollow fiber precursor. It can be seen that the BCFZ particles are well-dispersed and connected to each other by the polymer binder. After sintering, the asymmetric structure is still remained, as shown in Fig. 3.1b and Fig. 3.1f and a significant shrinkage of the hollow fiber was observed. After sintering, the geometry of the fibers was as follows: outer diameter = 800 - 900 μm , inner diameter = 500 - 600 μm , length = 30 cm (Fig. 3.2). Such shrinkage is due to the removal of the polymeric binders and the sintering of the BCFZ particles. Fig. 3.1d shows the outer surface of the sintered hollow fiber, from which it can be seen that the BCFZ particles are closely connected to each other after the removal of the organic binders.

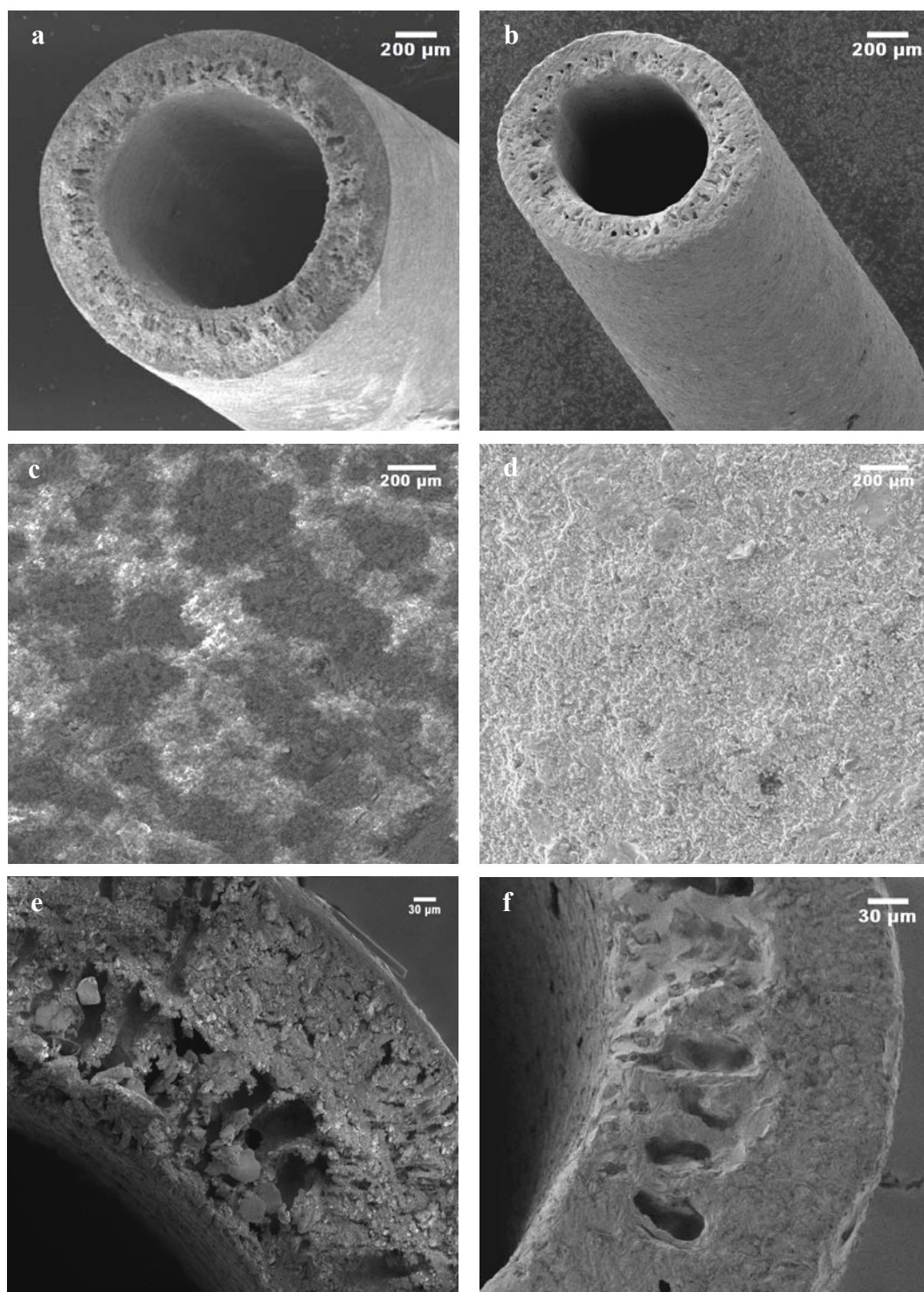


Figure 3.1 SEM micrographs of the BCFZ hollow fiber precursor (a, c, e) and the BCFZ hollow fiber after sintering (b, d, f).

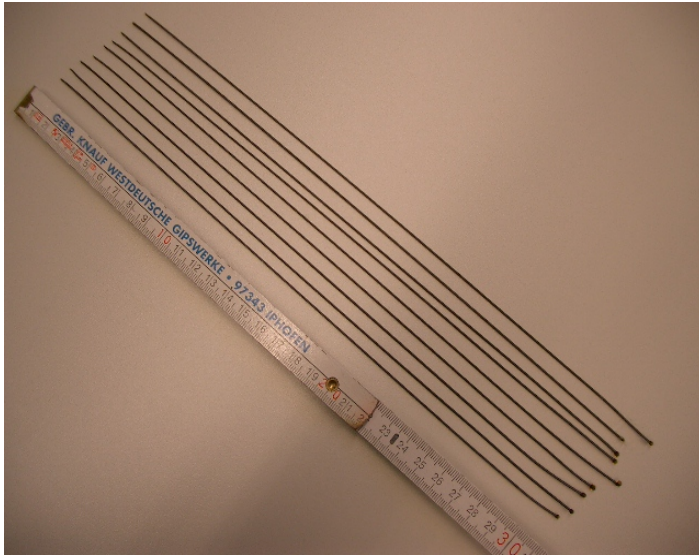


Figure 3.2 The hollow fiber perovskite membranes after sintering.

The magnification of the outer surface of the hollow fiber proved that the BCFZ membrane consists of grains of different size in the μm -region with clear grain boundaries (Fig. 3.3). Before the hollow fiber membrane was used for the oxygen permeation, the gas tightness was tested at room temperature. No nitrogen was found in the permeate side even when the nitrogen pressure on the feed side reached 5.0 bar, which proves that our hollow fiber membranes are gas tight.

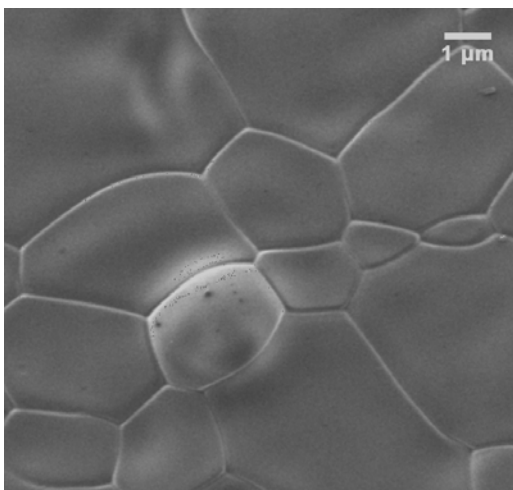


Figure 3.3 SEM of the outer surface of the sintered hollow fiber (magnification of Fig. 3.1d).

In order to increase the oxygen permeation flux, many efforts have been made to develop a thin film deposition on a porous support [1]. However, the supported thin films often suffer from compatibility problems such as the different thermal expansion coefficients of the layer and the support as well as from the solid state reaction between the two materials by diffusion processes at the operation temperature between 800 °C and 900 °C. The asymmetric hollow fiber membrane with dense perovskite layers and a porous bulk of the same materials has solved this problem. Simultaneously, the asymmetric structure can improve the mechanical strength of the hollow fiber membrane like a porous support. By measuring the three-point bending strength values a relative high value of ca. 150 MPa was found. The results show that hollow fiber membranes with an asymmetric structure not only possess an excellent oxygen permeation flux [2] but also a high mechanic strength.

3.2 Micro- and ultrastructure of grain boundaries in perovskite ceramics by transmission electron microscopy

To elucidate the real structure of membrane materials from the micrometer down to the sub-nanometer scale TEM is an indispensable tool. The usefulness of which is illustrated in the case of two model perovskite materials of practical importance.

Fig. 3.4 shows TEM investigations on the microstructure of a low-quality BCFZ ceramic sintered in disc geometry above 1200 °C. The TEM micrographs are made by Dr. A. Feldhoff at the Institute of Physical Chemistry and Electrochemistry, University of Hanover. The bright-field and dark-field micrographs in Fig. 3.4a,b reveal the size of the BCFZ grains to be of the order of 500 nm. The DF shows no indication of intergranular glass what would be clearly visible by continuous bright lines along the grain boundaries. Instead, the grain boundaries are decorated by smaller crystallites with sizes less than 100 nm that were found by SAED and EDXS to be most probably a BCFZ perovskite with a high Zr content or BaZrO₂. The diffraction pattern in Fig. 3.4c was taken of a circular region of 1.2 μm in diameter that contained perovskite grains as well as grain boundaries.

The relatively small and randomly oriented grain boundary crystals give rise to the appearance of Debye-Scherrer rings. The diameters of the best developed ones correspond to lattice plane distances of 0.3 nm and 0.18 nm that match well to the (111) and (220) planes of BCFZ perovskite with a high Zr content or BaZrO_2 , respectively. EDX spectra of the perovskite grains showed Ba, Co, Fe, Zr, and O (Fig. 3.4d).

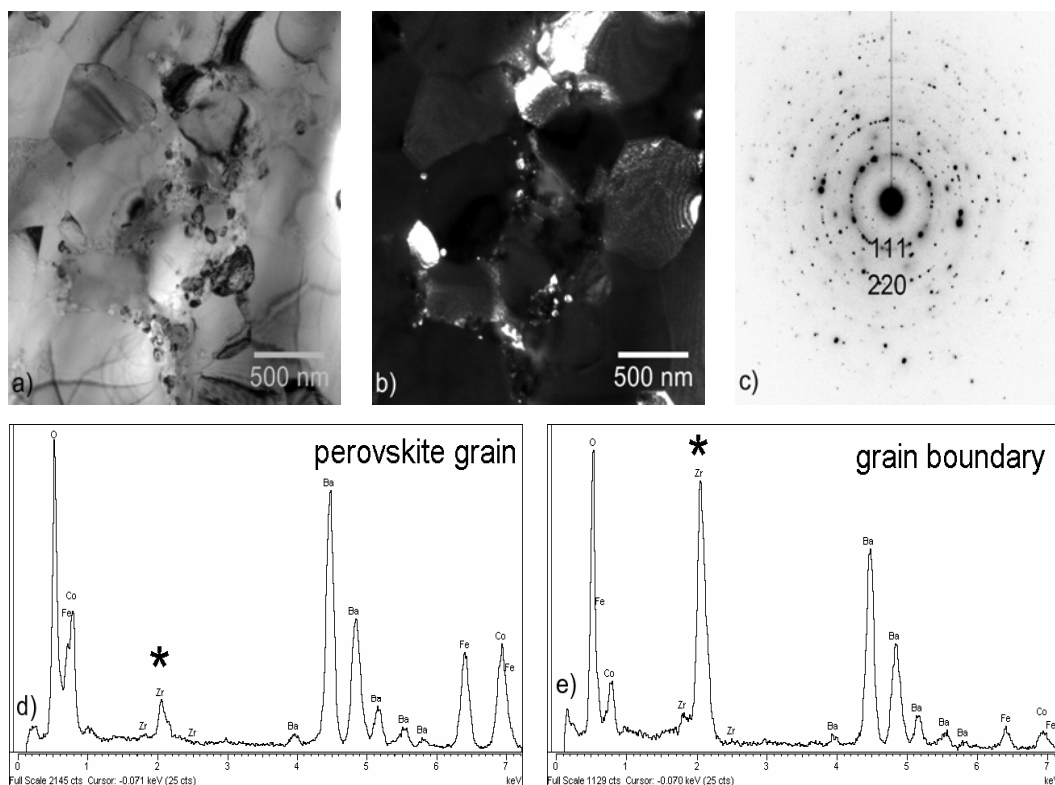


Figure 3.4 Microstructure of a BCFZ ceramic: a) TEM bright-field, b) TEM dark-field, c) selected area electron diffraction, d) EDXS of perovskite grain, e) EDXS of grain boundary region. The asterisk indicates Zr-L lines [3].

In the spectra from the grain boundary regions the Zr-L lines at around 2 keV (marked by asterisk) show up with much higher intensity, even if strong contributions of adjacent perovskite grains are still present (Fig. 3.4e). In this example even the starting BCFZ powder used for the disc preparation contained ZrO_2 as a foreign phase. Obviously, some synthesis skill is required to bring the relative large Zr^{4+} cation on the B position in the

ABO₃ perovskite structure. The two-phase characteristic of the starting powder remained after sintering the ceramic above 1200 °C.

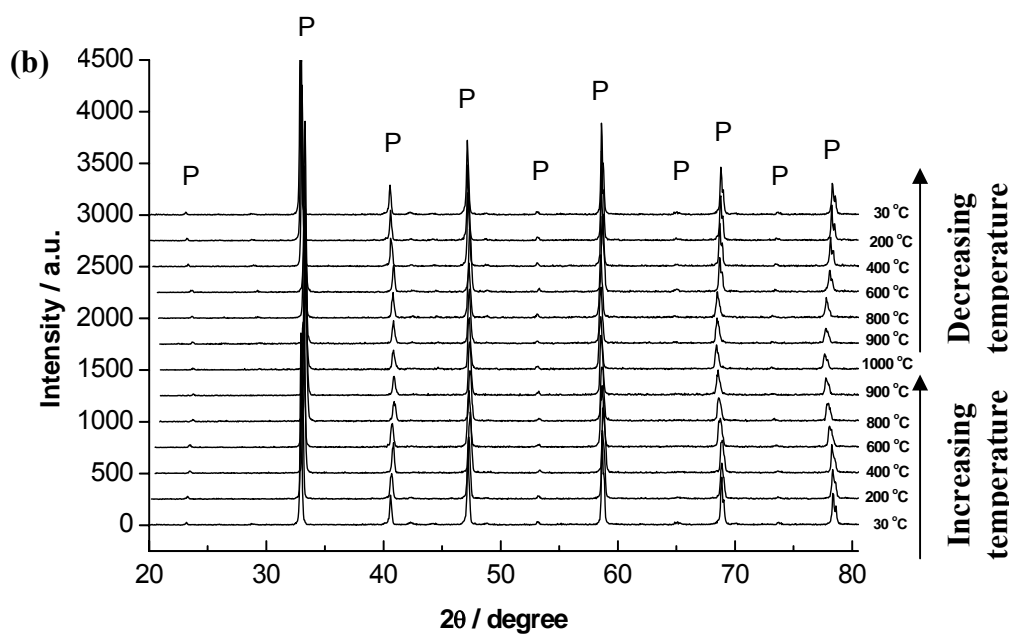
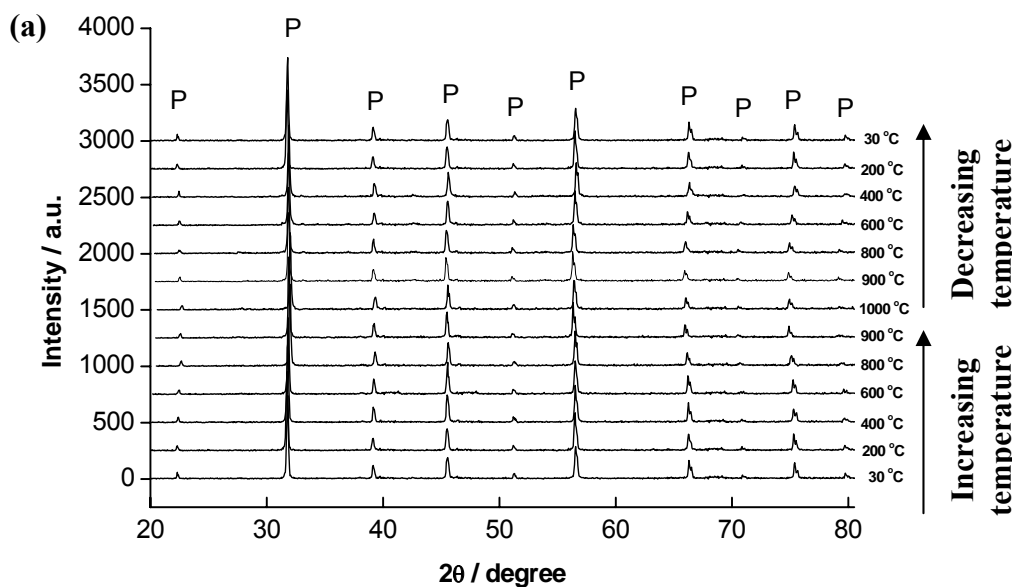
3.3 Selection of an optimum material for the hollow fiber membranes

Structure and stability of the mixed ionic and electronic conducting perovskite-type oxides can be studied very effectively by in situ high-temperature X-ray diffraction. It is a fast method to estimate the reversible stability of new mixed ionic and electronic conducting perovskite-type oxides by determining by-phases, lattice constants and thermal expansion coefficients.

The purpose is to develop an effective way for choosing and estimating mixed ionic and electronic conducting perovskite-type materials for preparation of the hollow fiber membranes. Three typical perovskite membranes, SrCo_{0.8}Fe_{0.2}O_{3-δ} (SCF) [4], Ba_{0.5}Sr_{0.5}Co_{0.8}Fe_{0.2}O_{3-δ} (BSCF) [5] and BaCo_xFe_yZr_zO_{3-δ} (BCFZ) [6] were chosen because they are widely studied and have similar compositions but different properties. SCF disc membrane has the highest reported oxygen permeation flux of 3.1 mL/cm².min at 850 °C, but its stability is poor. BSCF disc shows a high oxygen permeation flux (1.4 mL/cm².min at 950 °C) and good stability (1000 h stable operation under air/He). BCFZ disc possesses a medium oxygen permeation flux (0.9 mL/cm².min at 950 °C) but the best stability reported so far.

With increasing temperature, oxygen releases from the lattice. Accordingly, the metal ions could be reduced from a higher valence state to a lower one, and the oxygen vacancies were simultaneously formed. These effects may lead to phase transition. In situ high temperature X-ray diffraction technique provides an effective and direct way to trace the phase structure during the increasing and decreasing temperatures. Fig. 3.5 shows the XRD patterns of BSCF, SCF and BCFZ powders under air as the temperature was varied from 30 °C to 1000 °C. Under air, the XRD patterns of BSCF, SCF and BCFZ oxides at different temperatures showed that these materials remained in their perovskite structure during the temperature range studied. This behavior is reversible since the XRD patterns

during increasing and decreasing temperature, respectively, are almost the same. This means that the three perovskites exhibit good phase reversibility and structure stability under air.



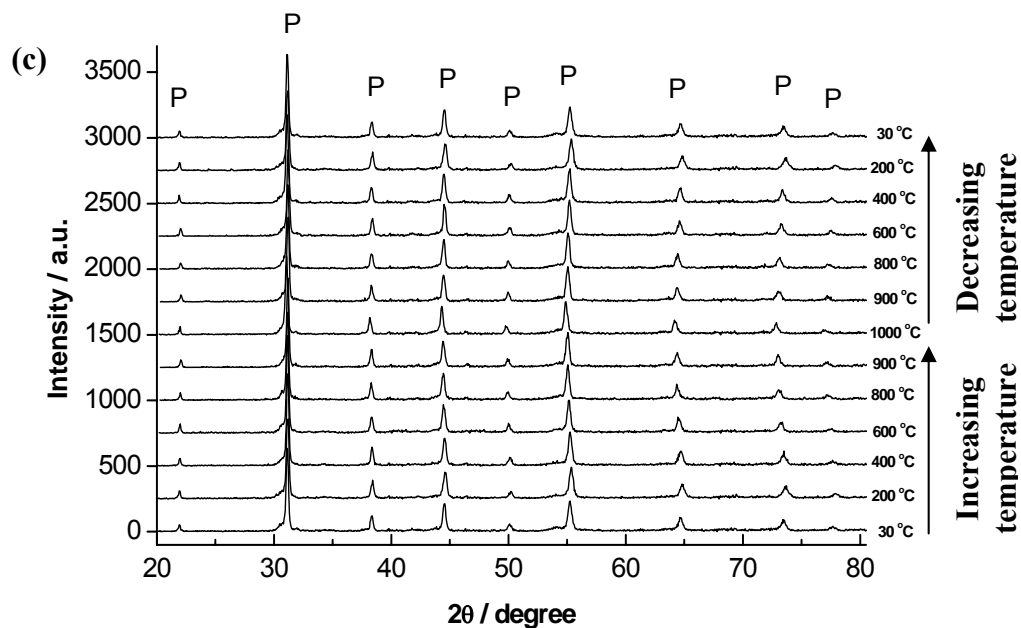
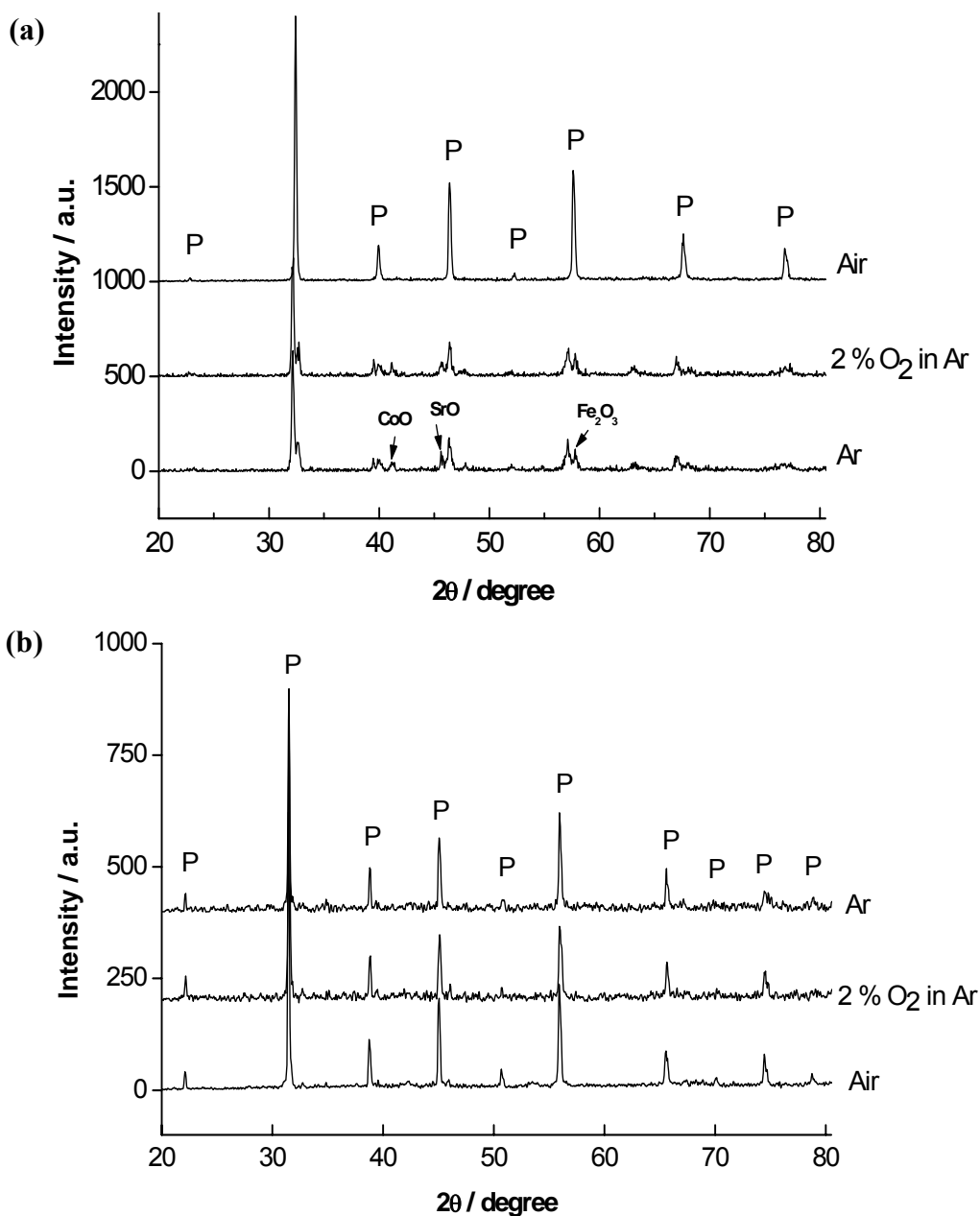


Figure 3.5 XRD patterns of the three perovskites under study during increasing and decreasing temperatures. Heating rate and cooling rate: 5 °C/ min, equilibration time at each temperature: 70 min, (a): BSCF, (b) SCF, (c) BCFZ. P: perovskite.

During the oxygen permeation operation, one side of the membrane is exposed to air (high oxygen partial pressure side); the other side of the membrane is exposed to Ar or He (low oxygen partial pressure side). Thus the phase stability of the perovskite oxides under air alone is not enough to reflect the actual stability when they are selected as candidates for oxygen separation membranes. Therefore, it is necessary to study the high temperature phase stability of the mixed ionic and electronic conducting perovskite-type oxides under low oxygen partial pressures, e.g. 2 % O₂ in Ar and pure Ar. Fig. 3.6 shows the XRD patterns of BSCF, SCF and BCFZ powders at 900 °C under different atmospheres (2 % O₂ in Ar, pure Ar and air). New XRD peaks appeared in the XRD patterns of SCF when the atmosphere was 2 % O₂ in Ar or pure Ar. Further analysis showed that a part of the perovskite has been decomposed to SrO, CoO and Fe₂O₃, as shown in Fig. 3.6a. This means that SCF exhibits poor phase stability at low oxygen partial pressures although it

3 Oxygen permeation through MIEC membranes

has good phase stability under air. It was found that the perovskite structure of SCF is thermodynamically stable only at higher oxygen pressures (> 0.1 atm) and this material has very limited chemical and structure stability at low oxygen partial pressures [7]. Pei et al. [7] found that the membrane reactor made from SCF broke into pieces when methane was fed to the reactor. These results are in accordance with these XRD results.



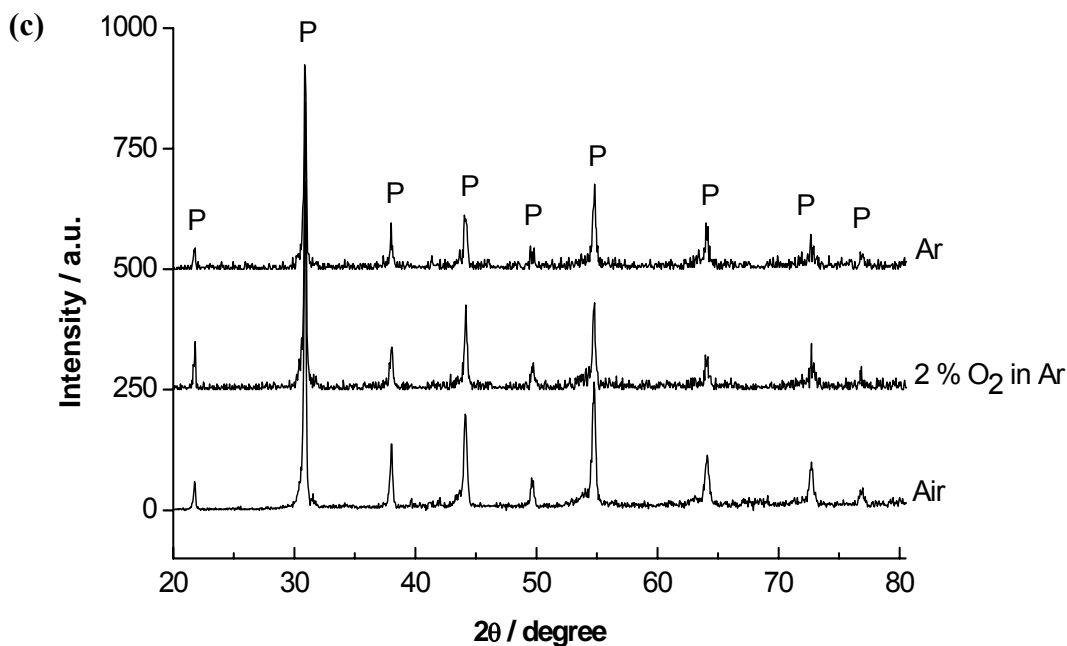


Figure 3.6 XRD patterns of the three perovskites under study in different atmospheres at 900 °C. Equilibration time: 70 min, (a) SCF, (b) BSCF, (c) BCFZ. P: perovskite.

However, BSCF and BCFZ oxides can remain their perovskite structure under both air and 2 % O₂ in Ar, and even under a pure Ar atmosphere with oxygen partial pressure $\leq 1 \times 10^{-5}$ atm (shown in Fig. 3.6b and Fig. 3.6c). These results indicate that BSCF and BCFZ possess good phase stability at high temperatures not only under air but also under low oxygen partial pressures, e.g. pure Ar. By oxygen temperature-programmed desorption technique (O₂ – TPD) Shao et al. [5] found that the substitution of strontium ions in SCF by larger barium ions could effectively suppress the oxidation of Co³⁺ and Fe³⁺ to Co⁴⁺ and Fe⁴⁺ in the lattice and stabilize the perovskite structure under low oxygen partial pressures, e.g. pure Ar. Consequently, it is reasonably understood that BSCF and BCFZ membranes can be steadily operated for a long time as reported in Refs. [5, 6].

Fig. 3.7 shows the lattice parameters of BSCF, SCF and BCFZ perovskites at various temperatures calculated based on the XRD data under air. Koster and Mertins [8] had reported X-ray powder diffraction data for BSCF. The Rietveld refined unit cell parameter

is 3.9830 Å at room temperature which is similar to our value of 3.9793 Å as shown in Fig. 3.7. This means our calculation method and measurement is believable. Among the three perovskites, the lattice parameter of BCFZ is the largest while that of SCF is the smallest. The lattice parameter of BSCF is larger than that of SCF because Ba²⁺ is larger than Sr²⁺. For the same reason, substitution of Co⁴⁺ by the larger Zr⁴⁺ should lead to an increase in the lattice parameter of BCFZ. From Fig. 3.7 it can be seen that the lattice parameters of the perovskites increase linearly with temperatures. Within the examined temperature range, the variation percents of BSCF, SCF and BCFZ were 1.1 %, 1.7 % and 1.0 %, respectively. The thermal expansion coefficients (TEC) was calculated following the definition $\frac{d(\Delta a/a_0)}{dT}$ (a: lattice constant, a₀: lattice constant at room temperature). By analyzing their lattice parameters as shown in Fig. 4.7, the TECs of BSCF, SCF and BCFZ are obtained to be $11.5 \times 10^{-6} \text{ K}^{-1}$, $17.9 \times 10^{-6} \text{ K}^{-1}$ and $10.3 \times 10^{-6} \text{ K}^{-1}$, respectively.

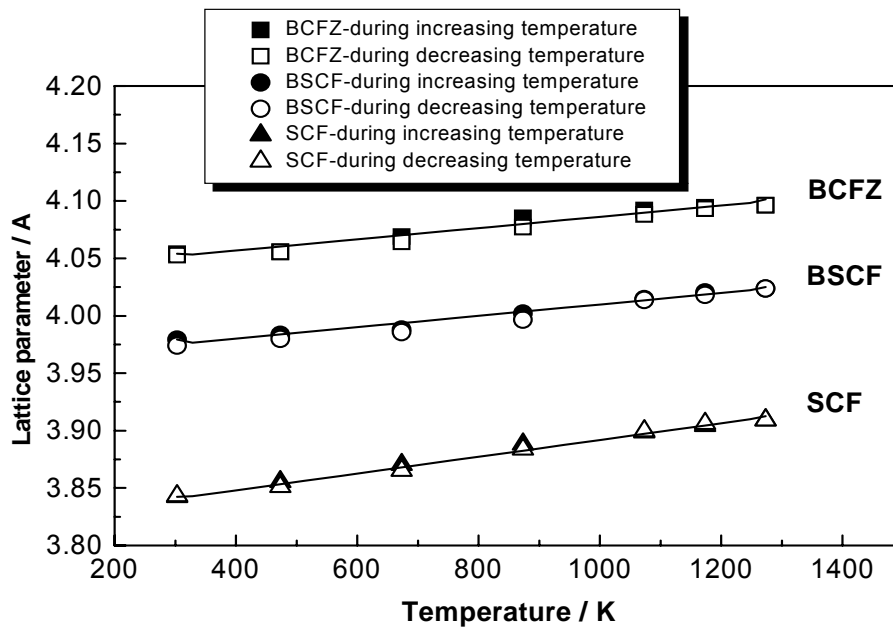


Figure 3.7 Temperature dependence of the lattice parameters for BCFZ, BSCF and SCF.

The highest TEC is found for SCF ($17.9 \times 10^{-6} \text{ K}^{-1}$), i.e. the material with the highest Co and the lowest Ba content. The high TEC of SCF was caused by the high concentration of

cobalt and iron which can easily change their valences in this composition. It can be assumed that the higher the TEC of the perovskite is, the more easily the B-site ions can change their valences. The relationship between reducibility and the TEC is also validated by comparing the BSCF and BCFZ materials. It is found that doping the B-site of perovskites with metal cations exhibiting a constant oxidation state, such as Zr^{4+} , can suppress oxygen nonstoichiometry variations and lattice expansion induced by changes in temperatures or oxygen chemical potentials and increase the phase structure stability [9]. It was found that the TEC of BCFZ ($10.3 \times 10^{-6} K^{-1}$) is slightly lower than that of BSCF ($11.5 \times 10^{-6} K^{-1}$). This finding is in agreement with the fact that the membrane reactor made of **BCFZ is more stable** during the POM reaction than that made of BSCF. Thus it can be understood that a high reducibility of metal ions in the perovskite leads to a high TEC which results in poor operation stability when it was used as membrane material for oxygen separation and membrane reactors for POM at high temperatures.

3.4 Oxygen permeation flux through $BaCo_xFe_yZr_zO_{3-\delta}$ (BCFZ) disc and hollow fiber membranes

For comparison, the disc-type membrane of the same perovskite composition was prepared and the oxygen permeation was tested under the same conditions. Table 3.1 shows the O_2 -permeation data for hollow fiber and disc geometries. In comparison to the disc-shaped membrane a lower F_{air} saturation flow rate is obtained for the hollow fiber perovskite membrane. Due to the different wall thickness, higher oxygen flux for the hollow fiber geometry in comparison to disc membrane is obtained.

Table 3.1 Comparison of the oxygen permeation data for different geometries of perovskite membranes: hollow fiber and disc membranes.

	Hollow fiber	Disc
F_{air} / mL/min	150 (shell side)	150
F_{He} / mL/min	30 (core side)	30
T / °C	850	850
Membrane surface / cm²	4.08	1.00
Membrane thickness / mm	0.16	1
J_{O₂} / mL/cm².min	1.05	0.30
J_{N₂}^{defect} / J_{O₂}	0.003	--

Fig. 3.8 shows the variation of the air flow rate between 20 mL/min and 150 mL/min at 850 °C, while the helium flow rate on the sweep side was kept at 30 mL/min. It was found that the oxygen permeation flux through hollow fiber increased with air flow rate until the air flow rate was higher than 80 mL/min. Further increase of the air flow rate did not lead to a further increase of the oxygen flux. These results indicate that air should be sufficiently delivered to use the separation capacity of the hollow fiber perovskite membrane properly. It can be concluded that for air flow rates higher than 80 mL/min a further increase of the air flow would not change the shell side concentration profile, being already flat at the level of the inlet concentration. In order to eliminate the effect of air

flow rate on the oxygen permeation flux, it was chosen a constant air flow rate of 150 mL/min in the subsequent studies.

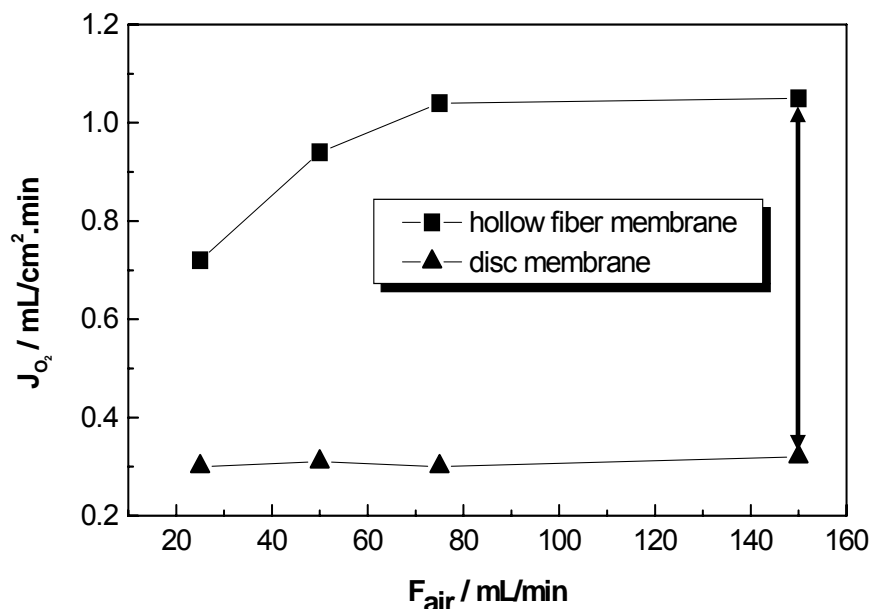


Figure 3.8 Oxygen permeation flux through the BCFZ perovskite membranes as a function of air flow rate. Permeation conditions: air flow rate on the shell side: 20 - 150 mL/min, helium flow rate on the sweep side: 30 mL/min, T = 850 °C.

In comparison to disc membrane much higher oxygen permeation flux through hollow fiber membrane are obtained because of the different wall thickness. It can be assumed that the limiting step is different for disc and hollow fiber membranes. The oxygen permeation flux through hollow fiber membrane is not as high as expected. From the thickness dependence between disc membrane (1 mm) and hollow fiber membrane (0.16 mm) it is expected to have a factor of 6.3 instead of 3.3. Another possible explanation would be that the oxygen concentration on the sweep side for hollow fiber membrane is much higher (11 %) than the disc membrane (1 %) when the helium flow rate on the sweep side is 30 mL/min and air flow rate on the shell side is 150 mL/min at the temperature of 850 °C. When the oxygen concentration on the sweep side is higher, the oxygen partial pressure is higher, the driving force is lower and oxygen permeation

through the membrane is lower. Thus the factor of 3.8 was obtained for oxygen permeation flux.

The dependence of the oxygen permeation flux of the disc and hollow fiber perovskite membrane on the He flow rates on the sweep side at 850 °C is shown in Fig. 3.9. During this experiment, the He flow rate was varied from 10 mL/min to 100 mL/min and the air flow rate was kept constant at 150 mL/min. As observed for the variation of the air flow rate, the oxygen permeation flux was found to increase with increasing helium flow rate. However, no saturation of the oxygen permeation flux was observed when the helium flow rate increased from 10 mL/min to 100 mL/min because the increase of the helium flow rate reduces the oxygen partial pressure (P_2 on the sweep side, and thus a higher oxygen permeation flux is obtained.

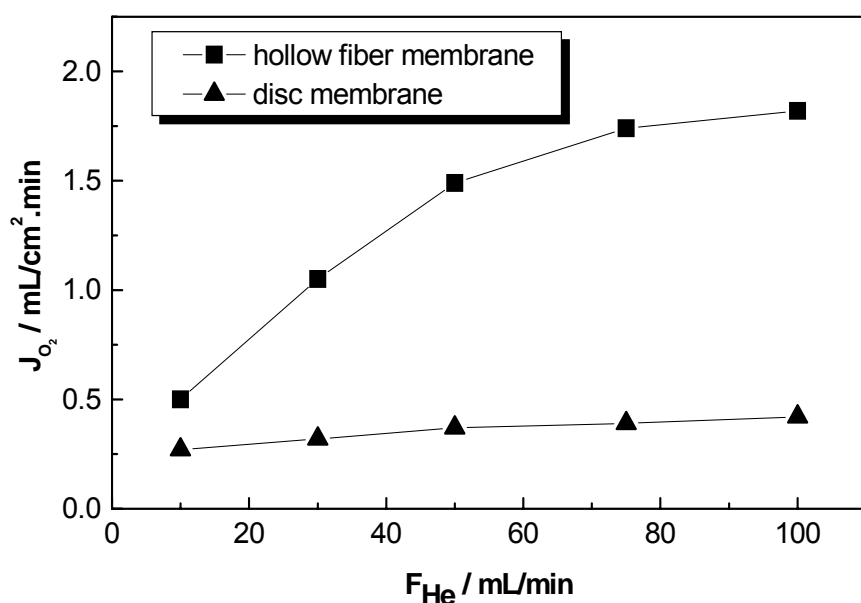


Figure 3.9 Oxygen permeation flux through the BCFZ perovskite membranes as a function of helium flow rate. Permeation conditions: air flow rate on the shell side: 150 mL/min, helium flow rate on the sweep side: 10 - 100 mL/min, $T = 850$ °C.

In comparison to hollow fiber membrane, the oxygen permeation flux through disc membrane is approximately constant and much lower than the hollow fiber. In conclusion

the oxygen permeation flux through disc membrane is not sensitive to the variation of the air flow rate on the shell side when the helium flow rate is constant or to the variation of the helium flow rate on the sweep side when the air flow rate is constant.

Fig. 3.10 shows oxygen permeation flux through disc and hollow fiber membranes at different temperatures. As shown in Fig. 3.10, the oxygen flux became substantial above a critical temperature of 650 °C. Higher oxygen permeation flux through hollow fiber membrane is obtained. Oxygen permeation flux through both membranes was found to increase with temperature. The tendency of increase in oxygen flux with temperature can be attributed to the promotion of the oxygen diffusion and the oxygen surface reaction rates. The increase of the oxygen flux through disc membrane is slow.

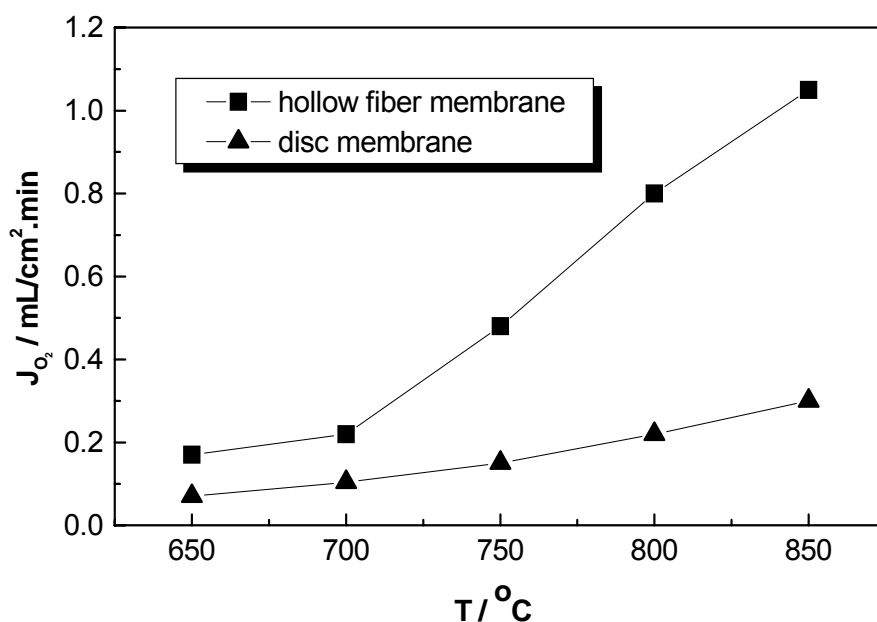


Figure 3.10 Temperature dependence of the oxygen permeation flux through BCFZ membranes. Conditions: air flow rate on the shell side: 150 mL/min; helium flow rate on the sweep side: 30 mL/min, T = 650 – 850 °C.

The XRD patterns of the hollow fiber membrane, disc membrane and powder are shown in Fig. 3.11. The hollow fiber membrane does not have a pure perovskite structure; a ZrO₂ by-phase can be observed. The by-phase is supposed to be formed during the preparation of the hollow fiber. In contrast, both the powder and disc membrane have a pure

perovskite structure. The structure for hollow fiber membrane is supported by the preparation method, the spinning additives which are not needed for pressing a disc membrane

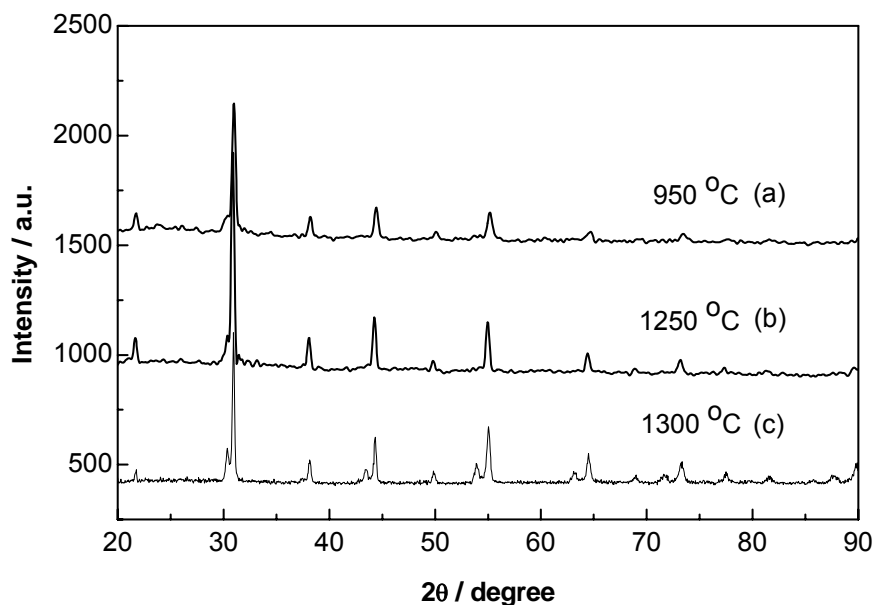


Figure 3.11 XRD patterns of BCFZ materials (a) powder; (b) disc membrane and (c) hollow fiber membrane at room temperature.

Phase stability is very important for an industrial perovskite application. XRD was used to characterize the perovskite structure of the hollow fiber membrane before and after operation. The XRD patterns of the perovskite membrane after sintering for 6 hours at 1300 °C in air and after oxygen permeation for 5 days at temperatures between 650 °C and 950 °C are shown in Fig. 3.12. In the fresh membrane, in addition to the cubic perovskite structure an unidentified by-phase was found. The concentration of this by-phase was unchanged after 5 days of operation. In contrast, the starting perovskite powder for spinning showed a pure perovskite structure. It is supposed, therefore, that this by-phase is formed during sintering. However, no difference between the fresh and spent membrane was observed. Thus, X-ray analysis of the material before and after the experiment confirmed that the material is phase stable.

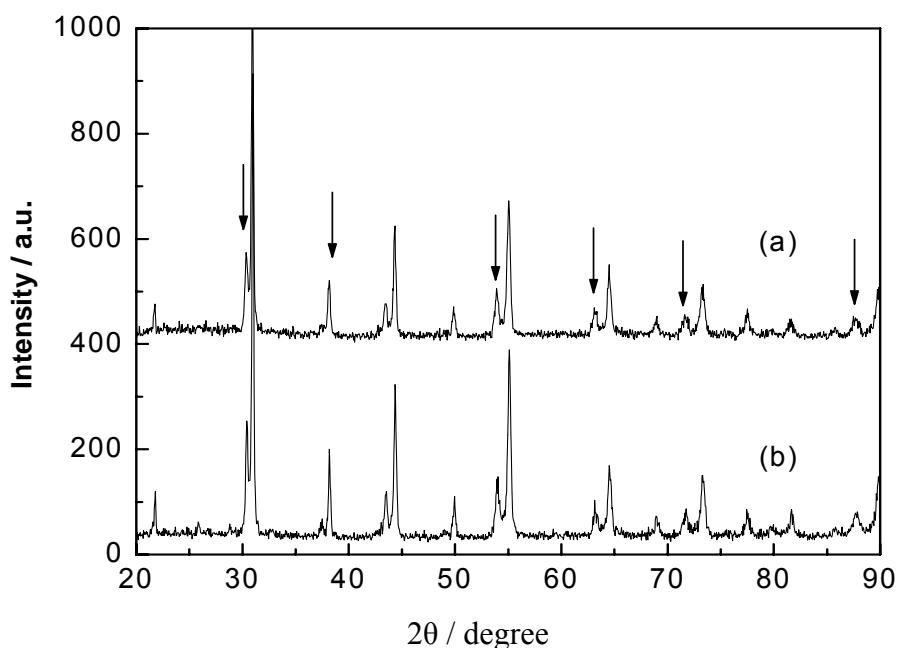


Figure 3.12 XRD patterns of the fresh and spent perovskite hollow fiber membranes. (a): fresh membrane; (b): membrane after oxygen permeation measurements for 5 days between 650 - 950 °C.

3.5 Oxygen permeation flux through hollow fiber membranes coated with Au paste

The temperature profile for the oven is shown in Fig. 3.13. For every oven temperature, there are only 8 cm isotherm zone. For example, when the oven temperature is 850 °C, there are only 8 cm zone really at 850 °C, the temperatures at the two endings are much lower than 850 °C. For all experiments the effective length of the hollow fiber used in the reactor was 24 cm. This means that only one third hollow fiber is at 850 °C and two third of hollow fiber is at the temperatures below 850 °C. As it is well known, the temperatures have great effect on the oxygen permeation flux. And the oxygen permeation fluxes as a lower limit in all experiments were calculated assuming that the total hollow fiber is at 850 °C.

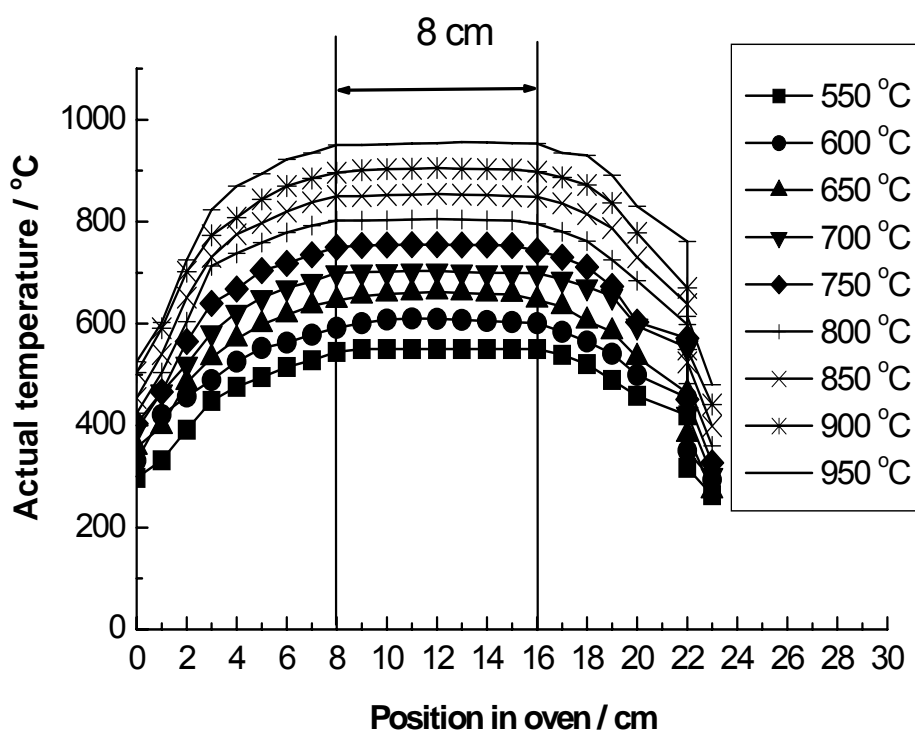


Figure 3.13 Temperature profile of the oven for oxygen permeation and POM reaction.

However, in Fig. 2.3b, the effective length of the hollow fiber is 2 cm. This remarkable experimental progress could be achieved by using Au paste to coat the ends of the hollow fiber membrane. After sintering at 950 °C a dense Au film was obtained. This means that the total hollow fiber is at 850 °C when the oven temperature is 850 °C. Therefore the temperature profile causes the difference of the oxygen permeation flux between the two types of hollow fiber membrane reactor. The high data from this section are correct.

The oxygen permeation through the gas tight hollow fiber membrane was measured in the high temperature permeation cell shown in Fig. 2.3b. Fig. 3.14 shows the influence of the air flow rate on the oxygen permeation flux through the hollow fiber membrane under different temperatures while the helium flow rate on the core side was kept constant at 30 mL/min. The oxygen permeation flux increased with raising air flow rate until the air flow rate was higher than 250 mL/min. Further increase of the air flow rate led to no further increase of the oxygen permeation flux, as shown in Fig. 3.14. The oxygen permeation flux through the hollow fiber membrane is determined by the gradient of the oxygen

concentrations across the membrane, i.e. the oxygen concentrations on the shell side and the core side.

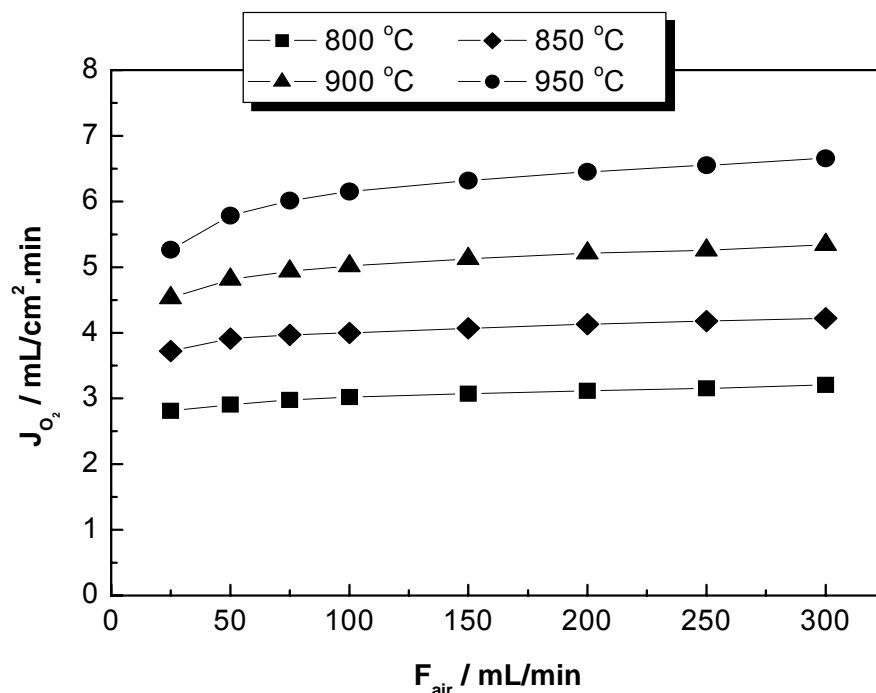


Figure 3.14 Oxygen permeation flux through short BCFZ hollow fiber as a function of air flow rates on the shell side. Membrane surface area: 0.43 cm^2 , He flow rate on the core side: 30 mL/min .

Fig. 3.15 shows the oxygen permeation flux as a function of the He flow rate on the core side. During this experiment the He flow rates were varied from 25 mL/min to 150 mL/min and the air flow rate was kept constant at 150 mL/min . A sharp increase of the oxygen permeation flux was observed when the He flow rate increased from 25 mL/min to 100 mL/min . However, the increase of the oxygen permeation flux becomes slow if the He flow rate on the core side is higher than 100 mL/min .

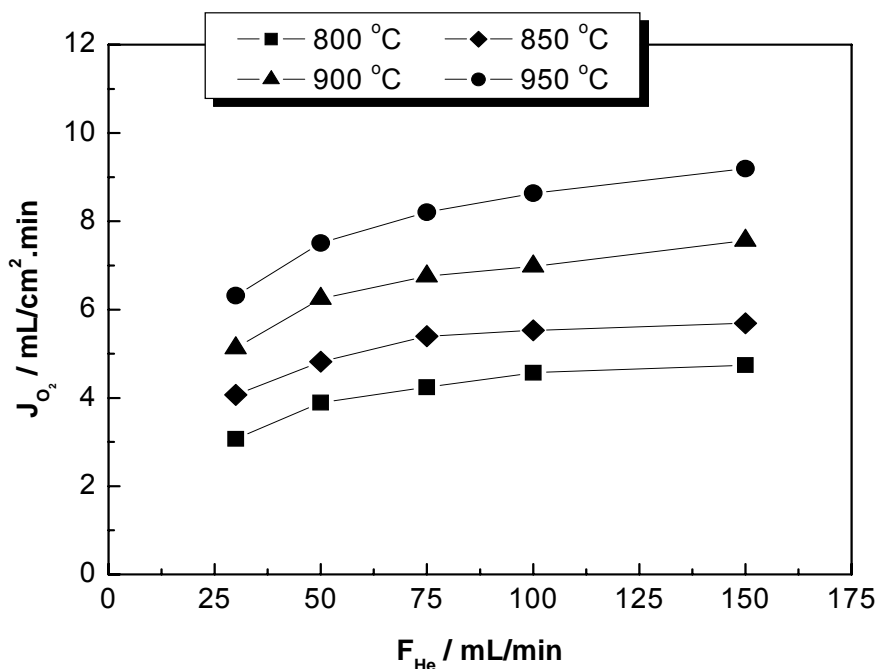


Figure 3.15 Oxygen permeation flux through BCFZ hollow fiber membrane as a function of He flow rates on the core side. Membrane surface area: 0.43 cm², air flow rate on the shell side: 150 mL/min.

Figure 3.16 shows the oxygen permeation through the short hollow fiber membrane as a function of temperature when air flow rate is 150 mL/min and He flow rate is 30 mL/min. For comparison the oxygen permeation through the hollow fiber was measured from 600 °C to 950 °C and then from 950 °C to 650 °C. The oxygen permeation flux through the hollow fiber was much higher when the measurements were performed from higher to lower temperature. It can be assumed that at 950 °C, the activation of the hollow fiber perovskite membrane has occurred. For both experiments the oxygen permeation flux is increasing with the temperature which is attributed to the promotion of the oxygen diffusion and the oxygen surface reaction rates. A low oxygen permeation flux is obtained when the temperature is below 700 °C for the experiment performed from 600 °C to 950 °C.

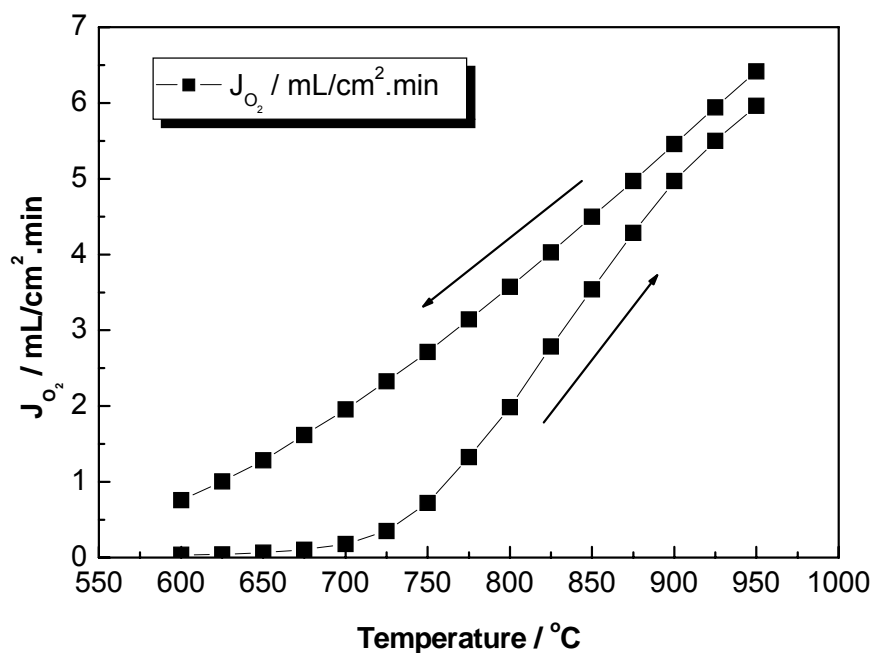


Figure 3.16 Oxygen permeation flux through BCFZ hollow fiber membrane as a function of temperature. Membrane surface area: 0.43 cm^2 , air flow rate on the shell side: 150 mL/min , He flow rate on the core side: 30 mL/min .

Another factor for evaluating the oxygen permeability is the activation energy for oxygen permeation. The activation energy for oxygen permeation of the short hollow fiber membrane is shown in Fig. 3.17. In the corresponding Arrhenius plot a straight line is found for short BCFZ hollow fiber membrane which gives an apparent activation energy of 53 kJ/mol . The apparent activation energy has a close value to the activation energy for disc membrane (56 kJ/mol) with the same composition and 1.0 mm thickness.

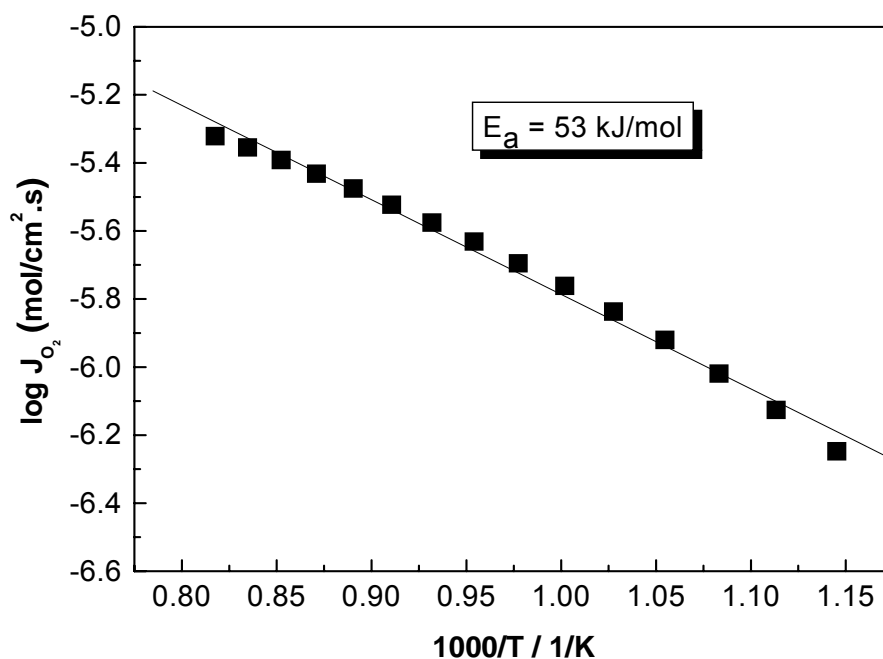


Figure 3.17 Arrhenius plot of the oxygen permeation flux of the dense hollow fiber perovskite membrane after activation at 950 °C. Permeation conditions: air flow rate on the shell side: 150 mL/min, helium flow rate on the core side: 30 mL/min, T = 600 – 950 °C.

The short hollow fiber membrane after operating for more than 100 h in the range of 600 °C to 950 °C with different air and helium flow rates was subjected to SEM-EDXS characterization and the SEM images are shown in Fig. 3.18. It is interesting to find that the membrane after oxygen permeation is becoming denser. A possible explanation for the closed pores can be the high temperature. Quantitative analysis of the SEM - EDXS element maps of the spent hollow fiber after 100 hours operation (Fig. 3.19) shows that no significant element segregation was observed on the both membrane surfaces and the bulk. This analysis of the hollow fiber membrane before and after the experiment confirmed that the perovskite hollow fiber membrane is stable.

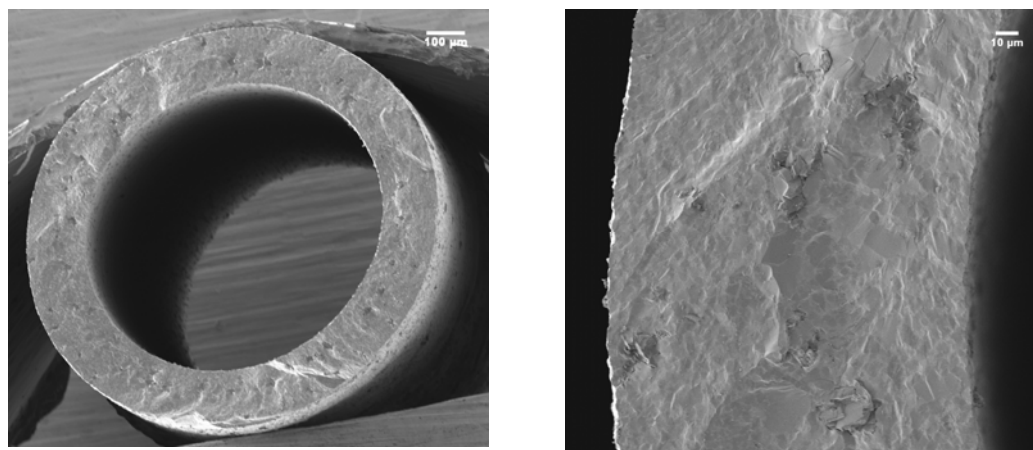


Figure 3.18 SEM pictures of the hollow fiber membrane after O₂-permeation.

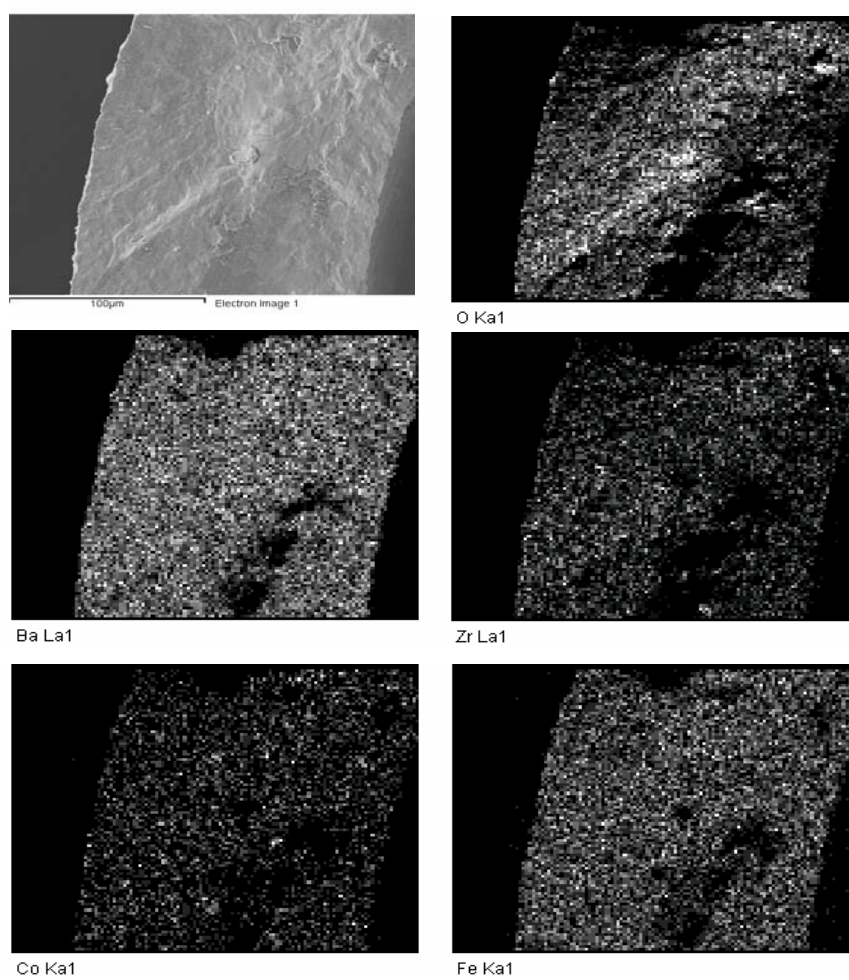


Figure 3.19 SEM - EDXS element maps for the spent fiber after 100 hours.

Quantitative measurements of the cations composition are shown in Table 3.2. Within the analytical precision, the compositions of the spent hollow fiber membrane surface exposed to helium, to air and the bulk are identical with the fresh membrane. This comparison between the fresh and spent hollow fiber membrane showed that the perovskite hollow fiber membrane is stable.

Table 3.2 Cation composition of the fresh and spent hollow fibers.

Sample	Ba (atom %)	Co (atom %)	Fe (atom %)	Zr (atom %)
Fresh membrane	54.2	18.4	17.6	9.8
Air side*	53.6	17.8	18.5	10.1
Bulk*	55.3	18.2	17.3	9.2
He side*	52.0	17.8	17.7	12.5

* the spent hollow fiber

3.6 Conclusions

Dense hollow fiber perovskite membranes of the composition $\text{BaCo}_x\text{Fe}_y\text{Zr}_z\text{O}_{3-\delta}$ were prepared by a phase inversion process. After sintering fibers with an outer diameter 800 - 900 μm , inner diameter 500 - 600 μm and a length of 30 cm were obtained. From an XRD phase study it was found that the dense hollow fiber membrane after sintering at 1300 °C was not a pure perovskite though the starting powder was a pure perovskite.

The O_2 -permeation rate was stable at 850 °C during 5 days which confirms the stable phase structure of the hollow fiber membranes. No signs of degradation of the perovskite material after O_2 -permeation measurements are observed from XRD. A high oxygen flux of 1.05 $\text{mL}/\text{cm}^2\cdot\text{min}$ was achieved for the long hollow fiber membrane at 850 °C when air flow rate on the shell side is 150 mL/min and helium flow rate on the core side is 30 mL/min .

A high oxygen permeation flux of 5.5 $\text{mL}/\text{cm}^2\cdot\text{min}$ through the short hollow fiber membrane was obtained under the air/He gradient ($P_1 = 0.21$ bar, $P_2 = 0.065$ bar) at 900

°C, which is the highest oxygen permeation flux through a short hollow fiber membrane reported in the open literatures so far. The high oxygen flux renders the hollow fiber geometry for MIEC membranes as possible candidates for industrial POM reactors.

3.7 Bibliography

- [1] P. N. Dyer, R. E. Richards, S. L. Russek, D. M. Taylor, *Solid State Ionics* 134 (2000) 21.
- [2] T. Schiestel, M. Kilgus, S. Peter, K. J. Caspary, H. Wang, J. Caro, *J. Membr. Sci.* 258 (2005) 1.
- [3] J. Caro, H. Wang, C. Tablet, A. Kleinert, A. Feldhoff, T. Schiestel, M. Kilgus, P. Kölsch, S. Peter, *Catal. Today*, accepted.
- [4] Y. Teraoka, H. M. Zhang, S. Furuka, N. Yamazoe, *Chem. Lett.* 167 (1985) 1743.
- [5] Z. P. Shao, W. S. Yang, Y. Cong, H. Dong, J. H. Tong, G. X. Xiong, *J Membr. Sci.* 172 (2000) 177.
- [6] J. H. Tong, W. S. Yang, R. Cai, B. C. Zhu, L. W. Lin, *Catal. Lett.* 78 (2002) 129.
- [7] S. Pei, M. S. Kleefish, T. P. Kobylinski, J. Faber, C. A. Udovich, Z. McCoy, B. Dabrowski, U. Balachandran, R. B. Poeppel, *Catal. Lett.* 30 (1995) 201.
- [8] H. Koster, F. H. B. Mertins, *Powder Diffraction* 18 (2003) 56.
- [9] V. V. Kharton, V. A. Sobyanin, V. D. Belyaev, G. L. Semin, S. A. Veniaminov, E. V. Tsipis, A. A. Yaremchenko, A. A. Valente, I. P. Marozau, J. R. Frade, J. Rocha, *Catal. Commun.* 5 (2004) 311.

4 Experimental and modeling study of dense perovskite hollow fiber membranes for the production of O₂-enriched air

The perovskite composition BaCo_xFe_yZr₂O_{3-δ} (BCFZ), which is a novel O₂-permeable membrane material with high O₂ permeation fluxes and excellent thermal and mechanical stability [1, 2], was applied in a modified composition in a hollow fiber configuration to prove the possibility of the production of O₂-enriched air in a perovskite membrane permeator [3]. A comprehensive analysis was conducted to investigate the effects of various factors on the performance of the permeator. The O₂-enriched air productivity of the BCFZ hollow fiber membrane was studied experimentally under different operating conditions. A model for the production of O₂-enriched air was developed by Dipl. Chem. C. Hamel [4] at the Max Planck Institute for Dynamics of Complex Technical Systems, University of Magdeburg and the data were compared to the experimentally results performed at the Institute of Physical Chemistry and Electrochemistry, University of Hanover. The structure and the stability of the BCFZ fiber in the O₂-enriched air production were investigated. This work intends to develop a more in-depth understanding of the O₂-enriched air process with BCFZ hollow fiber membranes in order to provide a guidance regarding the design of a hollow fiber membrane module for the oxygen enrichment under industrial conditions.

4.1 Model development for the production of O₂-enriched air

A gradient in the chemical potential of oxygen, forming the essential driving force for the mass transfer of oxygen in the considered material BCFZ, can be generated e.g. by:

1. Decreasing the oxygen partial pressure at one side of the hollow fiber by consumption of oxygen in a chemical reaction.

2. Decreasing the oxygen partial pressure at one side of the hollow fiber by application of non-reactive sweep gases.
3. Application of a significant difference in the total air pressure on both sides of the hollow fiber which provides different oxygen partial pressures.

For the mathematical quantification of the oxygen mass transfer from the shell to the core side through the hollow fiber (Fig. 4.1) a one dimensional, isothermal Plug Flow Tubular Reactor (PFTR) model was used. The derived model allows also the consideration and calculation of oxygen transport for using of reactive sweep gases and a coupling e.g. with selective oxidation reactions, respectively. Here, air is used as a non reactive sweep gas, i.e. the reaction rate, \bar{r} , is zero.

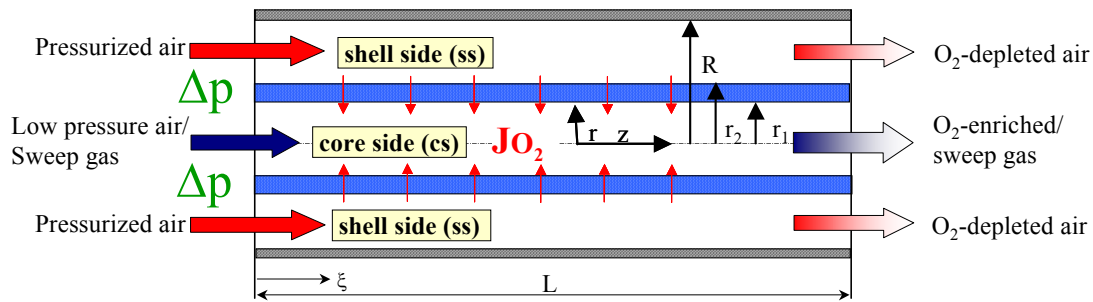


Figure 4.1 Schematic illustration of the simulated configuration.

Under the following assumptions, simplified mass balances can be formulated:

1. steady state conditions
2. isothermal
3. ideal gas behaviour
4. negligible axial and radial dispersion

Component and total mass balances on the shell side (ss) $r_2 < r < R$:

$$\frac{d\dot{n}_i^{ss}}{dz} = -2 \cdot \pi \cdot r_2 \cdot J_i \Big|_{r=r_2} \quad \text{with } i = 1, N \quad (4.1)$$

$$\frac{d\dot{n}_{tot}^{ss}}{dz} = -2 \cdot \pi \cdot r_2 \cdot \sum_i J_i \Big|_{r=r_2} \quad (4.2)$$

4 Production of O₂-enriched air

Oxygen flux through perovskite membranes [5, 6] $r_1 < r < r_2$:

$$J_{O_2} = \frac{D_{eff}}{4 \cdot n \cdot t} \cdot \left[(P_{O_2}^{ss})^n - (P_{O_2}^{cs})^n \right] \quad (4.3)$$

$$J_{O_2} = \frac{r_1}{r} \cdot J_{O_2} \Big|_{r=r_1} \quad (4.4)$$

J_i of all other components is zero.

Component and total mass balances on the core side (cs) $0 < r < r_1$:

$$\frac{d\dot{n}_i^{cs}}{dz} = \pi \cdot r_1^2 \cdot \rho_{Bulk} \cdot \sum_j v_{ij} \cdot \bar{r}_j + 2\pi \cdot r_1 \cdot J_i \Big|_{r=r_1} \quad (4.5)$$

or

$$\frac{d\dot{n}_i^{cs}}{dz} = \frac{m_{Kat}}{L} \cdot \sum_j v_{ij} \cdot \bar{r}_j + 2\pi \cdot r_1 \cdot J_i \Big|_{r=r_1} \quad (4.6)$$

$$p_{O_2}^{ss} = \frac{\dot{n}_{O_2}^{ss}}{\sum_i \dot{n}_i^{ss}} \cdot p_{tot}^{ss} = \frac{\dot{n}_{O_2}^{ss}}{\sum_i \dot{n}_{tot}^{ss}} \cdot p_{tot}^{ss} \quad (4.7)$$

with $i = 1, N$; $j = 1, M$.

The equations are coupled by the following boundary conditions:

$$r = r_1 \quad J_{O_2} = J_{O_2} \Big|_{r=r_1} \quad J_i = 0 \quad \text{for } i \neq O_2$$

$$p_{O_2}^{cs} = \frac{\dot{n}_{O_2}^{cs}}{\sum_i \dot{n}_i^{cs}} \cdot p_{tot}^{cs} = \frac{\dot{n}_{O_2}^{cs}}{\sum_i \dot{n}_{tot}^{cs}} \cdot p_{tot}^{cs} \quad (4.8)$$

$$r = r_2 \quad J_{O_2} = \frac{r_1}{r_2} \cdot J_{O_2} \Big|_{r=r_1} \quad J_i \neq J_{O_2} = 0$$

$$p_{O_2}^{ss} = \frac{\dot{n}_{O_2}^{ss}}{\sum_i \dot{n}_i^{ss}} \cdot p_{tot}^{ss} = \frac{\dot{n}_{O_2}^{ss}}{\sum_i \dot{n}_{tot}^{ss}} \cdot p_{tot}^{ss} \quad (4.9)$$

The \dot{n}_i and/or the J_i are specified for internal concentration profiles and finally the outlet concentration, calculated by numerical integration of the system of ordinary difference equations given by Eqs. 1-7 using standard techniques. This integration can be performed conveniently using MATLAB[®] [7].

4.2 Estimation of mass transfer parameters

In preliminary experiments the oxygen permeation of the hollow fiber perovskite membrane using He as the sweep gas was tested in a high-temperature gas permeation cell at (i) different O₂-partial pressures which were obtained by mixing different ratios of nitrogen and oxygen, (ii) different temperatures between 650 °C and 950 °C. Air or synthetic air of different ratios of nitrogen and oxygen were fed to the shell side and pure He (99.995 %) flowed on the core side of the membrane. The estimation and validation of mass transfer parameters for the characterization and the mathematical description of the hollow fiber properties are based on the performed experiments and the achieved data, respectively. The transport of oxygen ions in MIEC oxides is documented in manifold empirical as well as physically founded approaches [8]. One approach based on thermodynamical mechanisms is the theory of Wagner [5, 6] assuming the gradient of the chemical potential of oxygen as the driving force for mass transfer. Thus, the Wagner approach was used to describe the transfer of oxygen ions through the BCFZ perovskite hollow fiber under study. Assuming that the oxygen ionic conductivity is much lower than the electronic one, the oxygen permeation flux through the MIEC membrane can be well expressed by Eq. (4.3) with an Arrhenius approach describing the temperature dependence of D_{eff} according to Eq. (4.10):

$$D_{eff} = D_{\infty} \cdot e^{-\frac{E_A}{R \cdot T}} \quad (4.10)$$

Figure 4.2 shows the temperature influence and the dependency of the oxygen partial pressure on the oxygen permeation flux through the hollow fiber membrane using He as sweep gas. The comparison between the experimental data und the calculations using equations (4.10) and (4.11) and the experimentally derived mass transfer parameters: $n = 0.39$, $D_{eff} = 1.647 \cdot 10^{-3} \text{ m}^2/\text{h} \cdot \text{bar}^n$, $D_{\infty} = 327.4 \text{ m}^2/\text{h} \cdot \text{bar}^n$, $E_A = 113.9 \text{ kJ/mol}$ reveals a sufficient agreement [9, 10] and forms the basis for further simulation studies.

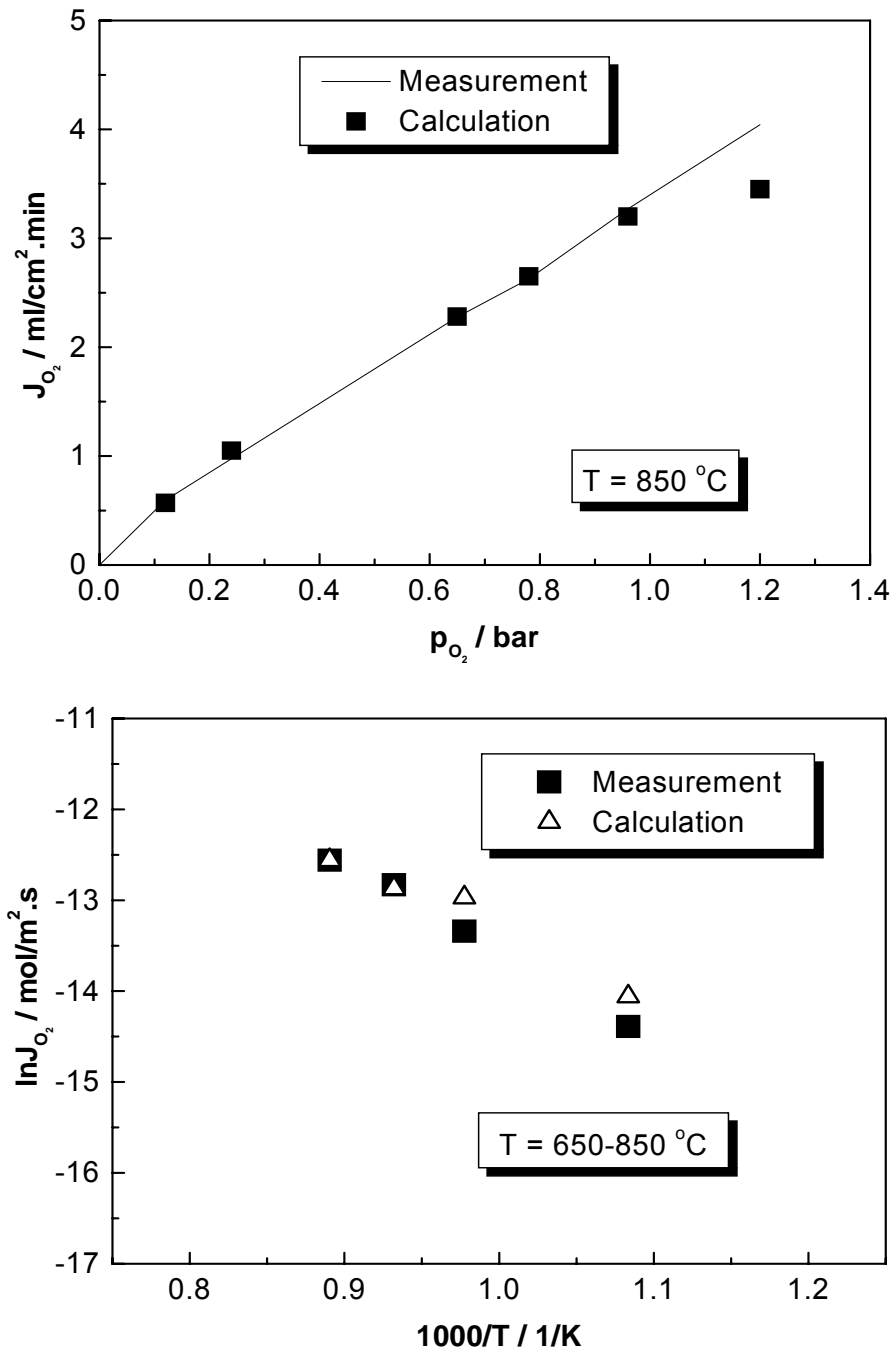


Figure 4.2 Comparison of the experimental and simulated data using He as the sweep gas. Air flow rate on the shell side: 150 mL/min, He flow rate on the core side: 30 mL/min, membrane surface area: 3.50 cm².

The parameters of the BCFZ hollow fiber membrane for O₂-enriched air production and the operating condition, listed in Table 4.1, were employed in the simulation and experiments.

Table 4.1 Parameters used in the simulation and experiments of the O₂-enriched air production using the BCFZ perovskite hollow fiber membrane.

Membrane area / cm ²	$S = 3.5$
Outer radius / mm	$r_2 = 0.42$
Inner radius / mm	$r_1 = 0.26$
Thickness / mm	$t = 0.16$
Effective membrane length / mm	$L = 160$
Operation temperature / °C	$T = 650 - 950$
Air flow rate on the shell side / mL/min	10 - 150
Air flow rate on the core side / mL/min	100
Air pressure difference / bar	$\Delta P = 0.5 - 10$
Air pressure on the core side / bar	$P_{tot}^{cs} = 1$
Effective diffusion coefficient / m ² /h.bar ⁿ	$D_{eff} = 1.647 \cdot 10^{-3}$
Preexponential factor / m ² /h.bar ⁿ	$D_{\infty} = 327.4$
Exponent in Eq. (4.3)	$n = 0.39$
Activation energy in Eq. (4.10) / kJ/mol	$E_A = 113.9$

4.3 O₂-enriched air production results

The performance of perovskite membranes for the O₂-enrichment can be characterized by the oxygen permeation rate (J_{O_2}), the production rate of O₂-enriched air (R_{OEA}) and the oxygen concentration at the outlet on the core side ($C_{O_2, outlet}$). As mentioned above, the driving force for oxygen transport through perovskite membranes is the gradient of the chemical potential, i.e. the difference of the oxygen partial pressure across perovskite membranes. Instead of the already known oxygen separation by inert sweep gases, it is

also possible to get O₂-enriched air by using air as sweep gas applying an air pressure difference as a driving force. Fig. 4.3 shows experimental and modeling results under variable air pressure differences. Both the experimental and modeling results show the same trend, i.e., the oxygen permeation flux increases with enhancing the air pressure difference, thus promoting an increased driving force for oxygen permeation. Experimentally, when the air pressure difference increases from 0.5 bar to 3.0 bar, the O₂ concentration on the permeate side almost doubles from 30 % to 55 % and the O₂ permeation rates rise from 0.5 mL/cm².min to 2.2 mL/cm².min.

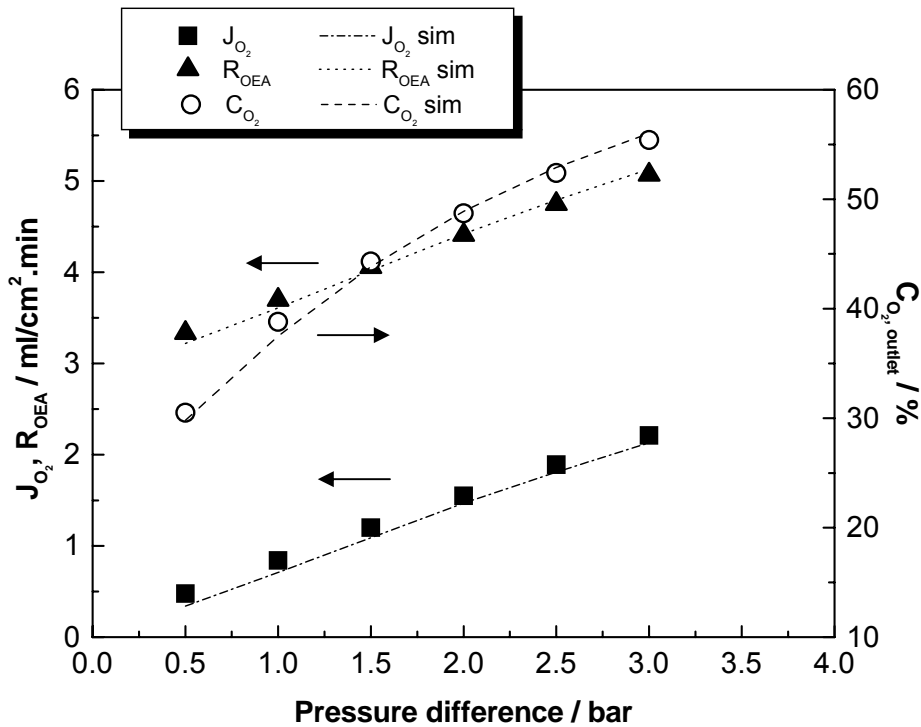


Figure 4.3 O₂ permeation rate, O₂-enriched air production rate and O₂ concentration versus the pressure difference between the two sides of a BCFZ membrane at 950 °C. Air flow rate: feed side = 100 mL/min; permeate side = 10 mL/min, membrane surface area = 3.50 cm².

Accordingly, the production rate of O₂-enriched air increases from 3.3 mL/cm².min to 5.0 mL/cm².min. The developed simple reduced 1D-model and the derived mass transfer

parameters for the hollow fiber agree very well with the experimental data set for the investigated parameter range of the given pressure difference. It should be pointed out that silicone rubber as the most often commercially used polymeric membrane with 25 μm thickness shows an O₂ permeation flux of $\sim 0.11 \text{ mL/cm}^2 \cdot \text{min} \cdot \text{bar}$ with an O₂ concentration of 35 % under the pressure difference of 9.0 bar [11]. However, the perovskite hollow fiber membrane with the thickness of around 180 μm can give an O₂ concentration higher than 38 % with a production rate of $3.7 \text{ mL/cm}^2 \cdot \text{min}$ applying only a pressure difference of 1.0 bar.

In Fig. 4.4 the axial oxygen concentration profiles for the O₂-enriched air on the core side are illustrated as a function of the hollow fiber length for three selected pressure differences. As an example it demonstrates the approach of modeling. The tubular permeation set-up constitutes an open system of multiple molar fluxes (shell and core side) coupled over the oxygen flux through the membrane. Thus, the oxygen flux, J_{O_2} , depends on the oxygen concentration and/or oxygen partial pressures on the sweep and shell sides, and this on each axial position. Based on the boundary conditions the oxygen flux, J_{O_2} , and the next corresponding oxygen concentrations are calculated, which result in the new oxygen flux. Thus, the given axial profiles were obtained. The estimated outlet concentrations as integral values correspond with the experimental data given in Fig. 4.3.

As shown in Figure 4.4, an increasing pressure on the shell side (pressurized air) results in a higher driving force for the mass transfer and in an increasing slope of the axial concentration profile of oxygen. After half length of the hollow fiber the change or the increase of the concentration of oxygen is negligible. Thus, for the given pressure differences, the membrane can be shortened to achieve the same outlet concentrations. On the other hand, the length of 16 cm is also suitable to work at higher pressure differences to increase the oxygen concentration on the permeate side (core side). The latter aspect is investigated in more detail in chapter “Evaluation of permeation performance in a broader range of operation parameters”.

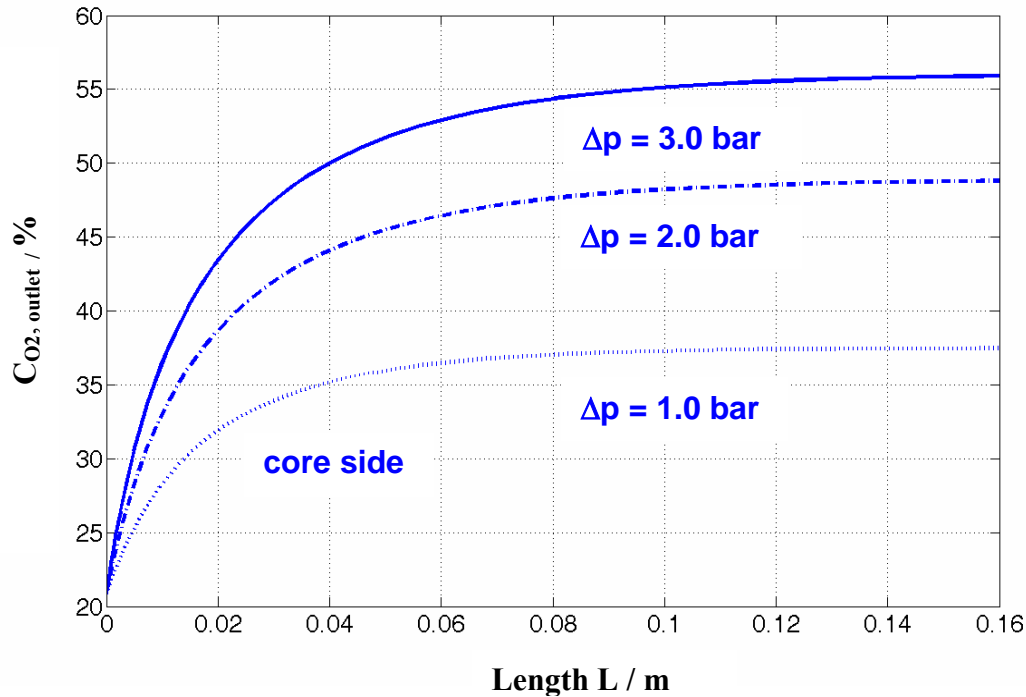


Figure 4.4 Axial profiles of the calculated O₂ concentration versus hollow fiber length for three selected pressure differences at 950 °C. The following conditions were assumed: air flow rate: feed side = 100 mL/min; permeate side = 10 mL/min, membrane surface area = 3.50 cm² [4].

Fig. 4.5 shows the experimental and simulated oxygen permeation rate, O₂-enriched air production rate and oxygen concentration versus temperature under a fixed pressure difference of 1.5 bar. As expected, the oxygen permeation rate increases with increasing temperature, which lead to the increase of the production rate of O₂-enriched air and oxygen concentration on the permeate side. In the temperature range studied, the oxygen concentration always maintains at a relative high level (> 30 %). The simulated results predict the same trend as the experiments, though the discrepancy between the simulated and experimental results is slightly higher at low temperatures. This discrepancy, also obtained in Fig. 4.2, may be attributed to the assumption that oxygen permeation flux is only determined by the diffusion in the membrane bulk. In fact, the surface exchange of oxygen on the membrane surface may play an important role on the oxygen permeation at

lower temperatures. Nevertheless, the simulated results are in good accordance with the experimental results.

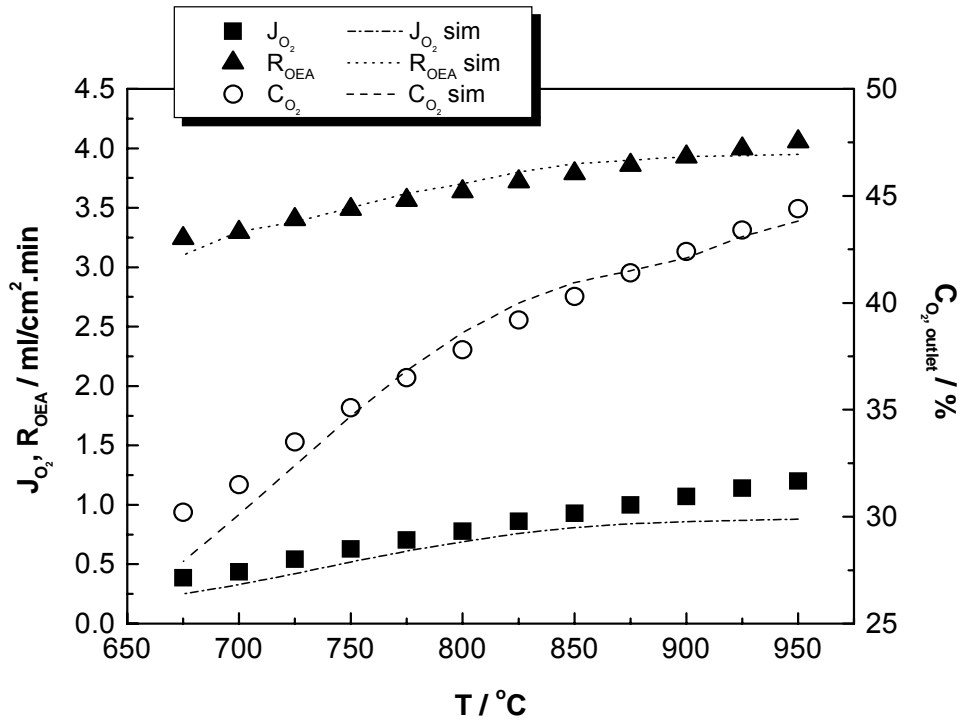


Figure 4.5 O₂ permeation rate, O₂-enriched air production rate and O₂ concentration versus temperatures under a fixed pressure difference of 1.5 bar. Air flow rate: feed side = 100 mL/min; permeate side = 10 mL/min, membrane surface area = 3.50 cm².

Fig. 4.6 shows the O₂ permeation rate, O₂-enriched air production rate and O₂ concentration as a function of air flow rate on the permeate side under an air pressure difference of 1.5 bar at 875 °C. It was previously found that the O₂ permeation rate increases with increasing flow rate of He used on the permeate side as a sweep gas [12]. The reason is that the oxygen partial pressure (or oxygen concentration) on the permeate side decreases with increasing the He flow rate. As shown in Fig. 4.6, the oxygen concentration decreases significantly with increasing the air flow rate on permeate side. This leads to an increase of the O₂ permeation rate with increasing the air flow rate on the permeate side. Accordingly, the O₂-enriched air production rate increases. From the

simulated result it can be seen that when the air flow rate is ~25 mL/min on the permeate side there is a good compromise where the oxygen concentration reaches ~35% with the O₂-enriched air production rate of ~9.0 mL/cm².min. From Fig. 4.6, it was also found that various oxygen concentrations required for the different industry processes can be obtained by adjusting the air flow rate on the permeate side. The experimental data could be sufficiently described also for various air flow rates.

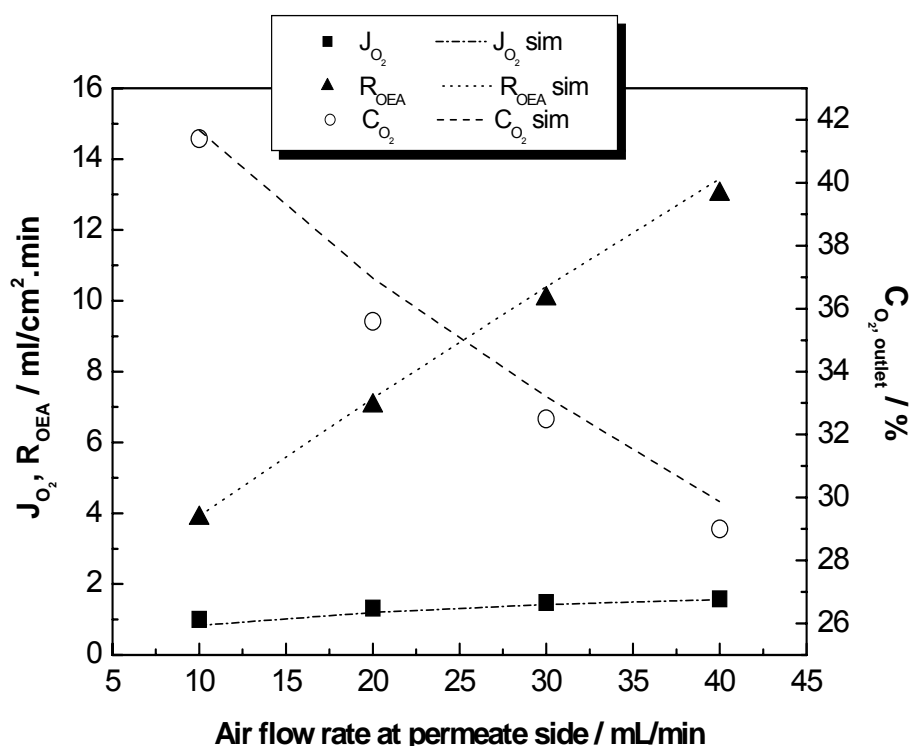


Figure 4.6 O₂ permeation rate, O₂-enriched air production rate and O₂ concentration versus air flow rate on the permeate side under a fixed pressure difference of 1.5 bar at 875 °C. Air flow rate: feed side = 100 mL/min, membrane surface area = 3.50 cm².

4.4 Stability

20 years after the pioneering paper of Teraoka et al. [13] who first reported the oxygen permeation through a perovskite membrane based on $\text{La}_{1-x}\text{A}_x\text{Co}_{1-y}\text{Fe}_y\text{O}_{3-\delta}$, still no industrial applications exist although the perovskite membranes are promising to apply in the field of chemical processing, including partial oxidation of natural gas to syngas [14-17], oxidative coupling of methane to value-added products such as ethane/ethylene [18-21], selective oxidation of hydrocarbons [22-24] and power generation [25, 26]. This lack of applicability is mainly due to the long-time stability problems of perovskites, especially at low oxygen partial pressure such as under the syngas atmospheres [27-29]. A further problem is the poor operational safety of such systems. E.g. in POM reaction, in case of a membrane leak air and methane/syngas mix at 800 °C which obviously causes serious trouble if not handled properly. However, these stability and operational safety problems are not relevant in the proposed O₂-enrichment process because both sides of the perovskite membranes are exposed to an oxidizing atmosphere (air). As expected, the perovskite membranes exhibit an excellent stability as shown in Fig. 4.7. The perovskite membrane was operated steadily for more than 800 hours at 875 °C under a constant pressure difference of 1.5 bar. During the long-time operation, the O₂ concentration in the O₂-enriched air reaches around 42 % with an O₂ permeation rate of $\sim 1.0 \text{ mL/cm}^2\cdot\text{min}$ and an O₂-enriched air production rate of $\sim 4.0 \text{ mL/cm}^2\cdot\text{min}$. It should be pointed out that we voluntarily stopped the long-term testing although the perovskite membrane was still working after 800 hours.

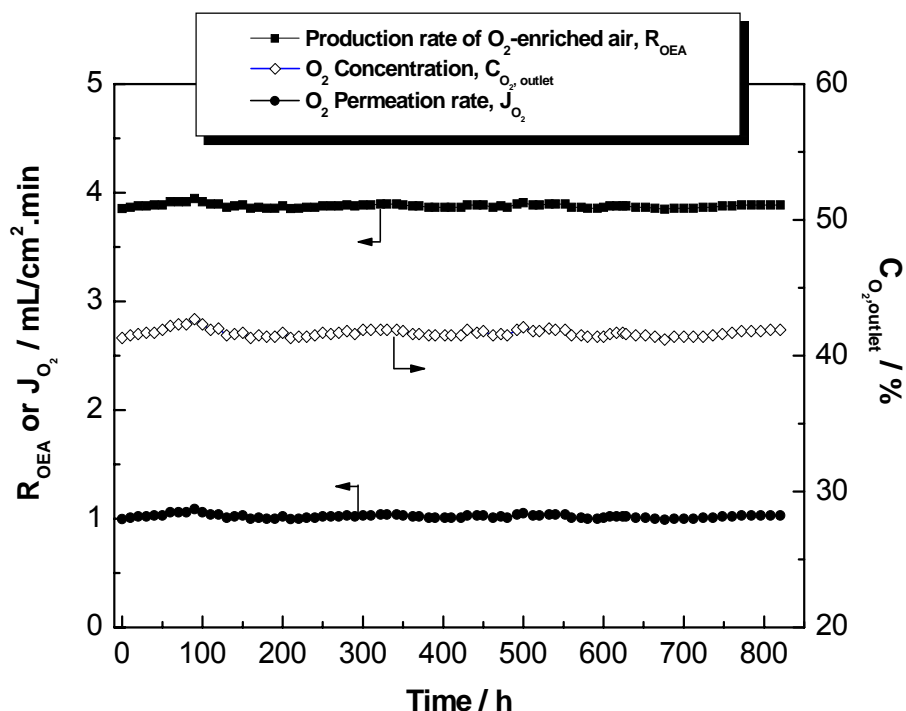


Figure 4.7 Long-time stability of perovskite hollow fiber for the production of O₂-enriched air. Air flow rate: feed side = 100 mL/min; permeate side = 10 mL/min, membrane surface area = 3.50 cm², pressure difference = 1.5 bar, T = 875 °C.

XRD was used to characterize the perovskite structure of the hollow fiber membrane before and after 800 hours operation, as shown in Fig. 4.8. No difference between the fresh and spent membrane and no carbonate were observed. This means that the structure is stable during the long time operation. Quantitative analysis of the SEM - EDXS element maps of the spent hollow fiber after 800 hours operation (Fig. 4.9) shows that no significant element segregation was observed on the both membrane surfaces and the bulk. This analysis of the hollow fiber membrane before and after the experiment confirmed that the perovskite hollow fiber membrane is stable.

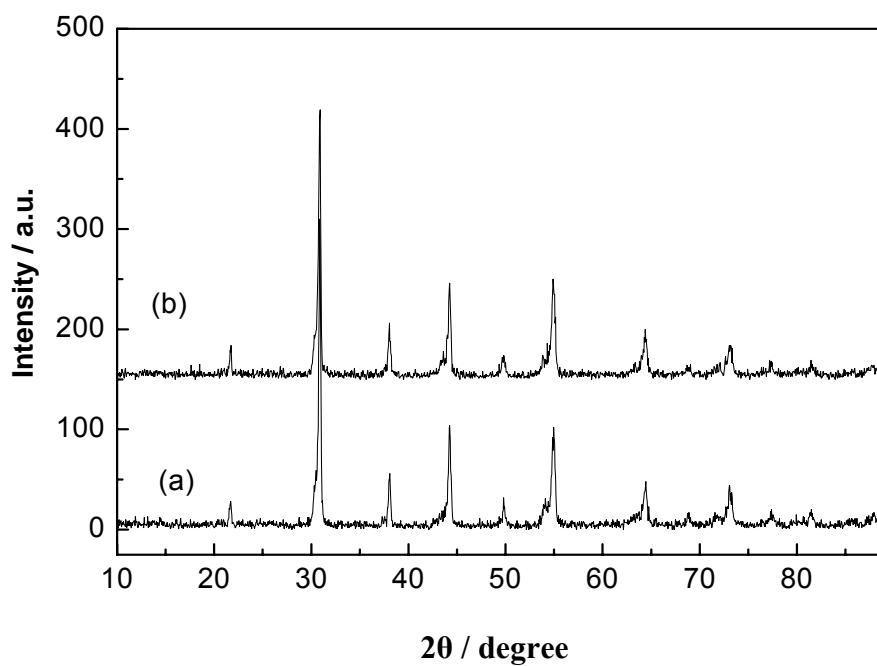


Figure 4.8 XRD patterns of the fresh and spent perovskite hollow fiber membranes. (a): fresh membrane; (b): spent membrane after 800 hours.

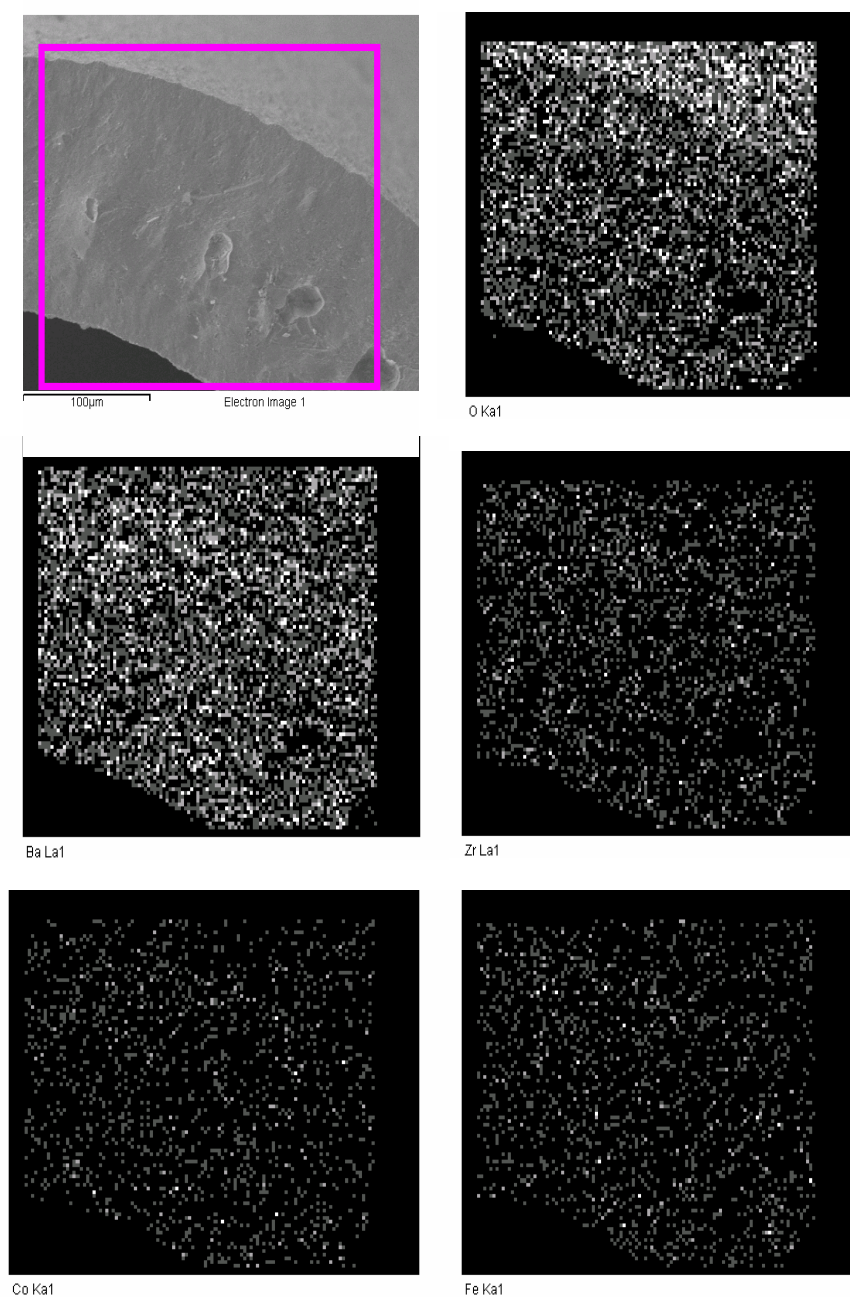


Figure 4.9 SEM-EDXS element maps for the spent fiber after 800 hours.

4.5 Conclusions

Gastight BCFZ hollow fiber membranes have been prepared at the IGB in Stuttgart by phase inversion spinning followed by sintering. The prepared BCFZ hollow fiber membranes were employed for high temperature O₂-enrichment. The O₂ concentration reached in the experiments was approximately 36 %. The O₂-enriched air production rate was 8.0 mL/min.cm² at 875 °C using a moderate total pressure difference of 1.5 bar. Higher O₂ concentrations in the O₂-enriched air and production rates required for different industrial processes appear to be achievable by controlling the operational parameters such as temperature, total pressure difference and gas flow rates. A mathematical model was developed by C. Hamel at the University of Magdeburg to simulate the oxygen enrichment achievable using hollow fiber membranes. The modelling results are in good agreement with experimental data. Based on the validated model of the air separation process, the mass transfer properties of the membrane were calculated in a broad parameter range. The highest achievable amount of oxygen enrichment of ca. 68 % was estimated for a temperature of 950 °C, a pressure difference of 10 bar and a flow rate of 10 mL/min and 150 mL/min on the permeate and retentat sides, respectively. The BCFZ perovskite hollow fiber membrane was steadily operated for more than 800 h for oxygen enrichment without any fracture. XRD and SEM-EDXS element maps of the spent hollow fiber membrane show that no structure change and no significant element segregation were observed. The long-time stability found in our experiments indicates that the perovskite membrane of the type investigated has the potential to replace the current O₂-enrichment system for high temperature applications.

4.6 Notation

$C_{O_2,outlet}$	oxygen concentration at the outlet on the core side, %
$C_{O_2,inlet}$	fed oxygen concentration in air, %
D_{eff}	effective diffusion coefficient, m ² /h.bar ⁿ

4 Production of O₂-enriched air

D_{∞}	preexponential factor, m ² /h.bar ⁿ
E_A	activation energy, kJ/mol
$F_{air, inlet}$	fed air flow rate on the shell side, mL/min
F_{outlet}	O ₂ -enriched air flow rate of the outlet on the shell side, mL/min
i	component index
j	reaction index
J_{O_2}	oxygen permeation flux, mL/cm ² .min
J_i	flux of component i through hollow fiber, mol/m ² .s
L	effective membrane length, m
m_{cat}	mass catalyst, kg
M	number of reactions
n_i^{ss}	molar flow rate of component i on the shell side, mol/s
n_{tot}^{ss}	total molar flow rate of component i on the shell side, mol/s
n_i^{cs}	molar flow rate of component i on the core side, mol/s
n_{tot}^{cs}	total molar flow rate of component i on the core side, mol/s
N	number of components
$P_{O_2}^{cs}$	oxygen partial pressure on the core side, bar
P_{tot}^{cs}	total pressure on the core side, bar
$P_{O_2}^{ss}$	oxygen partial pressure on the shell side, bar
P_{tot}^{ss}	total pressure on the shell side, bar
r	radial coordinate, m
r_1	inner radius of the hollow fiber membrane, mm
r_2	outer radius of the hollow fiber membrane, mm
\bar{r}	reaction rate, mol/kg.s
R	radius of the ceramic tube as the shell, cm
R_{OEA}	O ₂ -enriched air production rate, mL/ cm ² .min
S	effective membrane surface area, cm ²

t	the thickness of the hollow fiber, mm
ρ_{Bulk}	density of catalyst bed, kg/m ³
z	axial coordinate, m

4.7 Bibliography

- [1] J. H. Tong, W. S. Yang, B. C. Zhu, R. Cai, *J. Membr. Sci.* 203 (2002) 175.
- [2] J. H. Tong, W. S. Yang, R. Cai, B. C. Zhu, L. W. Lin, *Catal. Lett.* 78 (2002) 129.
- [3] H. H. Wang, S. Werth, T. Schiestel, J. Caro, *Angew. Chem. Int. Ed.* 44 (2005) 6906.
- [4] C. Hamel, A. S. Morgenstern, T. Schiestel, S. Werth, C. Tablet, J. Caro, H. Wang, *AIChE J.*, accepted.
- [5] H. J. M. Bouwmeester, *Catal. Today* 82 (2003) 141.
- [6] H. J. M. Bouwmeester, H. Kruidhof, A. J. Burggraaf, *Solid State Ionics* 72 (1994) 185.
- [7] D. Redfern, C. Campbell, *The Matlab 5 Handbook*, Springer, 1997.
- [8] P. J. Gellings, H. J. M. Bouwmeester, *The CRC Handbook of Solid State Elektrochemistry*, CRC Press 1997.
- [9] T. Schiestel, M. Kilgus, S. Peter, K. J. Caspary, H. Wang, J. Caro, *J. Membr. Sci.* 258 (2005) 1.
- [10] C. Tablet, G. Grubert, H. H. Wang, T. Schiestel, M. Schroeder, B. Langanke, J. Caro, *Catal. Today* 104 (2005) 126.
- [11] S. L. Matson, W. J. Ward, S. G. Kimura, W. R. Browall, *J. Membr. Sci.* 29 (1986) 79.
- [12] H. H. Wang, R. Wang, D. T. Liang, W. S. Yang, *J. Membr. Sci.* 243 (2004) 405.
- [13] Y. Teraoka, H. M. Zhang, S. Furukawa, N. Yamazoe, *Chem. Lett.* 11 (1985) 1743.
- [14] C. Y. Tsai, A. G. Dixon, W. R. Moser, Y. H. Ma, *AIChE J.* 43 (1997) 2741.
- [15] U. Balachandran, J. T. Dusek, P. S. Maiya, B. Ma, R. L. Mieville, M. S. Kleefisch, C. A. Udovich, *Catal. Today* 36 (1997) 265.
- [16] X. H. Gu, W. Q. Jin, C. L. Chen, N. P. Xu, J. Shi, Y. H. Ma, *AIChE J.* 48 (2002)

2051.

- [17] T. Ishihara, Y. Tsuruta, T. Todaka, H. Nishiguchi, Y. Takita, *Solid State Ionics*, 152 (2002) 709.
- [18] S. J. Xu, W. J. Thomson, *AIChE J.* 43 (1997) 2731.
- [19] J. E. Elshof, H. J. M. Bouwmeester, H. Verweij, *Appl. Catal. Gen. A* 130 (1995) 195.
- [20] V. V. Kharton, V. A. Sobyanin, V. D. Belyaev, G. L. Semin, S. A. Veniaminov, E. V. Tsipis, A. A. Yaremchenko, A. A. Valente, I. P. Marozau, J. R. Frade, J. Rocha, *Catal. Commun.* 5 (2004) 311.
- [21] F. T. Akin, Y. S. Lin, *AIChE. J.* 48 (2002) 2298.
- [22] H. H. Wang, Y. Cong, W. S. Yang, *Chem. Commun.* 14 (2002) 1468.
- [23] M. Rebeilleau-Dassonneville, S. Rosini, A. C. van Veen, D. Farrusseng, C. Mirodatos, *Catal. Today* 104 (2005) 131.
- [24] F. T. Akin, Y. S. Lin, *J. Membr. Sci.* 209 (2002) 457.
- [25] J. Y. Ren, Y. Q. Fan, F. N. Egolfopoulos, T. T. Tsotsis, *Chem. Eng. Sci.* 58 (2003) 1043.
- [26] Y. Q. Fan, J. Y. Ren, W. Onstot, J. Pasale, T. T. Tsotsis, F. N. Egolfopoulos, *Ind. Eng. Chem. Res.* 42 (2003) 2618.
- [27] S. G. Li, W. Q. Jin, N. P. Xu, J. Shi, *J. Membr. Sci.* 186 (2001) 195.
- [28] M. Schroeder, *Phys. Chem. Chem. Phys.* 7 (2005) 166.
- [29] C. S. Chen, S. J. Feng, S. Ran, D. C. Zhu, W. Liu, H. J. M. Bouwmeester, *Angew. Chem. Int. Ed.* 42 (2003) 5196.

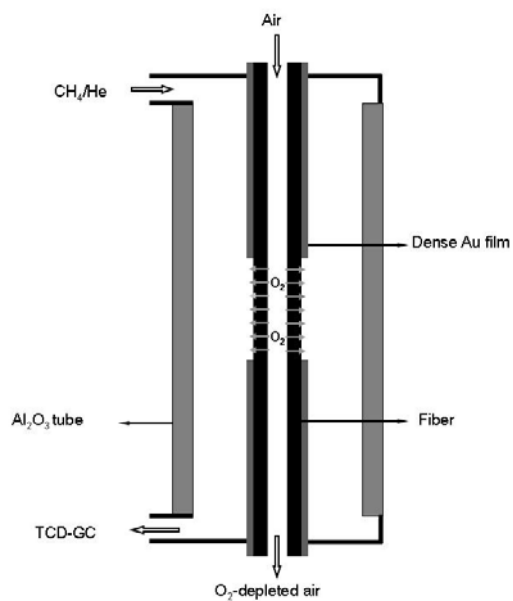
5 POM in a perovskite hollow fiber membrane reactor

The perovskite mixed conducting membrane made from the composition $\text{BaCo}_x\text{Fe}_y\text{Zr}_z\text{O}_{3-\delta}$ (BCFZ) in a hollow fiber geometry was used to construct a membrane reactor for the POM to syngas ($\text{CO} + \text{H}_2$) and possible reaction pathways in the hollow fiber membrane reactor were deduced. In the membrane reactor without catalyst filling, the product gas contained mainly unreacted CH_4 and O_2 together with a few percent of CO_2 . After packing sufficient Ni-based catalyst around and behind the hollow fiber membrane, almost exclusively syngas ($\text{CO} + \text{H}_2$) was observed as product.

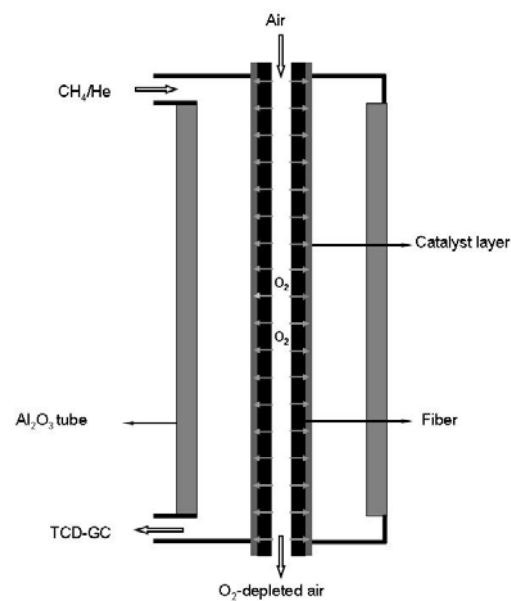
Fig. 5.1 shows a schematic diagram of the membrane reactor used in this study. The two ends of the hollow fiber were coated by Au paste, and after sintering at $950\text{ }^\circ\text{C}$ a dense Au film was obtained. Therefore, such Au-coated hollow fibers can be sealed at room temperature and the uncoated part can be kept in the middle of the oven ensuring isothermal conditions. As standard condition, 150 mL/min air was fed to the core side and a mixture of CH_4 and He was fed to the shell side of the fiber. Different catalyst arrangements were studied (Fig. 5.1). In the configuration A, no catalyst was used. In the configuration B, a commercial Ni-based steam reforming (SR) catalyst* (Süd-Chemie) was coated on the outer surface of the hollow fiber perovskite membrane, in the configuration C the catalyst was packed only around the hollow fiber membrane and in the configuration D, the Ni-based SR catalyst was packed around and behind the hollow fiber membrane.

* Because of several pending WO Patents the composition of the SR catalyst can not be given.

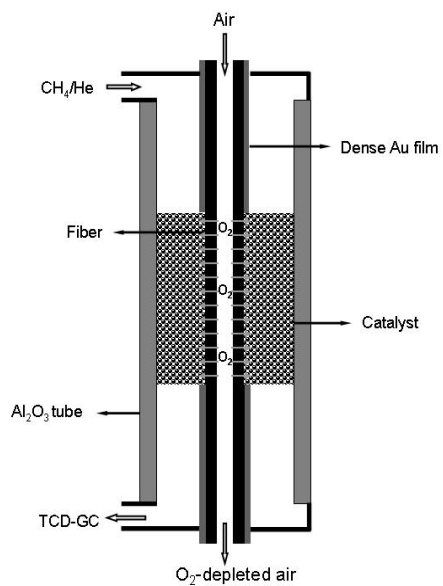
Configuration A



Configuration B



Configuration C



Configuration D

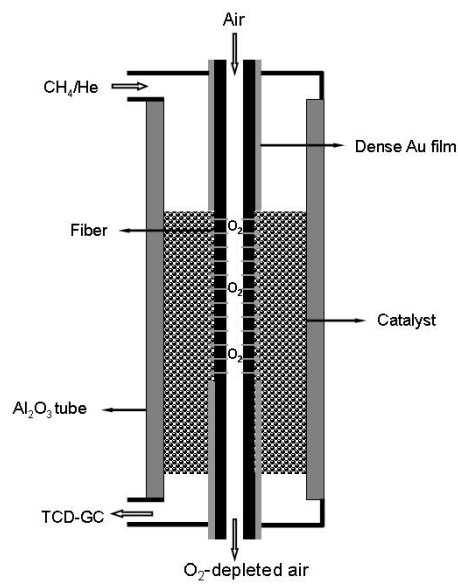


Figure 5.1 Schematic diagram of different types of catalyst arrangements in BCFZ hollow fiber membrane reactors for POM.

5.1 POM reaction in a hollow fiber membrane reactor without catalyst

The BCFZ hollow fiber membrane was adopted for the construction of a membrane reactor for studying the POM reaction, since it had the highest so far known steady-state oxygen permeation rate at high temperatures. Fig. 5.2 shows that only CO₂ rather than other carbon-containing products (CO and C₂-hydrocarbons) were observed when the BCFZ perovskite hollow fiber membrane is used for methane conversion without catalyst at 875 °C (Configuration A).

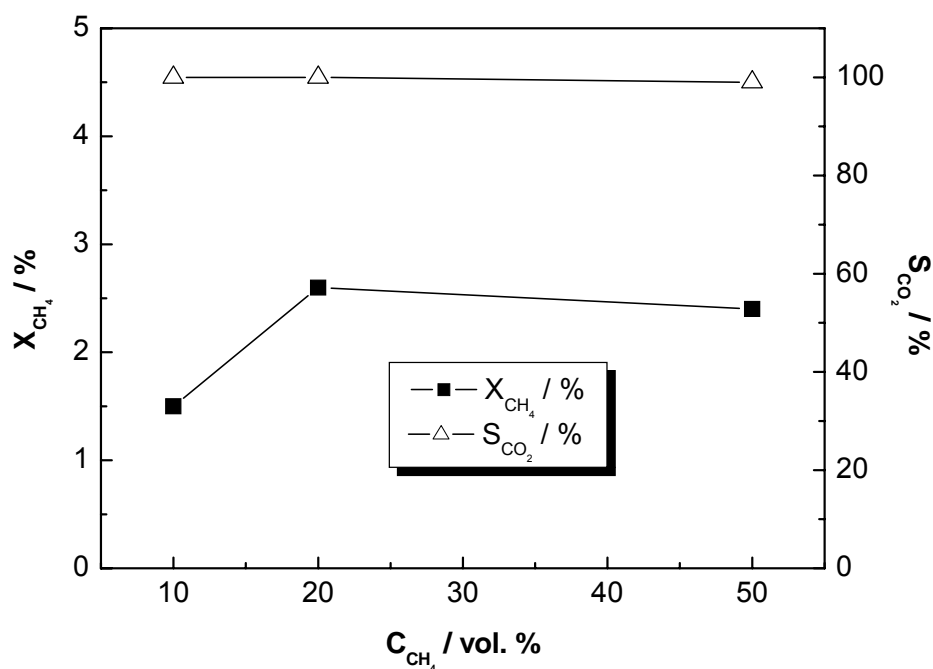


Figure 5.2 Catalytic performance of the POM in the BCFZ hollow fiber membrane reactor without reforming catalyst. Air flow rate on the shell side: 150 mL/min, the total flow rate on the core side: 30 mL/min, CH₄ concentration: 10 – 50 vol. %, membrane surface area: 3.3 cm², T = 875 °C.

Under standard experimental conditions, a large amount of un-reacted gaseous oxygen was observed at the outlet of the membrane reactor besides non-consumed methane. For elongated contact times, this CH₄/O₂ mixture would react in a gas phase combustion to

CO₂ and H₂O. Therefore, it is reasonable to use a suitable catalyst, which will catalyse the methane oxidation by gas-phase oxygen.

Similar results were reported by Balachandran et al. who found that in an SrFeCo_{0.5}O_x tubular membrane reactor (membrane surface area 8 cm²) in the absence of a reforming catalyst, the permeated oxygen reacted with methane, yielding CO₂ and H₂O [1]. The presence of CO₂, H₂O, CH₄, and O₂ were also reported by Tsai et al. in the effluent of a La_{0.2}Ba_{0.8}Fe_{0.8}Co_{0.2}O_{3-δ} disc-shaped membrane reactor (membrane surface area 0.28 cm²) without catalyst [2].

5.2 POM reaction in a modified hollow fiber membrane reactor with reforming catalyst layer

The Ni-based SR catalyst was coated on the outer surface of the hollow fiber perovskite membrane (Configuration B in Fig. 5.1). The modified hollow fiber membrane was characterized by field emission scanning electron microscopy and the micrographs are shown in Fig. 5.3. From the examination of the cross-section, a uniform and very thin catalyst layer is coated on the surface of the hollow fiber membrane. The micrograph of the coated hollow fiber membrane shows a catalyst layer of about 1 - 2 μm thickness.

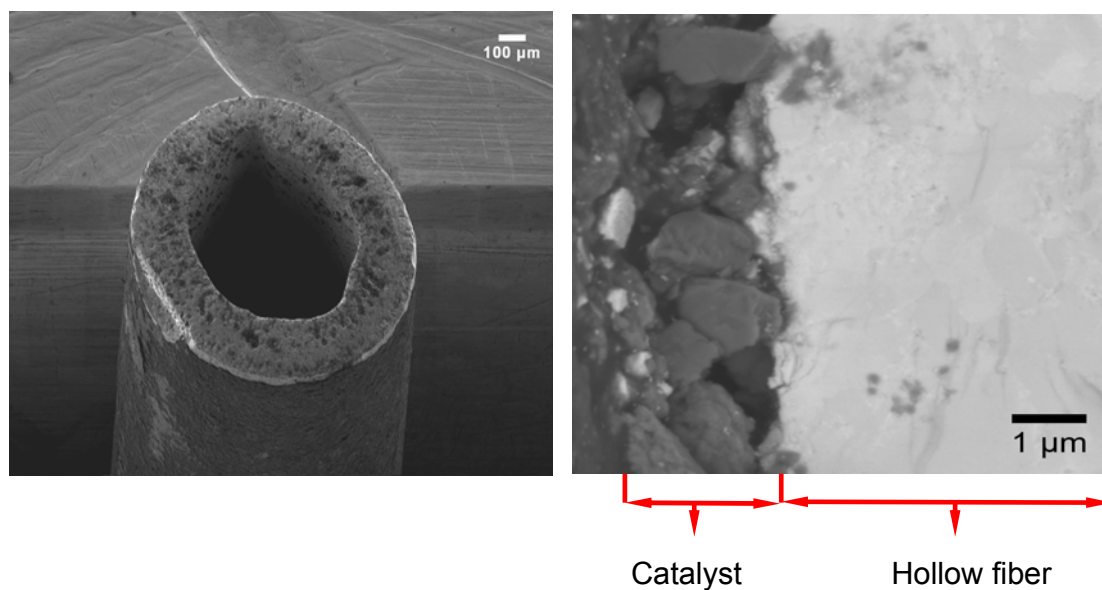


Figure 5.3 SEM images of the modified hollow fiber membrane with reforming catalyst layer

Fig. 5.4 shows the methane conversion, CO and CO₂ selectivity as well as the oxygen permeation flux as a function of the methane flux on the shell side when the air flow rate on the core side was 150 mL/min, and the total flow rate on the shell side was varied from 10 mL/min to 50 mL/min. A higher oxygen flux through the hollow fiber membrane compared to the uncoated fiber is obtained. It is clear that the oxygen permeation rate increased dramatically by changing from He to CH₄ on the permeating side due to the gradient of the oxygen partial pressure. The CH₄ conversion is much higher than that in the absence of the catalyst. However, the CO selectivity is very low which indicates that the methane reforming with the produced CO₂ and H₂O was not complete. More catalyst is needed and in the following section a certain amount of catalyst will be packed around the un-coated fiber for CH₄ reforming with the produced CO₂ and H₂O.

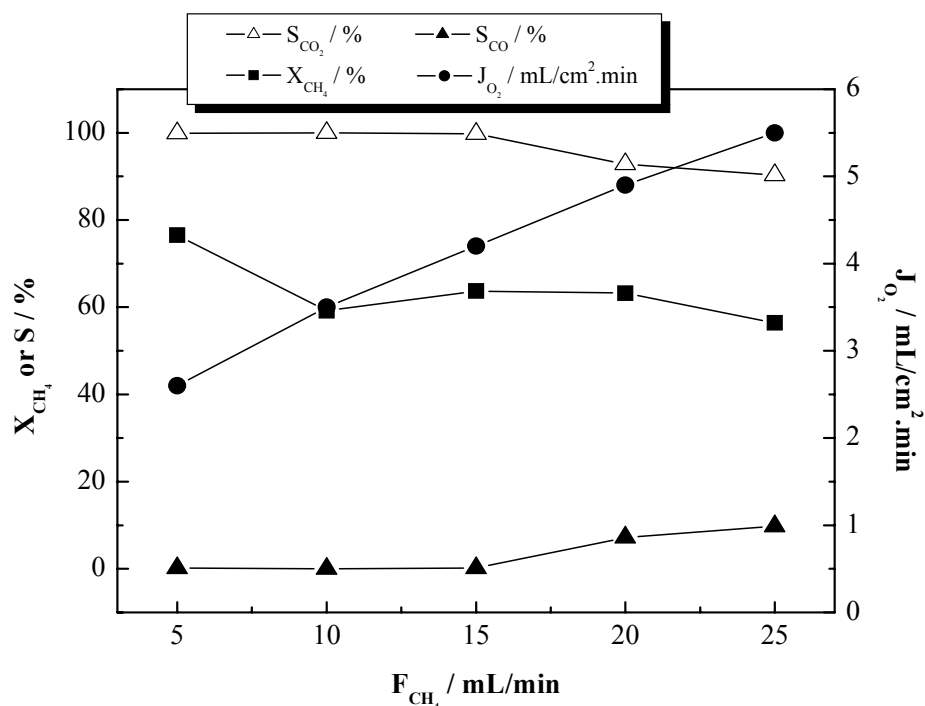


Figure 5.4 Catalytic performance of the POM in the modified BCFZ hollow fiber membrane reactor with reforming catalyst according the configuration B in Fig. 6.1. Air flow rate on the core side: 150 mL/min, the total flow rate of 50 vol. % methane on the shell side: 10 - 50 mL/min, $T = 875$ °C.

The BCFZ hollow fiber membrane survived only 5 hours when operated as a reactor for the POM reaction at 875 °C. It is well known that the BCFZ material is not stable in the CO_2 atmosphere [3]. Therefore it can be assumed that the structure of the hollow fiber membrane was destroyed by $BaCO_3$ formation because of the high amount of the CO_2 .

5.3 POM reaction in a hollow fiber membrane reactor with reforming catalyst

The Ni-based SR catalyst was applied as a packed bed ($\sim 0.16 - 0.4 \mu\text{m}$ particle size) around the perovskite fiber (shell side) (Configuration C in Fig. 5.1). In Fig. 5.5 it can be seen that the oxygen permeation flux in configuration C is much higher than that without Ni-catalyst. Consequently, the CH_4 conversion is considerably higher than that in the absence of the catalyst (Fig. 5.2). However, the CO selectivity is lower than 82 % and decreases with increasing temperature and considerable amounts of un-reacted methane were also found. At $925 \text{ }^\circ\text{C}$, both CO_2 and CO selectivities reach 50 % with only 70 % CH_4 conversion. This experimental finding indicates that the methane reforming with the produced CO_2 and H_2O was not complete. It seems that an additional amount of catalyst should be packed behind the un-coated fiber where the CH_4 reforming with produced CO_2 and H_2O can take place.

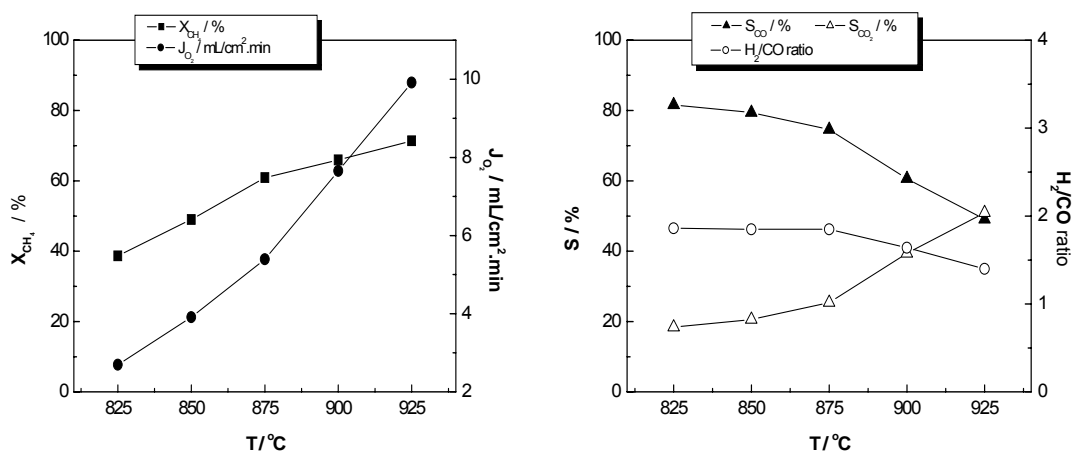


Figure 5.5 Catalytic performance of the POM in the BCFZ hollow fiber membrane reactor with reforming catalyst according the configuration C in Fig. 5.1. Air flow rate on the core side: 150 mL/min, the total flow rate of 50 vol. % methane on the shell side: 20 mL/min, $T = 825 - 925 \text{ }^\circ\text{C}$.

Fig. 5.6 shows the catalytic performance of the POM in the BCFZ perovskite hollow fiber membrane reactor with Ni-based SR catalyst around and behind the fiber (configuration D). A considerable improvement can be stated and CO and H₂ became the main reaction products (Fig. 5.6). At 925 °C, the CO selectivity is above 97 % with about 96 % CH₄ conversion and the H₂/CO ratio is around 2.0 as expected for the POM. The temperature increase in the CH₄ conversion is ascribed to the temperature-accelerated oxygen permeation flux. The changes in the catalytic performance of the membrane reactor in the presence of the Ni-based SR catalyst can be explained as follows. The perovskite membrane permeates oxygen from the air side to the hydrocarbon side. Since the membrane has very low intrinsic activity for methane oxidation (Fig. 5.2), methane conversion to syngas is concluded to occur exclusively over the Ni-based SR catalyst.

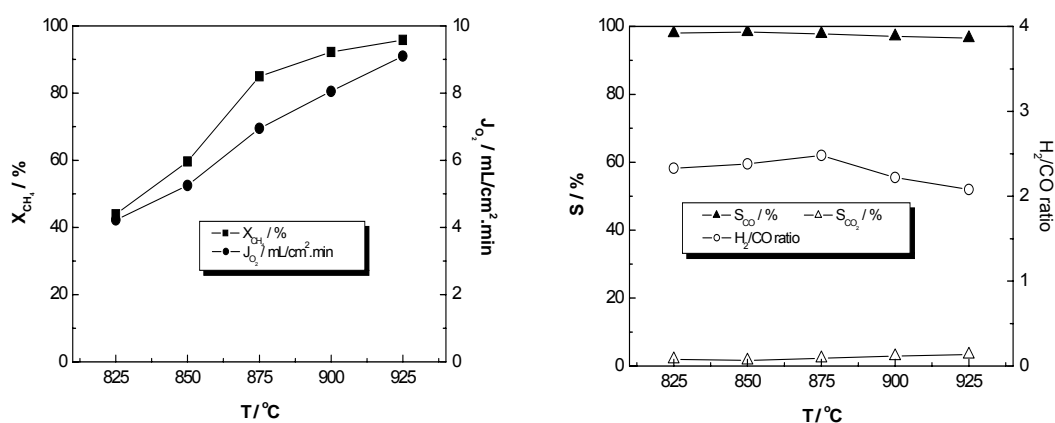


Figure 5.6 Catalytic performance of the POM in the BCFZ hollow fiber membrane reactor with reforming catalyst according the configuration D in Fig. 5.1. Air flow rate on the core side: 150 mL/min, the total flow rate of 50 vol. % methane on the shell side: 20 mL/min, T = 825 – 925 °C.

5.4 Possible pathways of reactions for the POM to syngas in a hollow fiber membrane reactor with reforming catalyst

Dissanayake et al. [4] studied a Ni-based catalyst for the POM in the conventional packed bed reactor. They found that the catalyst bed consists of three different regions. The first of these, contacting the initial $\text{CH}_4/\text{O}_2/\text{He}$ feed mixture, is NiAl_2O_4 , which has only moderate activity for complete oxidation of methane to CO_2 and H_2O . The second region is $\text{NiO} + \text{Al}_2\text{O}_3$, over which complete oxidation of methane to CO_2 occurs, resulting in a strong temperature increase in this section of the bed. As a result of complete consumption of O_2 in the second region, the third portion of the catalyst bed consists of a reduced $\text{Ni}/\text{Al}_2\text{O}_3$ phase. Formation of the CO and H_2 products, corresponding to the thermodynamic equilibrium at the catalyst bed temperature, occurs in this final region, via reforming reactions of CH_4 with the CO_2 and H_2O produced during the complete oxidation reaction over the $\text{NiO}/\text{Al}_2\text{O}_3$ phase. Taking into account the recently reviewed data on syngas production over various catalytic materials [5], CO and H_2 are suggested to be formed via indirect methane oxidation, i.e. the total methane oxidation to CO_2 and H_2O followed by steam and dry reforming of methane.

According to the reaction mechanism for the POM using the Ni-based catalyst obtained in the conventional packed bed reactor [4, 5], Fig. 5.7 summarizes possible reaction pathways for the POM to syngas in the hollow fiber membrane reactor. In the case of no catalyst, i.e., reaction zone 1 in Fig. 5.7, to some extent the combustion of methane takes place.



In the reaction zone 2 in Fig. 6.6, a part of methane reacts with oxygen that diffused or spilt over the catalyst from the membrane surface to form CO_2 and H_2O as reaction (1). The produced CO_2 and H_2O in reaction zones 1 and 2 will be converted with CH_4 to give CO and H_2 by dry reforming and steam reforming, respectively.



Some of the CO and H₂ formed by the reforming reactions (6.2) and (6.3) are oxidized with oxygen on the membrane surface to produce CO₂ and H₂O possibly by the following reactions, resulting in the decrease of the CO selectivity as found in Fig. 5.5 and resulting in an increase of the oxygen permeation flux [6]:



After packing further catalyst behind the permeation zone of the fiber, the reforming of the un-reacted CH₄ with CO₂ and H₂O produced by reactions (5.4) and (5.5) takes place to give CO and H₂ following the reactions (5.2) and (5.3) in reaction zone 3. Therefore, high CO selectivity with high CH₄ conversion was obtained when the configuration D was used. These experiments show that the so-called partial oxidation of methane to syngas in the dense perovskite membrane reactor is possibly first a total oxidation followed by reforming steps. H₂O and CO₂ become reduced by un-reacted CH₄ by SR and dry reforming giving CO and H₂ using especially the established Ni-based SR catalysts. Consequently, the synthesis gas formation from methane in a mixed conducting perovskite membrane reactor is called an “oxidation-reforming process” [7].

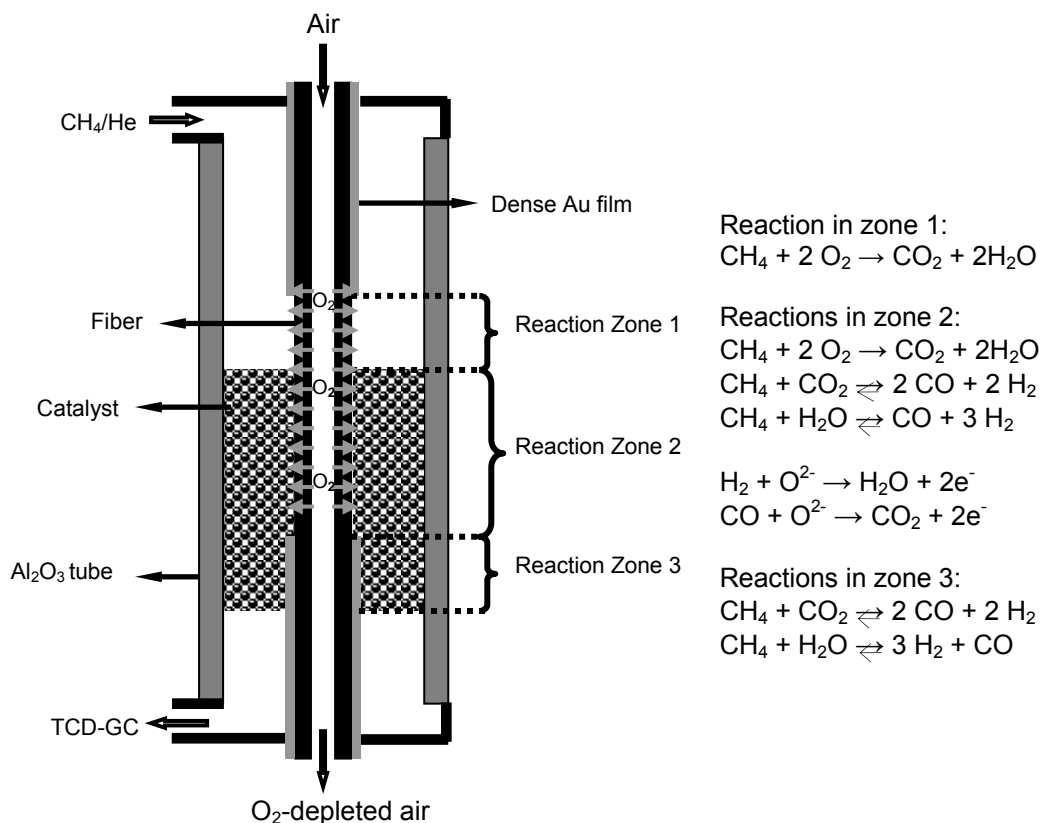


Figure 5.7 Possible reaction pathways in the BCFZ perovskite hollow fiber membrane reactor.

5.5 Stability of the hollow fiber membrane during the POM reaction

Ideal materials for the membrane reactor must have sufficient mechanical strength and maintain chemical stability at the desired oxygen permeation flux under the reductive reaction condition. Although recent reports have described various perovskite-type materials that could be used as ceramic membrane reactors for POM, only a few materials can be operated steadily for a long time under the syngas reaction condition. Balachandran et al [1, 8, 9] investigated POM to produce syngas by using tubular $\text{La}_{0.2}\text{Sr}_{0.8}\text{Co}_{0.2}\text{Fe}_{0.8}\text{O}_{3-\delta}$ (LSCF) and $\text{SrCo}_{0.8}\text{Fe}_{0.2}\text{O}_{3-\delta}$ (SCF) membrane reactors. They found that the membranes

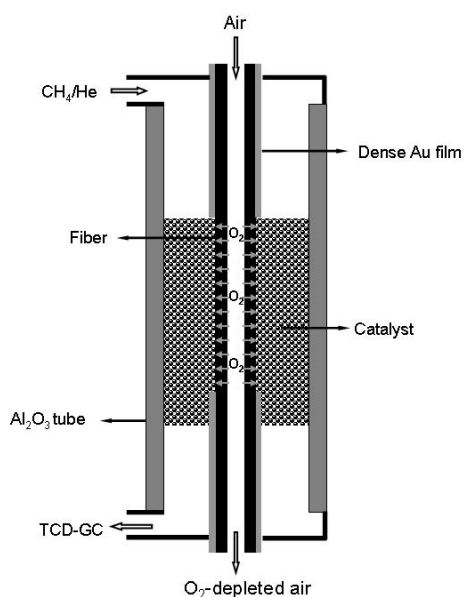
broke into several pieces within a few minutes after methane was introduced to the membrane reactor at 850 °C. Pei et al. [10] studied the failure mechanism of ceramic membrane reactors on POM to syngas. They observed two types of fractures occurring on the SCF membrane reactor. The first type occurred shortly after the reaction started and the second type often occurred days after the reaction. They also found the first fracture was the consequence of oxygen gradient across the membrane from reaction side to the air side, which causes a little mismatch inside the membrane, leading to fracture; the second type of fracture was the result of a chemical decomposition in the reductive atmosphere. No fractures occurred for the $\text{Ba}_{0.5}\text{Sr}_{0.5}\text{Co}_{0.8}\text{Fe}_{0.2}\text{O}_{3-\delta}$ (BSCF) membrane reactor during the POM reaction [11]. BSCF membrane exhibits better phase stability than the SCF because proper substitution of strontium ion in SCF with barium ion with a larger radius can increase the tolerance factor (near to 1) [12].

The perovskite $\text{BaCo}_x\text{Fe}_y\text{Zr}_z\text{O}_{3-\delta}$ [13] is an excellent oxygen permeable membrane material. This material possesses the following properties: (1) a high oxygen permeation flux; (2) a stable lattice structure under high concentrations of hydrogen, carbon monoxide and carbon dioxide; (3) lower steady operation temperature. In order to apply successfully these materials in the fabrication of MIECM reactors for POM reaction, the structural stability of BCFZ materials under reducing atmospheres was also investigated [13].

The long-term stability of the BCFZ disc membrane reactor for the partial oxidation of methane shows that during more than 2200 h running, the oxygen permeation flux was stable, similar to the stable reaction performance of CH_4 conversion, CO selectivity and the ratio of H_2 to CO. This long-term stable operation showed that the BCFZ membrane reactor was more stable than any other mixed conducting membrane reactors for the POM reaction published so far, except for that constructed from $\text{Sr}_{1.7}\text{La}_{0.3}\text{Ga}_{0.6}\text{Fe}_{1.4}\text{O}_{5.15}$ (SLGF) [14]. But it was well known that not only the gallium element was more expensive but also its oxygen permeation flux was too low to be suitable for practical application. These two shortcomings made SLGF not suitable for constructing a reactor for the POM reaction, when compared with the new material of BCFZ developed by J. Tong et al. [15]. For stability measurements two catalyst arrangements were studied. Fig. 5.8 shows a schematic diagram of the membrane reactor used in this study. 150 mL/min air was fed to

the core side and a mixture of CH_4 and He was fed to the shell side. The two ends of the hollow fiber were coated by Au paste and sintered at $950\text{ }^\circ\text{C}$ with obtaining of a dense Au film. Thus the uncoated part of the hollow fiber membrane is kept in the middle of the oven where the temperature is constant. In the configuration D, the Ni-based SR catalyst was packed around and behind the hollow fiber membrane. In the configuration E, the catalyst was packed only behind the hollow fiber membrane.

D



E

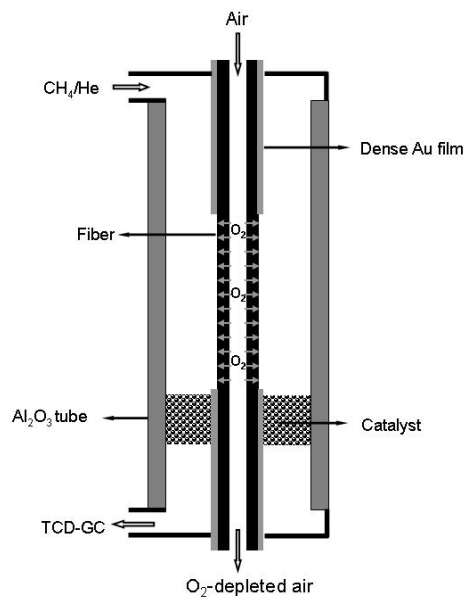
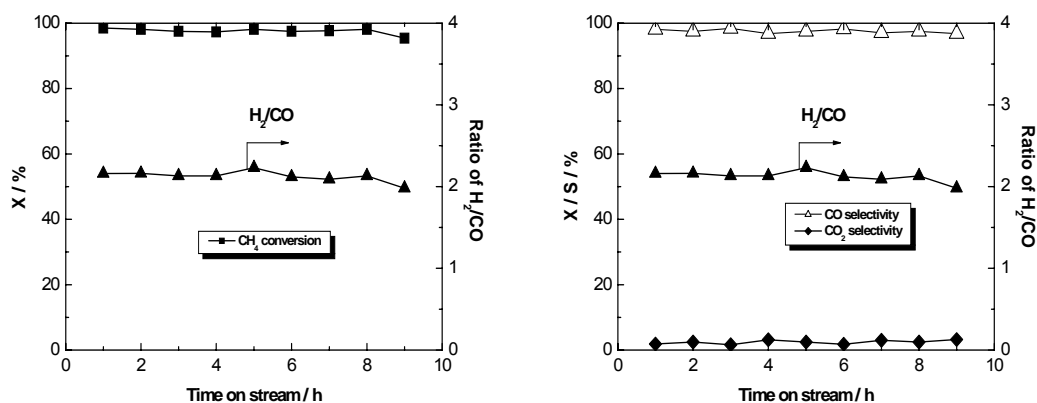


Figure 5.8 Schematic diagram of different types of catalyst arrangement for stability of BCFZ hollow fiber membrane during POM. Case D: catalyst around and behind fiber, case E: catalyst behind fiber.

Fig. 5.9 shows the stability measurements for the POM reaction in the hollow fiber membrane reactor for both configurations at $875\text{ }^\circ\text{C}$. CO and H_2 became the main reaction products. A very high CH_4 conversion and CO selectivity are obtained and the H_2/CO ratio is 2.0 as expected for the POM reaction. For both cases the hollow fiber membranes are broken after 9 h and 35 h, respectively. It is important to note that the fractures occurred on the BCFZ hollow fiber membrane reactor during the POM reaction process,

after few hours in comparison to BCFZ disc membrane reactor, which is very stable for a long time [15].

Case A



Case B

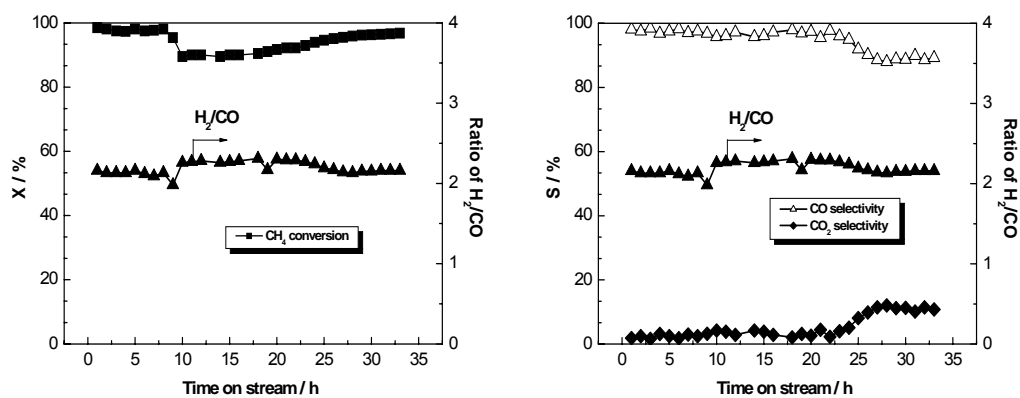


Figure 5.9 Stability of the fiber during POM reaction according the configurations in Fig. 5.8. Air flow rate on the core side: 150 mL/min, the total flow rate of 50 vol. % methane on the shell side: 20 mL/min, membrane area: 0.43 cm², T = 875 °C, Ni-based SR catalyst = 0.6 g (Case D) and Ni-based SR catalyst = 0.4 g (Case E).

The hollow fiber membranes used for the POM reaction with packed Ni-based SR catalyst are broken after few hours. Fig. 5.10 shows where the membranes are broken during the POM reaction. As it can be seen from the Fig. 5.10 that in case D the hollow fiber membrane was broken in the middle, where the membrane contacted with the Ni-based SR catalyst. In the case E the dense Au film was destroyed and the catalyst contacted with the membrane which resulted in a fiber destruction.

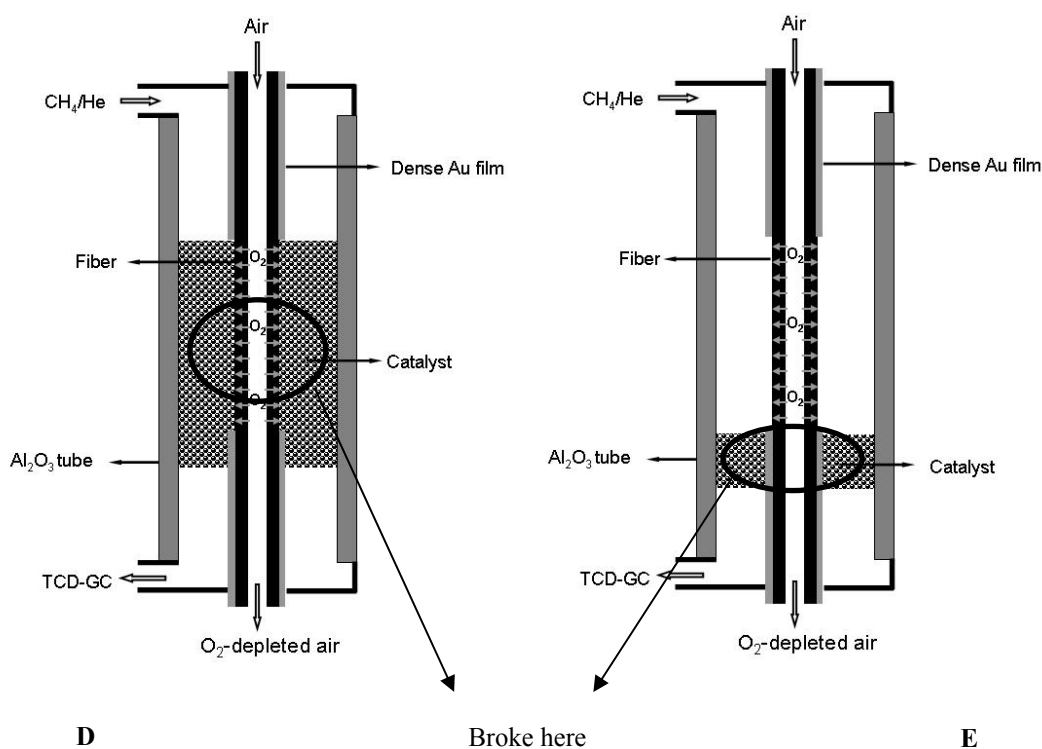


Figure 5.10 Schematic diagrams of destroyed BCFZ hollow fiber membrane reactors with different catalyst arrangement. Case D: catalyst around and behind fiber, case E: catalyst behind fiber.

The destroyed hollow fiber membrane after POM reaction was studied by SEM and EDXS analysis. Fig. 5.11 shows the micrographs of the spent hollow fiber perovskite membranes used for partial oxidation of methane to syngas. As it is shown in the Fig. 5.11 the fiber was broken in the middle. The fiber contacted with the Ni-based SR catalyst became amorphous and porous, especially on its outer surface. From the whole wall thickness of

the hollow fiber membrane, only 40 μm remained dense, the rest of the wall became porous.

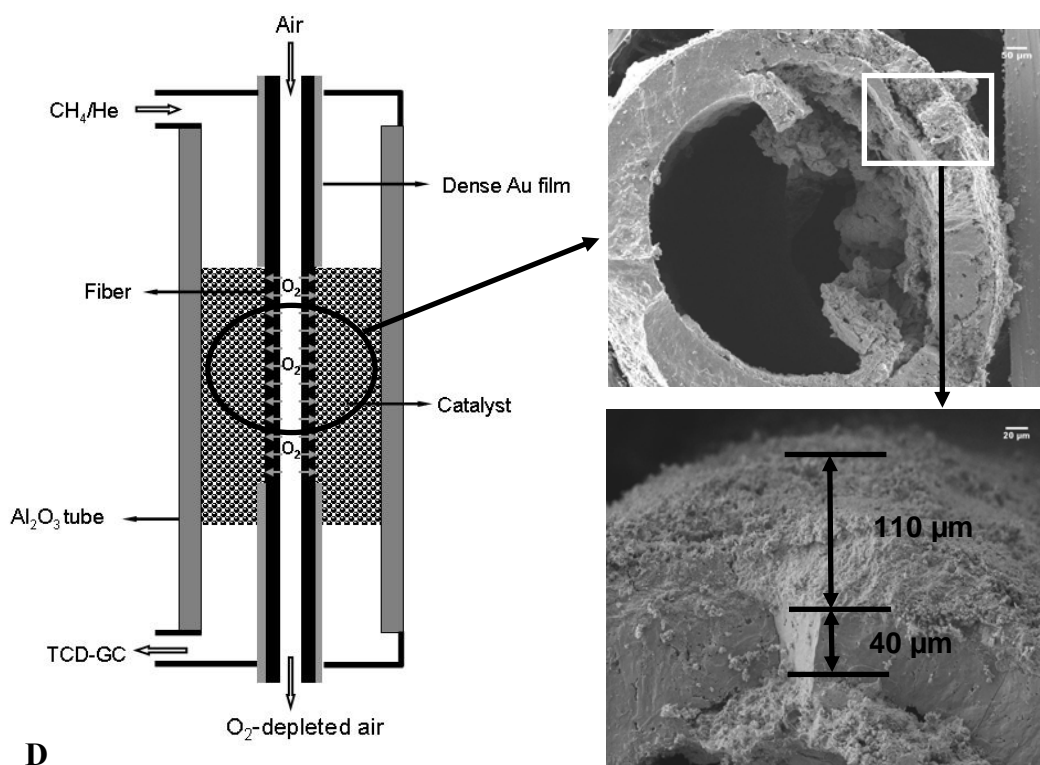


Figure 5.11 SEM micrographs of the cross section of the spent membrane. Case D: catalyst around and behind the fiber.

Consequently, the spent hollow fiber membrane was examined by EDXS analysis. As it can be seen from the Fig. 5.12 the spectrum of the outer and middle parts of the cross section of the porous fiber contains Al. The Al diffusion into the wall of the perovskite fiber may be a reason that the fiber is broken in this case. No Al content in the spectrum of the inner intact part (40 μm) of the hollow fiber membrane was observed.

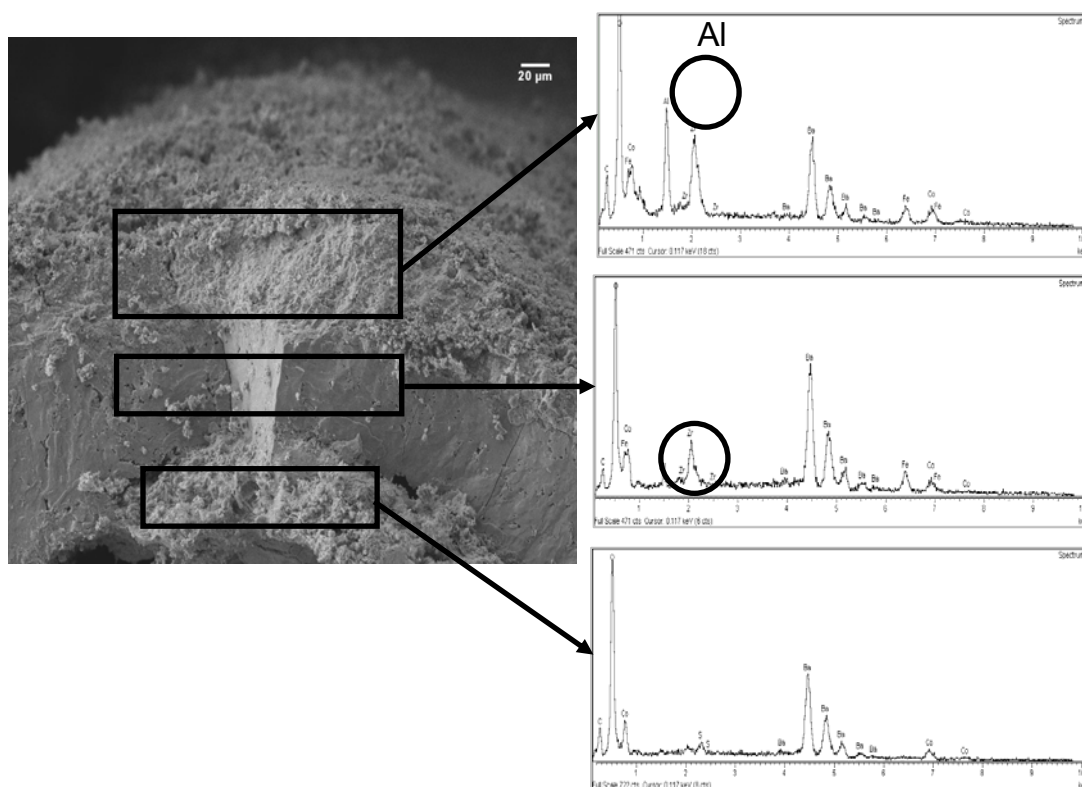


Figure 5.12 EDXS spectra of the cross section of the spent membrane. Case D: the catalyst around and behind the fiber.

Avoiding the catalyst contacting with the fiber can improve the stability of the membrane for the POM reaction (Fig. 5.13). Therefore in case E the catalyst was positioned behind the oxygen permeation zone and in this catalyst region the fiber was coated with Au. The uncoated fiber was found to be dense after the POM reaction, but the part of fiber coated with Au paste contacting the Ni-based SR catalyst was unexpectedly destroyed. The protect Au film was destroyed and the catalyst contacted and reacted directly with the fiber. The fiber became porous after reacting with the Ni-based SR catalyst as in the case D. It is concluded that perfect protecting layers are necessary.

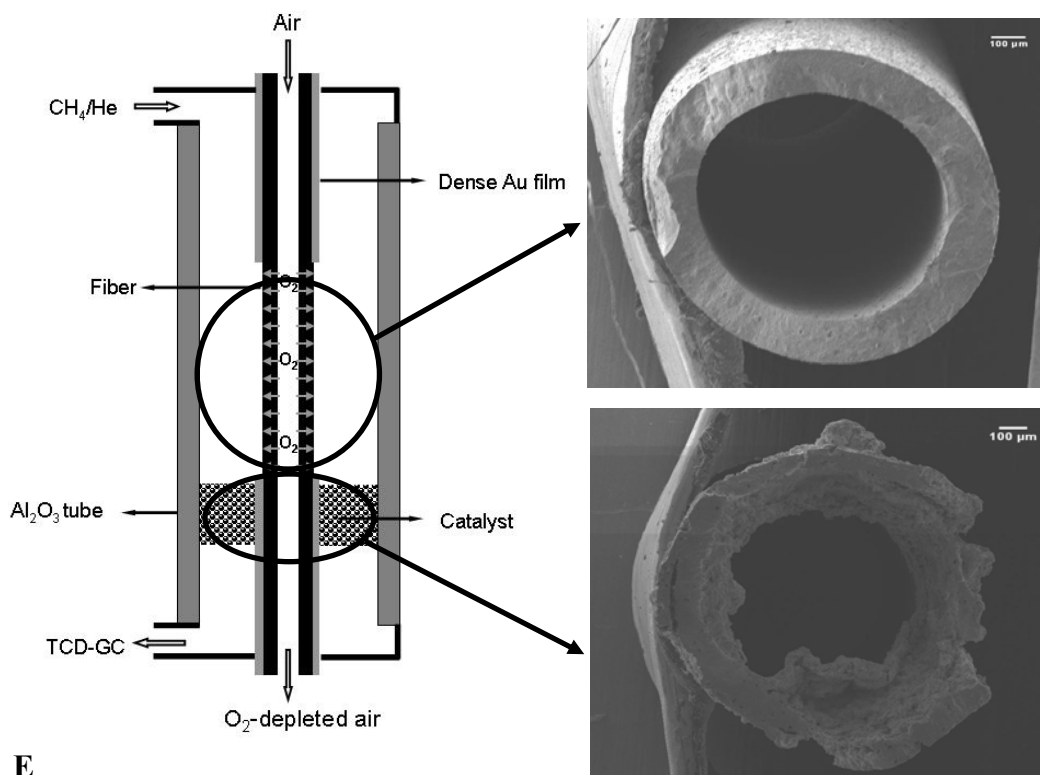


Figure 5.13 SEM micrographs of the cross section of the spent membrane. Case E: catalyst behind the fiber.

5.6 Conclusions

The POM to syngas was investigated at 825 – 925 °C using a BCFZ hollow fiber perovskite membrane reactor with/without Ni-based SR catalyst. Possible reaction pathways for POM were proposed. It was implied that CO and H₂ were formed by reforming reactions of methane with CO₂ and H₂O in the hollow fiber membrane reactor on the catalyst bed. Additional catalyst was needed packed behind the hollow fiber membrane to ensure that the reforming reactions take place completely. A suitable location of the Ni-based steam reforming (SR) catalyst seems to be behind the fiber. Avoiding catalyst contacting with fiber can improve the stability. The Ni-based SR

catalyst is capable of exhibiting good activity towards the oxidation of methane to synthesis gas.

The oxygen permeation flux of the hollow fiber membrane in POM reaction was very high compared to helium as sweep gas (He/Air). The BCFZ material is not stable in CO₂ atmosphere and the decomposition of the perovskite material due to BaCO₃ formation is believed as failure mechanism of the membrane reactor after 35 h of measurements. Another failure mechanism is the destruction of the perovskite by Al from the catalyst.

5.7 Bibliography

- [1] U. Balachandran, J. T. Dusek, P. S. Maiya, B. Ma, R. L. Mieville, M. S. Kleefisch, C. A. Udovich, *Catal. Today* 36 (1997) 265.
- [2] C. Y. Tsai, A. G. Dixon, Y. H. Ma, W. R. Moser, M. R. Pascucci, *J. Am. Ceram. Soc.* 81 (1998) 1437.
- [3] J. Tong, W. Yang, B. Zhu, R. Cai, *J. Membr. Sci.* 203 (2002) 175.
- [4] D. Dissanayake, M. P. Rosynek, K. C. C. Kharas, J. H. Lunsford, *J. Catal.* 132 (1991) 117.
- [5] E. V. Kondratenko, M. Baerns, *Encyclopedia of Catalysis*, I. Horvyth (Ed.), John Wiley and Sons, 6 (2003) 424.
- [6] M. Ikeguchi, T. Mimura, Y. Sekine, E. Kikuchi, M. Matsukata, *Appl. Catal. Gen. A* 290 (2005) 212.
- [7] C. S. Chen, S. J. Feng, S. Ran, D. C. Zhu, W. Liu, H. J. M. Bouwmeester, *Angew. Chem. Int. Ed.* 42 (2003) 5196.
- [8] U. Balachandran, J. T. Dusek, S. M. Sweeney, R. B. Poeppel, R. L. Mieville, P. S. Maiya, M. S. Kleefisch, S. Pei, T. P. Kobylinski, C. A. Udovich and A. C. Bose, *Am. Ceram. Soc. Bull.* 74 (1995) 71.
- [9] U. Balachandran, J. T. Dusek, R. L. Mieville, R. B. Poeppel, M. S. Kleefisch, S. Pei, T. P. Kobylinski, C. A. Udovich and A. C. Bose, *Appl. Catal. A* 133 (1995) 19.
- [10] S. Pei, M. S. Kleefisch, T. P. Kobylinski, J. Faber, C. A. Udovich, V. Zhang-

McCoy, B. Dabrowski and U. Balachandran, *Catal. Lett.* 30 (1995) 201.

[11] H. Wang, Y. Cong, W. Yang, *Cat. Today* 82 (2003) 157.

[12] Z. P. Shao, H. Dong, G. X. Xiong, Y. Cong, W. S. Yang, *J. Membr. Sci.* 172 (2001) 177.

[13] J. H. Tong, W. S. Yang, B. C. Zhu, R. Cai, *J. Membr. Sci.* 203 (2002) 175.

[14] M. Schwartz, J. H. White, A. F. Sammells, *Int. Patent*, WO 99/21649 (1999).

[15] J. H. Tong, W. S. Yang, R. Cai, B. C. Zhu, L. W. Lin, *Catal. Lett.* 78 (1-4) (2002) 129.

6 Selective oxidations of C₂H₆ over a MIECM perovskite – a TAP and membrane reactors study

The objective of this chapter is to study the oxidative activation of light hydrocarbons, especially the oxidative dehydrogenation of ethane to ethylene (ODE), and the partial oxidation of methane to syngas (POM), in a perovskite MIEC membrane reactor. The first results of the ODE in the BCFZ perovskite hollow fiber membrane reactor are included. The temporal analysis of products (TAP) technique [1] was employed to understand the possible reaction mechanisms on the membrane surface. As described in Section 2.6.1 the TAP measurements were made by Dr. E. Kondratenko. The perovskite MIEC membrane as well as the catalyst used in the TAP were made from BaCo_xFe_yZr_zO_{3-δ} (BCFZ). The BCFZ membrane was used in a hollow fiber geometry, which was developed in the CaMeRa (Catalytic Membrane Reactor) project under the auspices of ConNeCat (Competence Network Catalysis) of the German BMBF.

Although the principle of the catalytic membrane reactor for the ODE is easily understood, in practice the concept is much more complex. Three aspects of membrane reactors and their relationship to each other have to be taken into account: (1) Oxygen permeation rates through the hollow fiber with respect to the feed gas and sweep gas; (2) the intrinsic catalytic activity for the ODE of the membrane material; (3) the process parameters, which have a huge effect on the ODE performance and thus determine the ethane conversion, and ethylene selectivity. The relationships between the reaction rate, the flow rate, and the permeation rate through the hollow fiber membrane are very important in optimizing the process conditions.

6.1 Test of the catalytic activity of BCFZ in the ODE

For a catalytic membrane reactor, the membrane material should not only possess sufficient oxygen permeability but also necessary catalytic activity for the ODE. Therefore, the catalytic activity of BCFZ for the ODE was investigated using pelletized BCFZ powder in a co-feed packed bed reactor. A quartz tube ($\Phi = 6$ mm) was employed as the reactor. 0.6 g 30-60 meshes BCFZ particles were packed in the quartz reactor as the catalyst. Ethane and air were co-fed to the reactor. The mole ratio of ethane to air is 2:5, i.e. the mole ratio of ethane to oxygen is 2:1, which is the stoichiometric ratio of the ODE. The total flow rate of ethane and air is 40 mL/min. All the oxygen was consumed in the ODE. Ethane conversion and ethylene selectivity as a function of temperature are shown in Fig. 6.1. When the reaction temperature increased from 700 °C to 850 °C, ethane conversion increases from 55 % to 98 % and ethylene selectivity decreases from 54 % to 24 %. With increasing temperature, CO becomes the main product. These results demonstrate that the BCFZ shows moderate catalytic activity in the ODE reaction at lower temperatures.

The BCFZ catalytic activity of the ODE under a reducing environment was also tested in a quartz reactor ($\Phi = 6$ mm) with 0.6 g 30 - 60 meshes BCFZ particles in the periodically operated mode. Air was introduced to oxidize the BCFZ for 30 minutes, then helium instead of air swept the reactor until no nitrogen was detected; finally, a mixture of 10 % ethane and 90 % helium with the flow rate of 40 mL/min was introduced into the reactor. At 700 °C, the ethylene selectivity remained unchanged at around 88 %, although the ethane conversion is low (~3 %) and decreases with time. Compared to a reducing environment, lower ethylene selectivity was achieved in the present of O₂ in the co-feed packed bed reactor, which was due to the reaction between the gaseous oxygen and the produced ethylene.

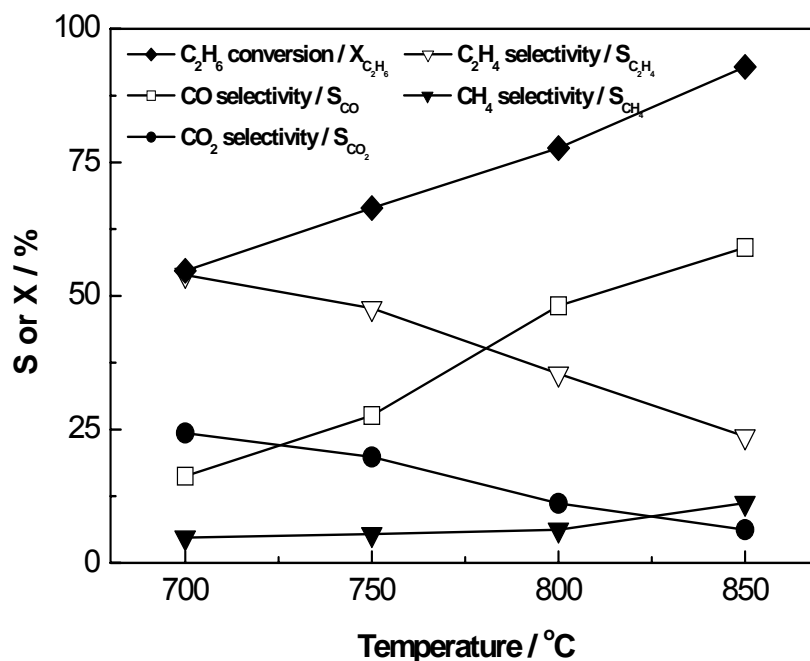


Figure 6.1 Catalytic activity of BCFZ for the oxidative dehydrogenation of ethane to ethylene in a co-feed packed bed reactor.

6.2 C₂H₆ and CH₄ oxidation over oxidized BCFZ catalyst under transient vacuum conditions in the TAP reactor

Transient analysis of C₂H₆ and CH₄ interactions with a perovskite BCFZ formula was performed in the TAP-2 reactor [2, 3]. CO₂ and C₂H₆ were detected at the reactor outlet upon pulsing a CH₄:Ne = 1:1 mixture over the pre-oxidized BCFZ perovskite at 875 °C. The formation of other possible products (C₃H₈, C₃H₆, CO, H₂CO, CH₃OH, C₂H₄ and C₂H₂, H₂) in significant amounts is unlikely. CO₂ was the main carbon-containing product. The presence of C₂H₆ in the reaction products indicates that the pre-oxidized BCFZ perovskite catalyses the oxidative coupling of methane (OCM). For this reaction, it is well accepted that C₂H₆ is formed via coupling of two methyl radicals [4]. It has to be particularly stressed that all the reaction products were formed by CH₄ oxidation with lattice oxygen of the perovskite, because gas-phase oxygen was not present in the CH₄ pulse.

CO₂ was also the main carbon-containing reaction product detected at the reactor outlet, when a C₂H₆:Ne = 1:1 mixture was pulsed over the pre-oxidized BCFZ perovskite at 800 °C. Additionally to CO₂, C₂H₄ was observed in the gas phase, however, as a minor product. Again as in the case of CH₄ oxidation, lattice oxygen of the pre-oxidized perovskite is responsible for C₂H₆ oxidation and respective products formation. In order to derive mechanistic insights into CH₄ and C₂H₆ oxidation, transient responses of the reaction products and the feed components were normalized by their height. Such normalization enables to better compare the shape and the appearance order of the feed components and the respective products. These parameters contain information on chemical and transport phenomena occurring in the reactor [1]. Figs. 6.2a and 6.2b exemplify the height-normalized transient responses of C₂H₆ and CH₄ pulsing over the pre-oxidized BCFZ perovskite, respectively.

The transient response of C₂H₆ is shifted to longer times and slightly broader than that of CH₄, because C₂H₆ is a product of CH₄ oxidation (Fig. 6.2a). The transient response of CH₄ obtained in the CH₄ pulse experiments has the sharpest shape, which indicates CH₄ oxidation. In contrast to the transient responses of both hydrocarbons, the transient response of CO₂ is very broad and shifted to considerably longer times. Based on the appearance order of these transient responses, their shapes and the high ratio of CO₂/C₂H₆, it is concluded that CH₄ is primary converted to C₂H₆ followed by consecutive oxidation of C₂H₆ to CO₂. This conclusion agrees with the well-accepted mechanistic concept of the OCM reaction over various oxide catalytic materials [4]. However, from the present data it is not possible to unambiguously exclude CO₂ formation via direct CH₄ oxidation (e.g. oxidation of methyl radicals), since shifting of the CO₂ transient and its very broad shape as compared to that of C₂H₆ is also attributed to the strong adsorption of CO₂ over BaO followed by its slow desorption. Taking into account the results in Fig. 6.4, CO₂ formation via C₂H₆ oxidation at high degrees of CH₄ conversion should prevail over that from CH₄. The formation of BaCO₃ may explain the poor (ca. 70 %) carbon balance in the CH₄ pulse experiments. Coke deposition cannot be also excluded. Similar to the experiments with CH₄, the results of C₂H₆ pulse experiments shown in Fig. 6.2b can be interpreted in the following way. C₂H₆ is oxidatively dehydrogenated by lattice oxygen of the oxidized

BCFZ perovskite yielding C_2H_4 as primary product. CO_2 is formed via consecutive oxidation of C_2H_4 .

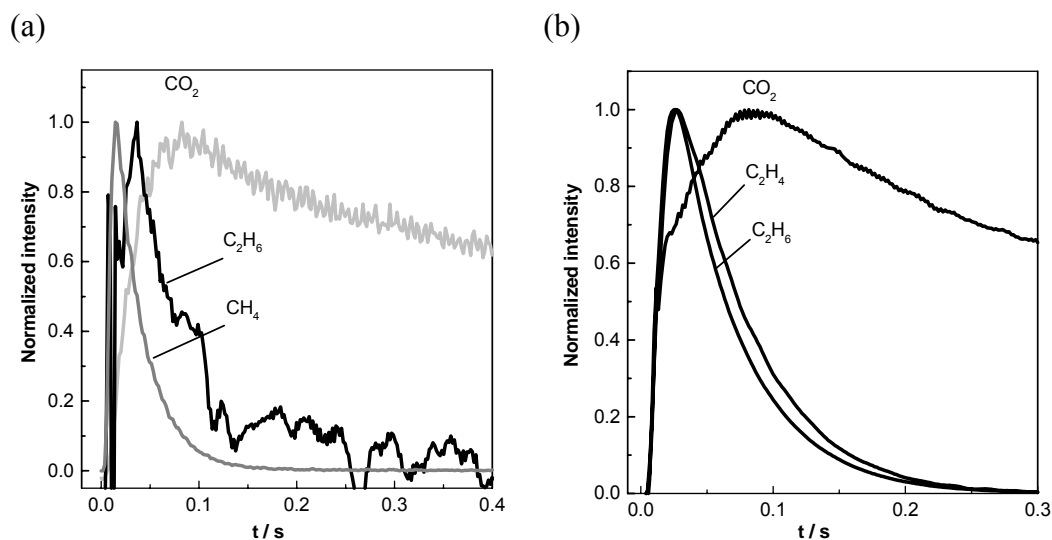


Figure 6.2 Height-normalized transient responses of C_2H_6 , CH_4 and CO_2 obtained during pulsing of a $CH_4/Ne = 1$ mixture (a) and height-normalized transient responses of C_2H_6 , C_2H_4 and CO_2 obtained during pulsing of a $C_2H_6/Ne = 1$ mixture (b) over the oxidized BCFZ perovskite ($m = 0.140$ g) at 800 °C (for C_2H_6) and 875 °C (for CH_4) in the TAP reactor.

Fig. 6.3 shows changes of C_2H_6 and CH_4 conversion upon increasing in the amount of lattice oxygen removed by hydrocarbons from the catalyst. The C_2H_6 conversion decreases stronger than the CH_4 conversion. This may be due to the fact that more lattice oxygen species are needed for the formation of CO_2 from C_2H_6 as compared to CH_4 . Not only hydrocarbon conversions but also product distribution are changed with progressive hydrocarbon pulsing.

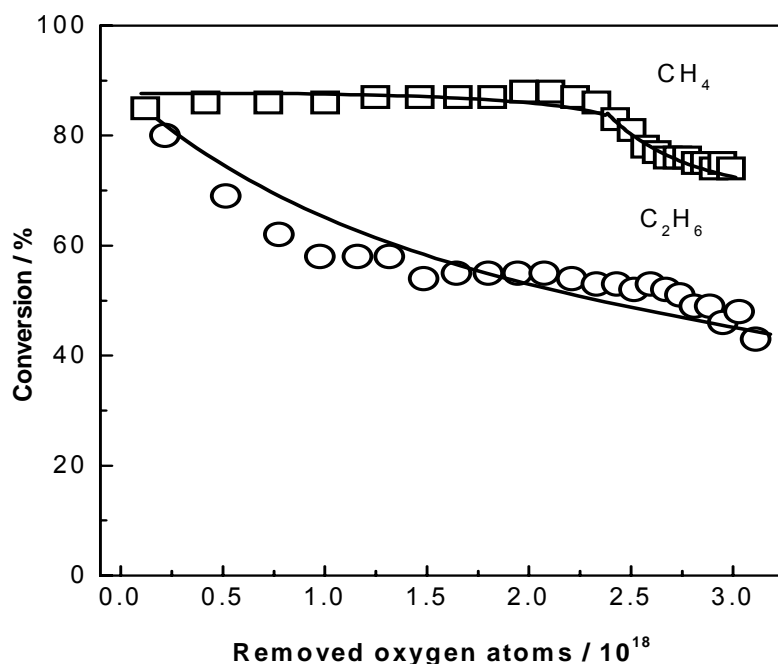


Figure 6.3 C₂H₆ and CH₄ conversions vs. amount of removed oxygen (pulsing of a C₂H₆/Ne = 1 mixture at 800 °C and pulsing of a CH₄/Ne = 1 mixture at 875 °C).

As shown in Fig. 6.4 the ratios of $S(\text{C}_2\text{H}_4)/S(\text{CO}_2)$ in the C₂H₆ interactions and $S(\text{C}_2\text{H}_6)/S(\text{CO}_2)$ in the CH₄ interactions increase with an increase in the amount of oxygen removed. With other words, selective reactions (oxidative ethane dehydrogenation to ethylene or oxidative coupling of methane) are favored by increased degree of catalyst reduction. This can be easily understood by taking into consideration the difference in the stoichiometry of selective and non-selective reaction pathways of C₂H₆ and CH₄ oxidations. Only one lattice oxygen is need for C₂H₆ oxidation to C₂H₄ or for CH₄ oxidation to C₂H₆, while four or seven lattice oxygen species are required for CO₂ formation from C₂H₆ or CH₄, respectively. The low initial $S(\text{C}_2\text{H}_4)/S(\text{CO}_2)$ and $S(\text{C}_2\text{H}_6)/S(\text{CO}_2)$ ratios are due to very high concentration of lattice oxygen in comparison to the amount of hydrocarbon (C₂H₆ or CH₄) pulsed. With increasing number of the hydrocarbon pulsed the concentration of lattice oxygen decreases due to its removal via interactions with ethane or methane. Therefore, active lattice oxygen species are expected

to become more isolated on the catalyst surface. In turn the non-selective secondary oxidation of hydrocarbon to CO_2 is inhibited, because for CO_2 formation more than one neighboring lattice oxygen is needed.

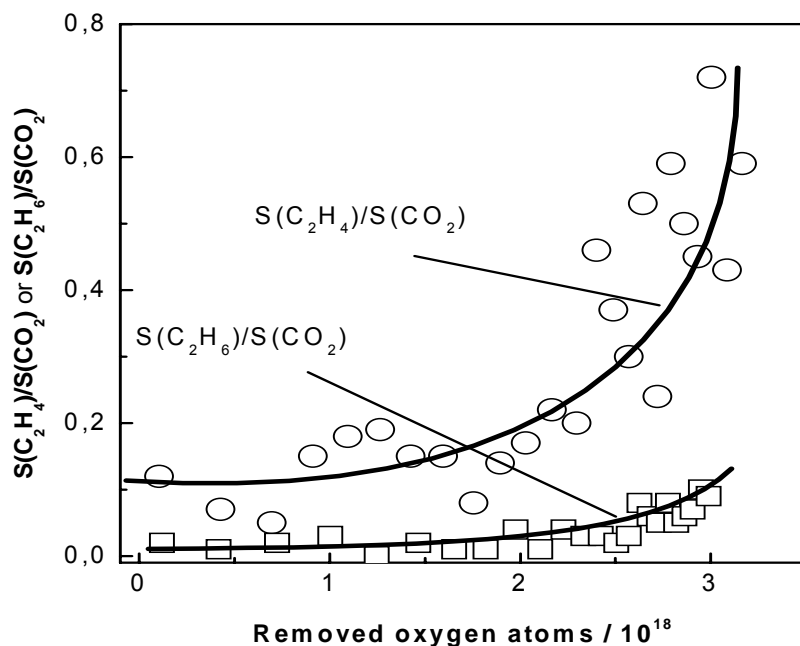


Figure 6.4 Ratios of $S(\text{C}_2\text{H}_4)/S(\text{CO}_2)$ and $S(\text{C}_2\text{H}_6)/S(\text{CO}_2)$ vs. the amount of removed oxygen during pulsing of a $\text{CH}_4/\text{Ne} = 1$ mixture at 875°C and a $\text{C}_2\text{H}_6/\text{Ne} = 1$ mixture at 800°C , respectively.

6.3 Ethane and methane oxidative transformations in the BCFZ membrane reactor

In order to avoid the gaseous oxygen contacting directly with hydrocarbons, the BCFZ membrane was employed as the reactor for the oxidative transformations. In this way, the hydrocarbon and the oxygen were separately fed to the reactor, so the CO and ethylene selectivity could be increased. Furthermore, the oxygen can be continuously supplied through the membrane in the form of oxygen ions, so higher hydrocarbon conversion can

be expected as it was demonstrated in the previous papers using BSCF disc and tubular membrane reactors [5-8].

Only CO₂ rather than the other carbon-containing products (CO and C₂-hydrocarbons) was observed when the BCFZ membrane is used for methane oxidation at 875 °C (Fig. 5.2). This finding is in agreement with the results presented in section 6.2. However, in contrast to the transient experiments, methane conversion was very low (< 3.0 %) in the membrane reactor. This is due to the low surface area of the hollow fibre membrane and due to the higher ratio of fed methane to the amount of catalyst as compared to the transient experiments in section 6.2. A large amount of un-reacted gaseous oxygen was found at the outlet of the membrane reactor besides the non-consumed methane. Therefore, it is reasonable to use a suitable catalyst, which will selectively catalyse methane oxidation with gas-phase oxygen. In the present study, the classical Ni-based steam reforming (SR) catalyst was packed on the membrane surface of the core side. Fig. 5.6 shows the catalytic performance of the BCFZ hollow fiber membrane reactor in the presence of the Ni-based catalyst at different temperatures. The degree of methane conversion is considerably higher than that in the absence of the catalyst (Fig. 5.2). Moreover, CO and H₂ became the main reaction products (Fig. 5.6). The CO selectivity is above 95 % and the H₂/CO ratio is around 2.0 as expected for the POM reaction. The temperature increase in methane conversion is ascribed to the temperature-accelerated oxygen permeation flux. The changes in catalytic performance of the membrane reactor in the presence of the Ni-based catalyst can be explained as follows. The perovskite membrane permeates oxygen from the air side to the hydrocarbon side. Since the membrane has very low intrinsic activity for methane oxidation (Fig. 5.2), methane conversion to syngas is concluded to occur over the Ni-based catalyst. The present results do not provide mechanistic insights into syngas formation. However, taking into account the recently reviewed data on syngas production over various catalytic materials [9], CO and H₂ are suggested to be formed via indirect methane oxidation, i.e. total methane oxidation to CO₂ and H₂O followed by steam and dry reforming of methane.

From the transient experiments described in section 6.2, it can be concluded that the formation of ethylene from ethane occurs via oxidative dehydrogenation of ethane by

lattice oxygen of the BCFZ perovskite. Carbon dioxide is preferentially formed via consecutive ethylene oxidation. Besides, Fig. 5.6 demonstrates that the ratio of $S(\text{C}_2\text{H}_4)/S(\text{CO}_2)$ increases strongly with an increase in the amount of removed lattice oxygen. This means, that the higher the ratio of ethane to oxygen available for C_2H_6 dehydrogenation, the higher C_2H_4 selectivity can be expected.

Consequently, for a high ethylene selectivity the ratio of the fed ethane to the permeated oxygen should not be too low. Fig. 6.5 compares catalytic performance of the BCFZ perovskite in the ODE at different temperatures. When reaction temperature increases from 700 °C to 800 °C, ethane conversion and ethylene selectivity increases from 21 % to 63 % and from 59 % to 64 %, respectively. This is unusual for the ODE reaction, since ethylene selectivity typically decreases with an increase in ethane conversion. Taking into account these facts, it can be concluded that ethylene selectivity depends stronger on temperature than on ethane conversion. This may be due to higher activation energy of ethylene formation as compared to that of its further oxidation to CO_2 . However, the ethylene selectivity decreases sharply from 60 % to 40 % but the ethane conversion increases from 60 % to 90 % with further increase in temperature from 800 °C to 850 °C (Fig. 6.5). This strong decrease may be explained as follows. Upon increasing the degree of ethane conversion from 60 % to 90 %, ethane concentration decreases 4 times. The unreacted ethane decreases from 1.6 mL/min to 0.4 mL/min. Since ethane and ethylene compete for lattice oxygen of the perovskite membrane, ethylene combustion starts to overcome over ethylene formation from ethane due to a strong decrease in the ethane concentration. In addition, the negative influence of oxygen partial pressure on ethylene selectivity cannot be excluded.

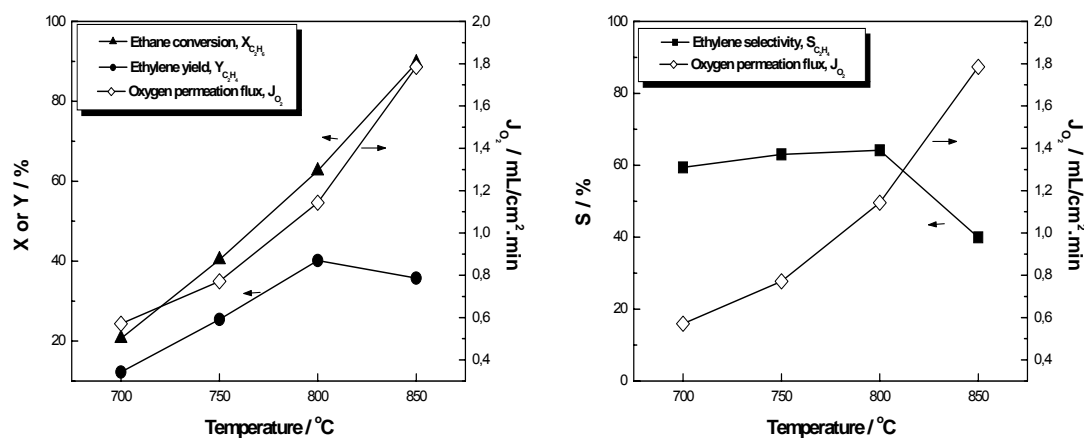


Figure 6.5 The effect of temperature on the ethane conversion and product selectivity of the ODE in the BCFZ hollow fiber membrane reactor. 40 mL/min a mixture of 10 % ethane and 90 % He on the sweep side, air flow rate on the shell side: 300 mL/min, membrane surface area: 3.52 cm².

As discussed in section 6.2, CO₂ formation in the ODE reaction is suggested to occur via consecutive oxidation of primarily formed C₂H₄. Therefore, in order to achieve high ethylene selectivities, short contact times of ethane with the perovskite surface are recommended. Fig. 6.6 shows the effect of the flow rate of a mixture of 90% He diluted ethane on the ethane conversion and product selectivities of the ODE in the BCFZ hollow fiber membrane reactor at 800 °C. As expected, ethylene selectivity increases from 64 % to 68 % with increasing the total flow rate of He and ethane from 40 mL/min to 80 mL/min, i.e. decreasing the contact time from 0.078 s to 0.039 s. This means that the contact time influences the ethylene selectivity; a shorter contact time gives higher ethylene selectivity. The concept of short contact times is in accordance with recent literatures on the oxidative dehydrogenation of ethane [9-11]. Ethylene yields up to 56 % at 71 % selectivity were achieved in autothermal oxidative dehydrogenations at short contact times of ca. 45 ms using catalysts as ignitors [10]. Schmidt and co-workers [11, 12] have also used the concept of very short contact times in the ms-range on noble metal coated monoliths at 920 °C to obtain ethylene yields of 53 - 57 % with selectivities ranging from 66 % to 70 %.

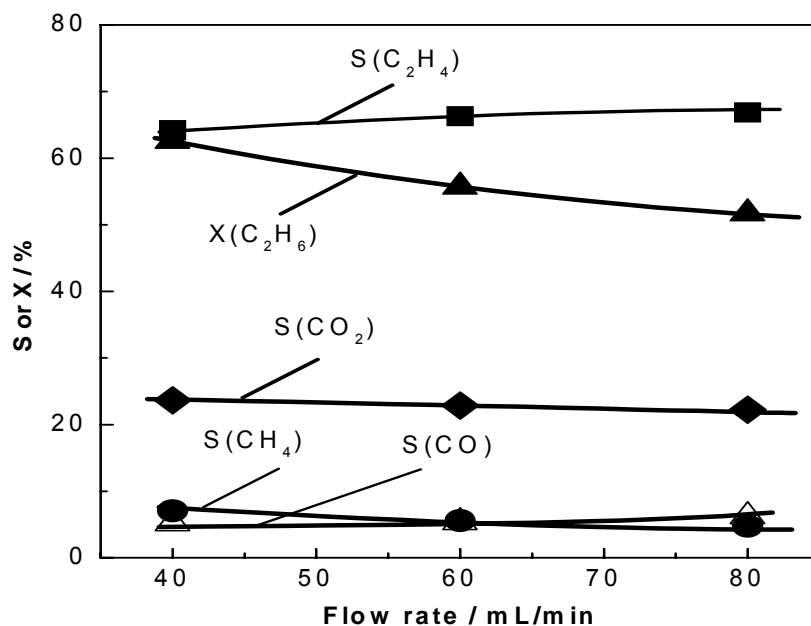


Figure 6.6 The effect of flow rate of a mixture of 90 % He diluted ethane on the ethane conversion and product selectivity of the ODE in the BCFZ perovskite hollow fiber membrane reactor at 800 °C. Membrane surface area: 3.52 cm², air flow rate on the shell side: 300 mL/min.

The idea of short contact times was also proven in the present study by performing the ODE reaction in reactors of different membrane geometries: i) the BCFZ disc (Fig. 6.7a) and ii) hollow fiber membrane reactors (Fig. 6.7b). As shown in Fig. 6.7, in the disc membrane reactor, the ethane reacted with lattice oxygen to form ethylene, and then the produced ethylene can leave the reactor in time. Therefore, the deep oxidation of ethylene can be largely avoided in the disc membrane reactor. However, for the hollow fiber membrane reactor, once ethylene was formed, it would react again with lattice oxygen or gaseous oxygen molecular to form CO_x. In the hollow fiber membrane reactor the contact time is 0.078 s, however, in the disk membrane reactor the contact time is 0.0023 s assuming 1 mm thickness above the membrane as the reaction zone. This means that the contact time in the disk membrane is much shorter than that in the hollow fiber reactor, which results in the higher ethylene selectivity in the disk membrane reactor.

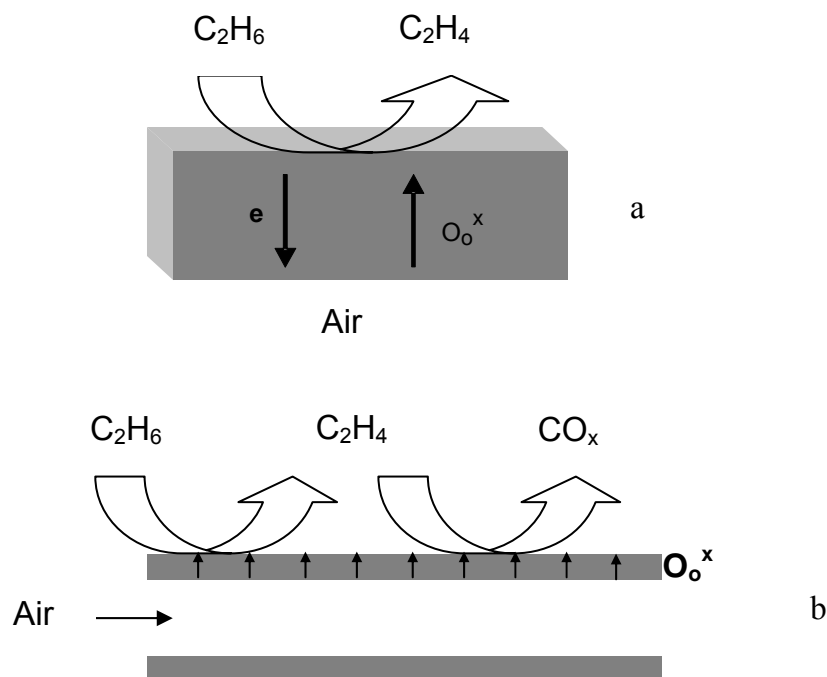


Figure 6.7 Comparison of the ODE in the disc membrane reactor (a) and in the hollow fiber membrane reactor (b).

For comparable degrees of ethane conversion (ca. 90 %), the ethylene selectivity in the disc membrane reactor was ca. 80 % as compared to 40 % only in the hollow fibre membrane (Table 6.1). More CO_2 was produced in the hollow fiber membrane reactor than in the disc membrane reactor. This means that the deeper oxidation of ethane/ethylene can not be avoided in the hollow fiber membrane reactor. High ethylene yield and selectivity obtained in the disc membrane reactor are comparable with those reported in literature. Wang et al. [5, 6] reported an ethylene selectivity of 80 % at an ethane conversion of 84 % at 800 °C using planar and tubular oxygen permeable mixed ion and electron-conducting membranes made of $Ba_{0.5}Sr_{0.5}Co_{0.8}Fe_{0.2}O_{3-\delta}$. On the same material an ethylene yield of 66 % was obtained at 807 °C and could be improved up to 76 % after Pd deposition [7, 8]. An ethylene yield of 56 % with an ethylene selectivity of 80 % was achieved in a dense tubular ceramic membrane reactor made of $Bi_{1.5}Y_{0.3}SmO_3$ at 875 °C [13].

Table 6.1 Catalytic performance of BCFZ disc membrane reactor and BCFZ hollow fiber membrane reactor at 850 °C

Reactor Types	C ₂ H ₆ Conversion, %	Product Selectivity, %			
		C ₂ H ₄	CH ₄	CO	CO ₂
Disc membrane reactor	85.2	79.1	10.7	5.4	4.8
Hollow fiber membrane reactor	89.6	39.9	12.1	15.4	32.6

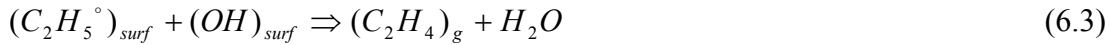
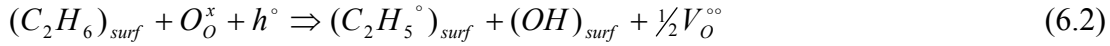
Membrane surface area of disc membrane and hollow fiber are 0.90 cm² and 3.52 cm². Feed: 40 mL/min 90 % He diluted ethane on the sweep side, air flow rate on the shell side: 300 mL/min.

6.4 Mechanistic aspects of hydrocarbon conversion over BCFZ perovskite

At temperatures above 650 °C, the thermal dehydrogenation of ethane (TDE) to ethylene, $C_2H_6 \rightleftharpoons C_2H_4 + H_2$, is thermodynamically favored. Since the operation temperature is up to 850 °C, the ethane conversion through the TDE was of concern. However, the ethane conversion is determined by the reaction kinetics and reactor conditions. Akin and Lin [13] had estimated the TDE at 850 °C with residence time of 0.07 – 0.1 s would result in less than 0.2 % ethane conversion based on the available kinetic data (reaction order and rate constant) and plug flow reactor model [14]. In the hollow fiber membrane reactor presented here, the residence time is changed from 0.04 s to 0.1 s, thus the TDE is not significant in the experiments. Actually from the experimental finding, it was found ≤ 1 vol. % hydrogen in the product gases. Therefore the TDE is not discussed in the following.

Taking into account the present (sections 6.2 and 6.3) and previous results [15], the following mechanistic concept of oxidation of light alkanes (CH₄ and C₂H₆) in the BCFZ membrane reactor can be suggested. The hydrocarbons are first in contact with the membrane surface where they react with lattice oxygen (O²⁻) to form the respective

radicals (Eq. 6.2). The later reaction can occur either on the catalyst surface (Eq. 6.3) or in the gas phase (Eq. 6.4).



where $V_O^{\circ\circ}$ are oxygen vacancies and h° is electron holes.

It is well accepted that the alkane activation (Eq. 6.2) is the rate limiting reaction step, which determines product formation. Since reactions (6.3) and (6.4) are a fast irreversible reaction, ethylene production rate is determined by reactions (6.1) and (6.2). If the reaction (6.2) can not consume all of the lattice oxygen (O_O^x) completely or the reaction rate of Reaction (6.2) is not fast enough to consume the lattice oxygen in time, the formation of gaseous oxygen can occur:



Therefore, the lattice oxygen (O_O^x) on the membrane surface exposed to the hydrocarbons is competitively consumed by two reactions: hydrocarbon activation (Eq. 6.2) and the recombination of oxygen ions (Eq. 6.5). Since the activation energy of the latter reaction is higher than that of the other reactions, the formation of gas-phase oxygen is accelerated by temperature. Therefore, non-selective hydrocarbon oxidation to CO_2 is expected to increase with temperature due to increased contribution of gas-phase reactions between O_2 and methyl or ethyl radicals. In this case selectivity to high value products drops as shown in Fig. 6.6 and previously reported by some of the authors [13]. Taking into account this discussion, it is easily to understand complete CH_4 oxidation to CO_2 in the BCFZ membrane reactor (Fig. 5.2). Due to the strong C-H bond in CH_4 molecule, CH_4 oxidation is performed at temperatures above 850 °C, where formation of gas-phase oxygen takes place and, therefore, non-selective oxidation is preferential. The contribution of gas-phase reactions to the CH_4 conversion is minimised under transient conditions of the TAP reactor due to high vacuum and low pulse size. As result, C_2H_6 formation from CH_4 was observed in transient experiments (Figs. 6.2a and 6.4). In the case of ethane because the

gaseous oxygen produced in reaction 5 could further react with ethylene or ethane to form CO_x , thus decreasing the ethylene selectivity. So the ethylene selectivity is determined by the competition between reactions 6.1 and 6.5. As shown in Fig. 6.6, the ethylene selectivity increased with raising the temperature when it is lower than 800 °C. However, when the temperature is higher than 800 °C, the ethylene selectivity decreased with increasing temperature. This result indicates that the recombination rate of lattice oxygen (reaction 6.5) increases faster than the ethane activation (reaction 6.1) at temperatures higher than 800 °C.

It is worthy to note that the oxygen permeation flux through the hollow fiber membrane during the ODE increases from 0.6 mL/cm².min to 1.8 mL/cm².min when the temperatures increase from 700 °C to 850 °C and no gaseous oxygen was found downstream corresponding to a total consumption of oxygen across the hollow fiber membrane. However, the oxygen permeation flux improved only slightly compared with that using pure helium as sweep gas. This finding is similar to the previous results of the ODE on disc and tubular membranes made of BSCF [5, 6] but different from the results of the partial oxidation of methane to syngas (POM). The oxygen permeation flux through the membrane during the POM is 5 – 10 times larger of that using pure helium as sweep gas [16, 17]. The reason is that the POM is so fast that the lattice oxygen (O_o^x) can be consumed by reaction with methane once methane reaches the surface of the membrane in the present of a POM catalyst. As a result, the oxygen partial pressure on the membrane surface decreased sharply to a very low value (10^{-17} bar) and leads to a large enhancement of the oxygen permeation flux. From the comparison of the oxygen permeation flux in the ODE and POM, it follows that the ODE reaction rate is not fast enough to consume the lattice oxygen (O_o^x) so that it could be recombined to gaseous oxygen and released to gas phase.

6.6 Conclusions

From mechanistic transient experiments in the TAP reactor, it is concluded that lattice oxygen of the BCFZ perovskite is responsible for the activation of methane and ethane

yielding C_2H_6 , CO_2 and C_2H_4 . C_2H_6 and C_2H_4 are the primary products of CH_4 and C_2H_6 oxidation, respectively. CO_2 is formed via consecutive oxidation of these primary products. Direct oxidation of alkanes (CH_4 and C_2H_6) cannot be completely excluded. This reaction pathway may dominate at low conversions of fed alkanes.

The degree of catalyst reduction in the CH_4 or C_2H_6 pulse experiments was found to influence the reaction selectivity. The lower the degree of catalyst reduction (oxidized sample), the higher is the formation of CO_2 . Consequently, for the selective oxidation of methane and ethane in the BCFZ perovskite membrane reactor the ratio of the permeated oxygen to the fed alkane should be fine-tuned. In contrast to ethane oxidation, methane oxidation in the BCFZ perovskite membrane reactor results in CO_2 formation only. This is ascribed to the fact that due to high stability of methane molecule, methane oxidation is carried out at high temperatures, where the ratio of methane to oxygen is too low for selective methane oxidation. Methane could be selectively converted to syngas (H_2 and CO) in the BCFZ perovskite membrane reactor in the presence of additional Ni-based catalyst.

Ethane oxidation in the BCFZ perovskite membrane reactor yields ethylene. The ODE catalytic activity of BCFZ was first tested both in the conventional co-feed packed bed reactor and the periodically operated shifted reactor, which shows that the BCFZ possesses good catalytic activity for ODE. The first results of the ODE using the BCFZ hollow fiber membrane are reported giving ethylene yields $\leq 40\%$ at $800\text{ }^\circ\text{C}$. To get higher ethylene yields on the hollow fiber geometry, the reaction conditions of the ODE have to be optimized. Comparing the ODE using the BCFZ disc and hollow fiber membrane reactors, the ethylene selectivity on the disc membrane reactor was found to be $\leq 80\%$ whereas using the hollow fiber membrane ethylene selectivity $\leq 68\%$ was found. The ethylene selectivity is influenced by the reactor geometry. Disc membrane reactor transforms the ethane more selectively as compared to the hollow fiber. This is due to a shorter residence time in the former reactor. Obviously, in the case of the hollow fiber membrane the deeper oxidation of ethylene to CO and CO_2 could not be avoided.

6.7 Bibliography

- [1] J. T. Gleaves, G. S. Yablonsky, P. Phanawadee, Y. Schuurman, *Appl. Catal. Gen. A* 160 (1997) 55.
- [2] E. Kondratenko, M. Cherian, M. Baerns, *Catal. Today* 99 (2005) 59.
- [3] H. Wang, V. Kontratenko, C. Tablet, E. Kondratenko, J. Caro, *Appl. Catal.*, accepted.
- [4] J. H. Lunsford, *Handbook of Heterogeneous Catalysis*, Eds. G. Ertl, H. Knözinger and J. Weitkamp, Wiley-VCH, Weinheim, 1997, 1843.
- [5] H. Wang, Y. Cong, W. Yang, *Chem. Comm* 14 (2002) 1468.
- [6] H. Wang, Y. Cong, W. Yang, *Catal. Lett.* 84 (2002) 101.
- [7] M. Rebeilleau, A.C. van Veen, D. Farrusseng, J. Rousset, C. Mirodatos, Z. Shao, G. Xiong, *Stud. Surf. Sci. Catal.* 147 (2004) 655.
- [8] M. Rebeilleau, S. Rosini, A. C. van Veen, D. Farrusseng, C. Mirodatos, *Catal. Today* 104 (2005) 131.
- [9] E. V. Kondratenko, M. Baerns, *Encyclopedia of Catalysis*, I. Horvyth (Ed.), John Wiley and Sons, 6 (2003) 424.
- [10] S. A. R. Mulla, O. V. Buyevskaya, M. Baerns, *J. Catal.* 43 (2001) 197.
- [11] M. Huff, L. D. Schmidt, *J. Phys. Chem.* 97 (1993) 11815.
- [12] C. Yokoyama, S. S. Bharadwaj, L. D. Schmidt, *Catal. Lett.* 38 (1996) 181.
- [13] F. T. Akin, Y. S. Lin, *J. Membr. Sci.* 209 (2002) 457.
- [14] A. M. Brodsky, R. A. Kalienko, K. P. Lavrosky, *J. Chem. Soc.* 11 (1960) 4443.
- [15] H. H. Wang, C. Tablet, T. Schiestel, J. Caro, *Catal. Today*, in press.
- [16] H. Wang, Y. Cong, W. Yang, *Catal. Today* 82 (2003) 157.
- [17] J. Tong, W. Yang, R. Cai, B. Zhu, L. Lin, *Catal. Lett.* 78 (2002) 129.

7 Conclusions and outlook

Dense ceramic membranes with high oxygen ionic and electronic conductivities are of increasing interest as economical, clean and efficient membrane material to produce oxygen or oxygen-enriched air by separating oxygen from air or other oxygen containing gases. Furthermore, these oxygen transporting materials are worldwide intensively tested in catalytic membrane reactors for partial oxidations. Different membrane geometries are used but it is shown in this Ph.D work that the hollow fiber geometry can provide the highest oxygen permeation flux so far reported as well as the largest membrane area per unit packing volume when assembled to a membrane permeator or membrane reactor. The successful development of perovskite hollow fibers is considered a remarkable step towards the industrial application of oxygen transporting membranes in air separation and catalytic membrane reactors for the partial oxidation of methane to syngas or for the oxidative dehydrogenation of light alkanes to the corresponding olefins. This PhD work shows that the hollow fiber membranes are possible candidates for an industrial applications.

First, the $\text{BaCo}_x\text{Fe}_y\text{Zr}_z\text{O}_{3-\delta}$ (BCFZ) hollow fibers prepared at the Fraunhofer Institute for Interfacial Engineering and Biotechnology (IGB), Stuttgart were used to construct a membrane permeator for oxygen separation. The green and the sintered hollow fiber perovskite membranes showed an asymmetric structure due to shearing forces in the spinning process. Because of the structured walls, not the whole wall thickness represents the permeation length and very high oxygen permeabilities through the hollow fiber membranes compared to a disc membrane of the same thickness were obtained. A significant shrinkage of the sintered hollow fiber due to the removal of the polymeric binders and the sintering of the BCFZ particles was observed. A very high oxygen flux was obtained under the air/He gradient which is the highest oxygen permeation flux reported in the open literatures so far. The oxygen permeation flux through the hollow fiber membrane is stable under the air/He gradient.

The novel O₂-permeable membrane material with high O₂ permeation fluxes and excellent thermal and mechanical stability was successfully applied in a hollow fiber configuration to prove the possibility of the production of O₂-enriched air in a perovskite membrane permeator. O₂-enriched air with 30 – 60 vol. % oxygen can be used in several industrial processes, for example in the ammonia synthesis, the Claus process and the Fluid Catalytic Cracking catalyst regeneration, the efficient utilization of methane in high-temperature furnaces or cement kilns. Different degrees of O₂-enrichment in air and different production rates could be achieved by controlling the operational parameters such as temperature, oxygen partial pressure difference and gas flow rates. As an example, for more than 820 h oxygen-enriched air with 41.5 vol. % O₂ could be produced.

The high oxygen flux renders the BCFZ material in hollow fiber geometry for mixed ionic and electronic conducting membranes in corresponding membrane reactors for the industrial oxidative activation of light hydrocarbons, especially the partial oxidation of methane to syngas (POM), and the oxidative dehydrogenation of ethane to ethylene (ODE) in a perovskite MIEC membrane reactor. The BCFZ hollow fiber perovskite membrane used for the POM showed that in the membrane reactor without catalyst filling the product gas contained mainly unreacted CH₄ and O₂ and a few percent of CO₂. Therefore, a commercial Ni-based steam reforming (SR) catalyst was used. To obtain ideal conditions for the POM reaction in the membrane reactor, different catalyst locations were tried. When the SR catalyst is packed around and behind the hollow fiber membrane, a very high CO selectivity was observed. It is supposed that CO and H₂ were formed by reforming reactions of methane with CO₂ and H₂O. The oxygen permeation flux of the hollow fiber membrane in the POM reaction was very high compared to helium as sweep gas since methane can reduce the oxygen concentration deeper than a sweep gas can do it. A problem is that the BCFZ material is not stable in a CO₂ containing atmosphere and as a result the material decomposes due to BaCO₃ formation after a few hours of the POM reaction. Another failure mechanism is the destruction of the perovskite by Al from the catalyst which enters the perovskite via a solid state diffusion. Avoiding catalyst contacting the fiber and finding a suitable catalyst location could improve the POM performance and stability. It was found that the catalyst location should be behind the

fiber. The Ni-based SR catalyst exhibits good activity towards the transformation of methane to synthesis gas.

The results of the ODE in the BCFZ perovskite hollow fiber membrane reactor were compared with those of a BCFZ disc membrane. The ethylene selectivity on the disc membrane reactor was found to be higher than that on the hollow fiber membrane. The ethylene selectivity is influenced by the reactor geometry. The disc membrane reactor transforms the ethane more selectively due to a shorter residence time as compared to the hollow fiber. In the case of the hollow fiber membrane the deeper oxidation of ethylene to CO and CO₂ could not be avoided due to repeated contacts with the inner wall of the hollow fiber. The hollow fiber membrane can not be successfully used for high ODE performances.

This Ph.D work shows that the hollow fiber perovskite membranes can not only be used for simple oxygen separation, oxygen-enriched air production, but also for delivering oxygen for partial oxidation of methane to syngas. In the future the stability of the hollow fiber membrane should be studied under POM conditions. For fundamental studies under lab-scale conditions, at first the fiber coated by an Au-paste can be surrounded by an alumina tube to avoid the contact between the Au layer and the Ni-based steam reforming catalyst.

However, before an industrial application, several problems have to be solved. One of the major problems is the construction of an industrial modul with some m² of membrane surface. The materials challenge is the gas-tight and long-term stable junction of the ceramic perovskite hollow fibers with a stainless steel housing.

List of publications and conferences

Publications

a) Appeared

1. H. Wang, **C. Tablet**, A. Feldhoff, J. Caro, *A cobalt-free oxygen-permeable membrane based on the perovskite-type oxide $Ba_{0.5}Sr_{0.5}Zn_{0.2}Fe_{0.8}O_{3-\delta}$* , Adv. Mat., 17 (2005) 1785.
2. **C. Tablet**, G. Grubert, H. Wang, T. Schiestel, M. Schroeder, B. Langanke, J. Caro, *Oxygen permeation study of perovskite hollow fiber membranes*, Catal. Today, 104 (2005) 126.
3. H. Wang, **C. Tablet**, A. Feldhoff, J. Caro, *Investigation of phase structure, sintering, and permeability of perovskite-type $Ba_{0.5}Sr_{0.5}Co_{0.8}Fe_{0.2}O_{3-\delta}$ membranes*, J. Membr. Sci., 262 (2005) 20.
4. H. Wang, **C. Tablet**, W. Yang, J. Caro, *In situ high temperature X-ray diffraction studies of mixed ionic and electronic conducting perovskite-type membranes*, Mat. Lett. 59 (2005) 3750.
5. H. Wang, W. Yang, **C. Tablet**, J. Caro, *Oxygen diffusion in oxide crystals - Tracing new routes to identify the rate limiting step of oxygen permeation through perovskite membranes*, Diff. Fund. 1 (2005) 246.
6. **C. Constantin**, V. Pârvulescu, A. Bujor, G. Popescu, B. L. Su, *Mesoporous nickelsilicate membranes on porous alumina supports. I. Effect of nature and surface pretreatment of alumina supports on the catalytic membrane formation*, J. Mol. Catal. A: Chem., 208 (2004) 245.
7. V. Pârvulescu, **C. Constantin**, G. Popescu, B. L. Su, *Mesoporous nickelsilicate membranes on porous alumina supports. II. Catalytic reactor for oxidation of aromatic hydrocarbons*, J. Mol. Catal. A: Chem., 208 (2004) 253.

8. V. Pârvulescu, **C. Tablet**, C. Anastasescu, B. L. Su, *Activity and stability of bimetallic Co (V, Nb, La)-modified MCM-41 catalysts*, Catal. Today, 93-95 (2004) 307.
9. V. Parvulescu, C. Anastasescu, **C. Constantin**, B. L. Su, *Mono (V, Nb) or bimetallic (V-Ti, Nb-Ti) ions modified MCM-41 catalysts: synthesis, characterization and catalysis in oxidation of hydrocarbons (aromatics and alcohols)*, Catal. Today, 78 (2003) 477.
10. V. Parvulescu, **C. Constantin**, B. L. Su, *Liquid phase oxidation of aromatic hydrocarbons using highly ordered Nb and NbCo-MCM-41 nanoreactors*, J. Mol. Catal. A: Chem., 202 (2003) 171.
11. **C. Constantin**, V. Parvulescu, A. Bujor, G. Popescu, B. L. Su, *The effects of nature and pretreatment of surface alumina support on the catalytic nickelsilicate membrane formation*, E. Gaigneaux et al. (Eds.), Stud. Surf. Sci. Catal., 143 (2002) 67.
12. V. Parvulescu, C. Anastasescu, **C. Constantin**, B. L. Su, *Highly selective oxidation of aromatic hydrocarbons (styrene, benzene and toluene) with H₂O₂ over Ni, Ni-Cr and Ni-Ru modified MCM-41 catalysts*, R. Aiello, G. Giordano and F. Testa (Eds.), Stud. Surf. Sci. Catal., 142 (2002) 1213.

b) Accepted, in print, submitted

1. H. Wang, P. Kölsch, T. Schiestel, **C. Tablet**, S. Werth, J. Caro, *Production of high-purity oxygen by perovskite hollow fiber membrane swept with steam*, Chem. Commun., submitted.
2. C. Hamel, A. S. Morgenstern, T. Schiestel, S. Werth, **C. Tablet**, J. Caro, H. Wang, *Experimental and modeling study on dense perovskite hollow fiber membranes for the production of O₂-enriched air*, AIChE Journal, in revised version.
3. H. Wang, **C. Tablet**, T. Schiestel, S. Werth, J. Caro, *Partial oxidation of methane to syngas in a perovskite hollow fiber membrane reactor*, Catal. Commun., in press.

4. H. Wang, V. Kondratenko, **C. Tablet**, E. Kondratenko, J. Caro, *Selective oxidations of CH₄ and C₂H₆ over a mixed oxygen ion and electron conducting perovskite – a TAP and membrane reactors study*, React. Kin. Catal. Lett., submitted.
5. H. Wang, T. Schiestel, **C. Tablet**, S. Werth, J. Caro, Mixed oxygen ion and electron conducting hollow fiber membranes for oxygen separation, Solid State Ionics, in revised version.
6. H. Wang, **C. Tablet**, T. Schiestel, J. Caro, *Hollow fiber membrane reactors for the oxidative activation of ethane*, Catal. Today, accepted.
7. J. Caro, H. Wang, **C. Tablet**, A. Kleinert, A. Feldhoff, T. Schiestel, M. Kilgus, P. Kölsch, S. Peter, *Evaluation of perovskites in hollow fibre and disk geometry in catalytic membrane reactors and in oxygen separators*, Catal. Today, accepted.

Patents

1. H. Wang, G. Grubert, **C. Tablet**, J. Caro, *Oxygen transporting oxide ceramics*, **European Patent**, N1010-N-EP, 2005, EP1630148/05102708.4.

Conferences

1. H. Wang, T. Schiestel, **C. Tablet**, J. Caro, *Hollow fiber membrane reactors for oxidative activation of light hydrocarbons*, The 7th International Conference on Catalysis in Membrane Reactors, Calabria, Italy, Sept. 2005 (Talk).
2. J. Caro, A. Kleinert, H. Wang, **C. Tablet**, T. Schiestel, M. Kilgus, S. Peter, *Evaluation of hollow fiber perovskite membranes in catalytic membrane reactors for selective partial oxidation and in separators for oxygen production*, The 7th International Conference on Catalysis in Membrane Reactors, Calabria, Italy, Sept. 2005 (Talk).
3. M. Kilgus, H. Wang, **C. Tablet**, J. Caro, T. Schiestel, *Perovskite hollow fibre membranes for oxygen separation*, The 7th International Conference on Catalysis in

- Membrane Reactors, Calabria, Italy, Sept. 2005 (Poster).
4. H. Wang, T. Schiestel, **C. Tablet**, S. Peter, J. Caro, *Mixed oxygen ion and electron conducting hollow fiber membranes for oxygen separation*, The 15th International Conference on Solid State Ionics, Baden-Baden, Germany, July 2005 (Talk).
 5. M. Schroeder, **C. Tablet**, G. Grubert, H. Wang, T. Schiestel, H. Hederer, J. Caro, *Oxygen permeation study of perovskite hollow fibre membranes for the partial oxidation of methane*, Engineering Conferences International 6 MetroTech Center, Brooklyn, NY 11201, USA, Nonstoichiometric Compounds, Kauai, Hawaii, Apr. 2005 (Poster).
 6. **C. Tablet**, H. Wang, A. Feldhoff, T. Schiestel, J. Caro, *Catalyst coated dense hollow fibre membranes for partial oxidation of methane to syngas*, The 38th German Annual Conference on Catalysis, Weimar, Germany, Mar. 2005 (Poster).
 7. H. Wang, T. Schiestel, **C. Tablet**, J. Caro, *Catalytic membrane reactors for oxidative dehydrogenation of ethane (ODE) to ethylene*, The 38th German Annual Conference on Catalysis, Weimar, Germany, Mar. 2005 (Poster).
 8. V Parvulescu, G Telipan, **C. Tablet**, M Ignat, N Cioatera, B.G. Albu, *Synthesis of mesoporous Y_2O_3 - TiO_2 - ZrO_2 oxides by sol-gel method*, Scientific Advances in Fuel Cell Systems, München, Germany, Oct. 2004 (Poster).
 9. M. Kilgus, **C. Tablet**, N. Dinges, D. Senftleben, T. Schiestel, *Inorganic hollow fibres membranes for gas separation*, Euromembrane 2004, Hamburg, Germany, Sept. – Oct. 2004 (Poster).
 10. V. Parvulescu, **C. Tablet**, B. L. Su, *Oriented zeolite membranes obtained from mesostructured films supported on alumina*, The 6th International Conference on Catalysis in Membrane Reactors, Lahnstein, Germany, July 2004 (Poster).
 11. H. Wang, **C. Tablet**, G. Grubert, A. Feldhoff, J. Caro, *Investigation of sintering, phase structure and oxygen permeability of perovskite-type $Ba_{0.5}Sr_{0.5}Co_{0.8}Fe_{0.2}O_{3-\delta}$* , The 6th International Conference on Catalysis in Membrane Reactors, Lahnstein, Germany, July 2004 (Poster).
 12. **C. Tablet**, G. Grubert, H. Wang, J. Caro, T. Schiestel, M. Schroeder, H. Hederer, *Oxygen permeation study of perovskite hollow fibre membranes for the partial*

- oxidation of methane to syngas*, The 6th International Conference on Catalysis in Membrane Reactors, Lahnstein, Germany, July 2004 (Poster).
13. A. Popa, Gh. Ilia, S. Iliescu, **C. Tablet**, E. Sacaliuc, V. Parvulescu, *Phosphonates obtained by Michaelis-Arbuzov reaction incorporated into hierarchically ordered silica*, The 11th International Conference on Polymers and Organic Chemistry, Prague, Czech Republic, July 2004 (Poster).
 14. V. Parvulescu, **C. Tablet**, C. Anastasescu, B. L. Su, *Reactivity and stability of bimetallic Co (V, Nb, La) – modified MCM-41 mesoporous catalyst*, The 3rd Asia Pacific Congress on Catalysis, Dalian, China, Oct. 2003 (Talk).
 15. V. Parvulescu, **C. Tablet**, G. Roman, B. G. Albu, G. Popescu, B. L. Su, *Composite membranes with bimetallic V(Ti, Co)-MCM-41 molecular sieves for catalytic treatment of waste water*, The European Catalysis Forum (Europa Cat – VI), Innsbruck, Austria, Aug. – Sept. 2003 (Poster).
 16. V. Parvulescu, **C. Tablet**, A. Bujor, G. Popescu, B. L. Su, *Gas permeation and catalytic oxidation of hydrocarbons by nickelsilicate mesoporous membranes supported on alumina*, The 11th Physical Chemistry Conference, Timisoara, Romania, Sept. 2003 (Poster).
 17. **C. Constantin**, V. Pârvulescu, A. Bujor, G. Popescu, B. L. Su, *The effects of nature and pretreatment of surface alumina support on the catalytic nickelsilicate membrane formation*, Proc. VIII International Symposium on Preparation of Catalysts, Louvain-la-Neuve, Belgium, Sept. 2002 (Talk).
 18. V. Parvulescu, C. Anastasescu, **C. Constantin** and B. L. Su, *Highly selective oxidation of aromatic hydrocarbons (styrene, benzene and toluene) with H₂O₂ over Ni, Ni-Cr and Ni-Ru modified MCM-41 catalysts*, The 2nd Federation of the European Zeolite Association, “Impact of zeolites and other porous materials on the new technologies at the beginning of the new millennium”, Italy, Sept. 2002 (Talk).
 19. **C. Constantin**, V. Pârvulescu, A. Dobre, A. Bujor, G. Popescu, B. L. Su, *Nickelsilicate mesoporous membranes synthesized on porous alumina supports*,

- The 7th International Conference of Inorganic Membranes, Dalian, China, July 2002 (Talk).
20. V. Pârvulescu, **C. Constantin**, G. Popescu, B. L. Su, *Oxidation of the aromatic hydrocarbons in the nickelsilicate membrane reactor*, The 7th International Conference of Inorganic Membranes, Dalian, China, July 2002 (Poster).
 21. V. Parvulescu, **C. Constantin**, B. L. Su, *Vanadium and niobium-MCM-41 mesoporous molecular sieves modified with titanium as catalysts in oxidation of aromatic hydrocarbons*, The 4th International Symposium on Group V, Toledo, Spain, Apr. 2002 (Talk).
 22. V. Parvulescu, **C. Constantin**, B. L. Su, *Highly ordered Nb, NbCo-MCM-41 molecular sieves and their application in oxidation of aromatic hydrocarbons*, The 4th International Symposium on Group V, Toledo, Spain, Apr. 2002 (Poster).
 23. B.G. Albu, G. Roman, **C. Tablet**, Gh. Batrănescu, G. Popescu, V. Pârvulescu, *Composite membranes with mesoporous silica and their utilization in wastewater purification*, JINR-Romanian Workshop, “Advanced materials and their characterization”, Dubna, Russia, Mar. 2002 (Talk).
 24. V. Parvulescu, **C. Tablet**, B. G. Albu, G. Popescu, B. L. Su, *Catalytic membranes synthesized on alumina support*, The 3rd Conference of Industrial Chemistry – University of Gh. Asachi, Iasi, Romania, Nov. 2002 (Poster).
 25. V. Parvulescu, C. Anastasescu, **C. Tablet**, E. Sacaliuc, B. L. Su, *Redox molecular sieves for oxidation reactions in liquid phase*, The 27th National Conference of Chemistry, Valcea, Romania, Oct. 2002 (Talk).
 26. **C. Tablet**, V. Parvulescu, B. G. Albu, G. Popescu, B. L. Su, *Nickelsilicate mesoporous membranes for oxidation of aromatic hydrocarbons*, NSF Workshop on Nanoscience and Technology – Romanian-American Workshop, Brasov, Romania, Oct. 2002 (Poster).
 27. B. G. Albu, **C. Tablet**, G. Roman, G. Popescu, V. Pârvulescu, *Ceramic/polysulfone composite membranes for wasted water purification*, The VIIth Symposium of Colloid and Surface Chemistry, Bucharest, Romania, Sept. 2002 (Talk).

28. V. Pârvulescu, **C. Tablet**, B. G. Albu, G. Popescu, B. L. Su, *Preparation, permeance and catalysis over nickelsilicate membranes*, The VIIth Symposium of Colloid and Surface Chemistry, Bucharest, Romania, Sept. 2002 (Talk).
29. **C. Constantin**, V. Pârvulescu, M. Alifanti, V. I. Pârvulescu, P. Grange, G. Poncelet, *Sol-gel prepared yttria-silica catalysts: characterization and catalytic performances in iso- and hydroisomerization of hexane, octane and decane*, Proceedings of International Symposium on Acid-Base Catalysis IV, T. Yamaguchi (Ed.) Matsuyama, Japan, 7-12 May, 2001 (Poster).

Curriculum vitae

Personal

Name	Cristina Tablet (born Constantin)
Date and Place of Birth	14 th June, 1976, Fetesti, Romania
Nationality	Romanian

Education:

1982 – 1994	Primary, Secondary and High School in Slobozia, Romania
1994 – 1999	Student of Chemistry at the University of Bucharest, Romania
06/1999	Diploma in Chemistry
1999 – 2001	Master of Science at the University of Bucharest, Romania
2001 – 2003	Chemist at the Research Center for Macromolecular Materials and Membranes, Bucharest, Romania
09/2003 – till date	Ph.D Student at the Institute of Physical Chemistry and Electrochemistry, University of Hanover, Germany